

AFRL-VA-WP-TR-1998-3058

**CHARACTERIZATION OF THE
FLOWFIELD NEAR A WRAP-AROUND
FIN AT SUPERSONIC SPEEDS**



Carl P. Tilmann

**Aerodynamic Components Research Branch
Air Vehicles Directorate
Air Force Research Laboratory
Wright-Patterson Air Force Base, Ohio 45433-7542**

FEBRUARY 1998

FINAL REPORT FOR PERIOD 1 OCTOBER 1995 – 1 MARCH 1997

Approved for public release; distribution unlimited

19990210 006

**AIR VEHICLES DIRECTORATE
AIR FORCE RESEARCH LABORATORY
AIR FORCE MATERIEL COMMAND
WRIGHT-PATTERSON AIR FORCE BASE, OH 45433-7542**

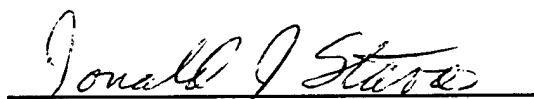
NOTICE

WHEN GOVERNMENT DRAWINGS, SPECIFICATIONS, OR OTHER DATA ARE USED FOR ANY PURPOSE OTHER THAN IN CONNECTION WITH A DEFINITELY GOVERNMENT-RELATED PROCUREMENT, THE UNITED STATES GOVERNMENT INCURS NO RESPONSIBILITY OR ANY OBLIGATION WHATSOEVER, THE FACT THAT THE GOVERNMENT MAY HAVE FORMULATED OR IN ANY WAY SUPPLIED THE SAID DRAWINGS, SPECIFICATIONS, OR OTHER DATA, IS NOT TO BE REGARDED BY IMPLICATION, OR OTHERWISE IN ANY MANNER CONSTRUED, AS LICENSING THE HOLDER, OR ANY OTHER PERSON OR CORPORATION; OR AS CONVEYING ANY RIGHTS OR PERMISSION TO MANUFACTURE, USE, SELL ANY PATENTED INVENTION THAT MAY IN ANY WAY BE RELATED THERETO.

THIS TECHNICAL REPORT HAS BEEN REVIEWED AND IS APPROVED FOR PUBLICATION.



CARL P. TILMANN
Aerospace Engineer
Aerodynamic Components
Research Branch



DONALD STAVA
Chief
Aerodynamic Components
Research Branch



DENNIS SEDLOCK
Chief
Aeromechanics Division

IF YOUR ADDRESS HAS CHANGED, IF YOU WISH TO BE REMOVED FROM OUR MAILING LIST, OR IF THE ADDRESSEE IS NO LONGER EMPLOYED BY YOUR ORGANIZATION PLEASE NOTIFY AFRL/VAAA, WRIGHT-PATTERSON AFB, OH 45433-7913 TO HELP MAINTAIN A CURRENT MAILING LIST.

COPIES OF THIS REPORT SHOULD NOT BE RETURNED UNLESS RETURN IS REQUIRED BY SECURITY CONSIDERATIONS, CONTRACTUAL OBLIGATIONS, OR NOTICE ON A SPECIFIC DOCUMENT.

REPORT DOCUMENTATION PAGE

Form Approved
OMB No. 0704-0188

Public reporting burden for this collection of information is estimated to average 1 hour per response, including the time for reviewing instructions, searching existing data sources, gathering and maintaining the data needed, and completing and reviewing the collection of information. Send comments regarding this burden estimate or any other aspect of this collection of information, including suggestions for reducing this burden, to Washington Headquarters Services, Directorate for Information Operations and Reports, 1215 Jefferson Davis Highway, Suite 1204, Arlington, VA 22202-4302, and to the Office of Management and Budget, Paperwork Reduction Project (0704-0188), Washington, DC 20503.

1. AGENCY USE ONLY (Leave blank)		2. REPORT DATE Feb 1998		3. REPORT TYPE AND DATES COVERED FINAL REPORT 1 OCTOBER 1995 - 1 MARCH 1997	
4. TITLE AND SUBTITLE CHARACTERIZATION OF THE FLOWFIELD NEAR A WRAP-AROUND FIN AT SUPERSONIC SPEEDS				5. FUNDING NUMBERS C: N/A PE: 62201F PR: 2404 TA: 10 WU: NM	
6. AUTHOR(S) Carl P. Tilmann					
7. PERFORMING ORGANIZATION NAME(S) AND ADDRESS(ES) Aerodynamic Components Research Branch Air Vehicles Directorate Air Force Research Laboratory Wright-Patterson Air Force Base, Ohio 45433-7542				8. PERFORMING ORGANIZATION REPORT NUMBER	
9. SPONSORING / MONITORING AGENCY NAME(S) AND ADDRESS(ES) Air Vehicles Directorate Air Force Research Laboratory Air Force Materiel Command Wright-Patterson Air Force Base, Oh 45433-7542 POC: Carl P. Tilmann, AFRL/VAAA, 937-255-4077				10. SPONSORING / MONITORING AGENCY REPORT NUMBER AFRL-VA-WP-TR-1998-3058	
11. SUPPLEMENTARY NOTES					
12a. DISTRIBUTION / AVAILABILITY STATEMENT APPROVED FOR PUBLIC RELEASE; DISTRIBUTION UNLIMITED				12b. DISTRIBUTION CODE	
13. ABSTRACT (Maximum 200 words) A wall-mounted semi-cylindrical model fitted with a single wrap-around fin (WAF) has been investigated numerically and experimentally, with the objective of characterizing the mean and turbulent flowfield near a WAF in a supersonic flowfield. Numerical and experimental results are used to determine the nature of the flowfield and quantify the effects of fin curvature on the character of the flow near WAFs. This research has been motivated by the need to identify possible sources of a high-speed rolling moment reversal observed in sub-scale flight tests. Detailed mean flow and turbulence measurements were obtained in the AFIT Mach 3 wind tunnel using conventional probes and cross-wire hot-film anemometry at a series of stations upstream of and aft of the fin shock/boundary layer interaction. Hot-film anemometry results showed the turbulence intensity and Reynolds shear stress in the fuselage boundary layer to be far greater on the concave side of the fin than on the convex side. Mean flow was also obtained in the AFIT Mach 5 wind tunnel using conventional pressure probes. Numerical results were also obtained at the test conditions employing the algebraic eddy viscosity model of Baldwin and Lomax. Correlation with experimental data suggests that the calculations have captured the flow physics involved in this complicated flowfield. The calculations, corroborated by experimental results, indicate that a vortex exists in the fin/body juncture region on the convex side of the fin. This feature is not captured by the oft-used inviscid methods, and can greatly influence the pressure loading on the fin near the root.					
14. SUBJECT TERMS Wrap-Around Fins, Missile Aerodynamics, Hot-Film Anemometry, Computational Fluid Dynamics, Shock/Boundary Layer Interactions				15. NUMBER OF PAGES 151	
				16. PRICE CODE	
17. SECURITY CLASSIFICATION OF REPORT UNCLASSIFIED	18. SECURITY CLASSIFICATION OF THIS PAGE UNCLASSIFIED	19. SECURITY CLASSIFICATION OF ABSTRACT UNCLASSIFIED	20. LIMITATION OF ABSTRACT SAR		

Table of Contents

	Page
List of Figures	vii
List of Tables	xi
List of Symbols	xii
1. Introduction	1-1
1.1 Wrap-Around Fins	1-1
1.2 Objectives of Present Research	1-3
1.3 Overview of Present Research	1-4
1.4 Outline of Document	1-5
2. Background	2-1
2.1 Blunt Unswept Fins	2-1
2.1.1 Experimental Investigations	2-2
2.1.2 Numerical Investigations	2-4
2.2 Experimental Turbulence Measurements	2-5
3. Experimental Methodology	3-1
3.1 WAF Model	3-1
3.2 Mach 3 Wind Tunnel	3-1
3.2.1 Operating Conditions	3-2
3.2.2 Tunnel Instrumentation	3-3
3.2.3 Traversing Equipment	3-3
3.3 Mach 5 Wind Tunnel	3-5
3.4 Pressure Probes	3-5
3.5 Hot-Film Cross-Wire Probes	3-7

	Page
3.6 Data Acquisition	3-10
3.7 Shadowgraph and Schlieren Optics	3-10
4. Numerical Methodology	4-1
4.1 Inviscid Calculations (M=2.9,5.0)	4-1
4.1.1 Grid Definition	4-1
4.1.2 Solution Strategy	4-2
4.1.3 Convergence Issues	4-4
4.1.4 Computational Requirements	4-4
4.1.5 Inviscid Fin Simulations at Other Mach Numbers . .	4-4
4.2 Viscous Calculations	4-4
4.2.1 Grid Definition	4-4
4.2.2 Solution Strategy	4-6
4.2.3 Convergence Issues	4-8
4.2.4 Mach 4.9 Calculations	4-11
4.2.5 Computational Requirements	4-12
5. WAF Flowfield at Mach 2.8	5-1
5.1 Pilot Inviscid Calculations	5-1
5.2 Shadowgraph and Schlieren Photography	5-1
5.3 Lambda Shock	5-3
5.4 Effect of Fin Curvature on the Flowfield	5-6
5.4.1 Flow Ahead of the Bow Shock	5-7
5.4.2 Flow on the Convex Side of the Fin	5-10
5.4.3 Flow on the Concave Side of the Fin	5-13
5.5 Aerodynamic Loading on the Fin	5-16
5.6 Effect of the Fin on Fuselage Boundary Layer Turbulence . .	5-18

	Page
6. WAF Flowfield at Mach 4.9	6-1
6.1 Shadowgraph and Schlieren Photography	6-2
6.2 Effect of Fin Curvature on the Mean Flowfield	6-4
6.2.1 Flow on the Convex Side of the Fin	6-5
6.2.2 Flow on the Concave Side of the Fin	6-7
6.3 Aerodynamic Loading on the Fin	6-8
7. Conclusions and Recommendations	7-1
7.1 Conclusions	7-1
7.2 Recommendations	7-3
7.2.1 General	7-3
7.2.2 Experimental	7-3
7.2.3 Numerical	7-4
8. Bibliography	8-1
Appendix A. Turbulent Navier-Stokes Equations	A-1
A.1 Overview	A-1
A.2 Navier-Stokes Equations	A-3
A.3 Reynolds (Time) Averaged Navier-Stokes Equations	A-3
A.4 Favré Averaged Navier-Stokes Equations	A-5
A.5 Zero-Equation Turbulence Models (Baldwin-Lomax)	A-7
Appendix B. Hot-Film Methods for Turbulence	B-1
B.1 Turbulence Fluctuations	B-3
B.2 Turbulence Transformation – Reynolds Shear Stress	B-6
Appendix C. Experimental Uncertainty Analysis	C-1
C.1 Measurement Errors	C-1
C.1.1 Conventional Probes	C-1

	Page
C.1.2 Hot-Film Probes	C-2
C.2 Error Propagation	C-3
C.2.1 Properties Determined with Pressure Probes	C-3
C.2.2 Properties Determined with Hot-film Measurements	C-5
C.2.3 Separation of Primitive Fluctuations	C-6
C.3 Comparison of $u-v$ and $u-w$ Hot-film Probes	C-6
C.4 Assessment of Probe Location Error Using Numerical Solutions	C-8
Appendix D. Mach 5 Wind Tunnel	D-1
D.1 Overview	D-1
D.2 Air Supply	D-1
D.3 Nozzle & Test Section	D-5
D.4 Diffuser & Silencer	D-7
D.5 Plenum Chamber Instrumentation	D-7
D.6 TSI 3-DOF Traverse System	D-8
D.7 Tunnel Calibration	D-10
D.8 Numerical Validation	D-10
Appendix E. GASP Input Deck for $M=2.8$ Viscous Simulation	E-1

List of Figures

Figure	Page
1.1. Typical WAF missile configuration (Vitale & Abate 1992).	1-2
2.1. Sketch of flow interference near a blunt fin (Hung and Kordulla, 1984).	2-2
2.2. The shock structure on symmetry plane ahead of a blunt fin.	2-3
3.1. Single wrap-around fin model (dimensions in inches).	3-2
3.2. Mach 3 wind tunnel schematic.	3-3
3.3. AFIT Mach 3 wind tunnel.	3-3
3.4. Traverse assembly (Miller).	3-4
3.5. AFIT Mach 5 wind tunnel with WAF model.	3-5
3.6. Pressure probes.	3-6
3.7. Hot film probes.	3-8
3.8. Shadowgraph camera and mirror setup.	3-11
3.9. Schlieren camera and mirror setup.	3-11
4.1. Grid boundaries and zonal structure for inviscid Mach 2.9 simulation. .	4-2
4.2. Grid boundaries and zonal structure for viscous simulations.	4-5
4.3. Effect of grid refinement on predicted boundary layer profile at the exit of the space-marched region ($z=0, x=-.5c$).	4-9
4.4. Effect of grid refinement on pitot pressure at downstream location. . .	4-10
4.5. Effect of grid resolution on the computed vortical structure ahead of the fin leading edge: $M=2.8$ laminar RANS simulation.	4-11
4.6. Residual history for $M=2.8$ laminar calculations in global region. . . .	4-12
4.7. Residual history for turbulent $M=4.9$ calculations in global region. . .	4-12
4.8. Effect of grid resolution on the computed vortical structure ahead of the fin leading edge: $M=4.9$ RANS simulation with Baldwin-Lomax. . . .	4-13
5.1. Computed inviscid test section surface pressures (at $M=2.9$).	5-2

Figure	Page
5.2. Shadowgraph of fin region.	5-3
5.3. Composite schlieren photograph – knife edge on top.	5-4
5.4. Composite schlieren photograph – knife edge on bottom.	5-4
5.5. Schlieren photograph showing lambda-shock structure.	5-5
5.6. Shadowgraph of the lambda-shock region.	5-5
5.7. Probe locations.	5-7
5.8. Numerical and experimental flow variables; convex side of fin.	5-8
5.9. Numerical and experimental flow variables; concave side of fin.	5-9
5.10. Convex measurement plane ($z=+0.47c$) pressure contours and mass-flux streamlines ($\rho u, \rho v$) given by numerical simulation. Outline of fin is overlaid. Dashed lines represent survey locations in the Mach 3 tunnel. . .	5-10
5.11. Flow at $x=0.69c$ measurement plane given by numerical simulation and experiment.	5-11
5.12. Effect of $\Delta z=-1\text{mm}$ on flow angularity; convex side of fin.	5-12
5.13. Stagnation pressure iso-surfaces and streamlines in juncture vortex region on convex side of the fin.	5-13
5.14. Concave measurement plane ($z=-0.47c$) pressure contours and mass-flux streamlines ($\rho u, \rho v$) given by numerical simulation. Outline of fin is overlaid. Dashed lines represent survey locations in the Mach 3 tunnel. . .	5-14
5.15. Effect of $\Delta z=+1\text{mm}$ on flow angularity; concave side of fin.	5-15
5.16. Computed inviscid fin surface pressures.	5-17
5.17. Computed viscous turbulent (Baldwin-Lomax) fin surface pressures. . .	5-17
5.18. Turbulence intensity profiles.	5-19
5.19. Turbulent kinetic energy, K_c	5-20
5.20. Turbulent kinetic energy, K_c	5-20
5.21. Measured turbulent shear stresses, $\tau_{ij}^T = -\frac{(\rho u_i)'(\rho u_j)'}{\bar{\rho}} + \bar{\rho} \overline{u_i' u_j'} \left(\frac{\rho'}{\bar{\rho}}\right)^2$. . .	5-21
6.1. Computed inviscid test section surface pressures (at $M=5.0$).	6-2
6.2. Shadowgraph of fin region ($M=4.9$).	6-3

Figure	Page
6.3. Schlieren photograph ($M=4.9$).	6-3
6.4. Computed pitot pressure and secondary streamlines at $M=2.8$ measurement plane, and at present measurement plane ($x=0.84c$).	6-4
6.5. Experimental and numerical pitot pressure.	6-5
6.6. Computed pressure and mass-flux streamlines ($\rho u, \rho v$) on measurement planes ($M=4.9$). Outline of fin is overlaid. Dashed lines represent survey locations.	6-6
6.7. Stagnation pressure iso-surfaces and streamlines in juncture vortex region on convex side of the fin.	6-6
6.8. Computed limiting surface streamlines at $M=4.9$	6-7
6.9. Computed inviscid fin surface pressures.	6-8
6.10. Computed viscous turbulent (Baldwin-Lomax) fin surface pressures. . .	6-9
6.11. Computed rolling moments.	6-9
B.1. Sample two-film calibration using <i>King's Law</i>	B-2
C.1. Comparison of hot-wire probe orientation at $x=0.69c$ ($M=2.8$).	C-8
C.2. Effect of a variation in probe position on computed pitot pressure ($M=2.8$). . .	C-9
C.3. Effect of a variation in probe position on θ ; convex side ($M=2.8$).	C-10
C.4. Effect of a variation in probe position on ϕ ; convex side ($M=2.8$).	C-10
C.5. Effect of a variation in probe position on θ ; concave side ($M=2.8$).	C-11
C.6. Effect of a variation in probe position on ϕ ; concave side ($M=2.8$).	C-11
D.1. Mach 5 wind tunnel schematic.	D-2
D.2. High pressure air tank.	D-3
D.3. Air control panel.	D-3
D.4. Compressor and dryer.	D-4
D.5. Mach 5 wind tunnel pebble bed heating system.	D-5
D.6. Wind tunnel nozzle (dimensions in inches).	D-6

Figure	Page
D.7. Wind tunnel nozzle and test section. Shown with nozzle wall removed for visibility and window replaced by aluminum plug for initial tunnel calibration.	D-7
D.8. Wind tunnel test section wall with windows (dimensions in inches). . .	D-8
D.9. Wind tunnel ceiling with model insert (dimensions in inches).	D-9
D.10. Wind tunnel floor with probe access (dimensions in inches).	D-9
D.11. Measured pitot pressure at upstream location.	D-10
E.1. Space marched zone inflow boundary condition for and exit.	E-1

List of Tables

Table	Page
3.1. Mach 3 tunnel freestream inflow conditions.	3-4
3.2. Data acquisition system parameters.	3-10
4.1. Freestream conditions used for Euler calculations.	4-3
4.2. Computational requirements for Mach 2.8 RANS calculations.	4-13
4.3. Computational requirements for Mach 4.9 RANS calculations.	4-13
C.1. Measurement error bounds.	C-3
C.2. Freestream conditions.	C-4
C.3. Typical freestream hot-film parameters (M=2.8).	C-4
C.4. Pressure probe related error bounds.	C-6
C.5. Hot-film related error bounds (M=2.8).	C-7
C.6. Turbulent fluctuation error bounds (M=2.8).	C-7
D.1. Typical Mach 5 tunnel freestream conditions (used for viscous CFD). .	D-1

List of Symbols

a	=	local speed of sound
a_k, b_k	=	constants for <i>King's Law</i>
d	=	diameter of cylindrical hot-film probe
c	=	chord length of missile fin, 2.03cm
Cm_x	=	rolling moment coefficient about missile axis, $8M_x/\rho U \pi D^3$
C_p	=	specific heat coefficient at constant pressure
C_v	=	specific heat coefficient at constant volume
E	=	total internal energy
e	=	internal energy per unit mass
H	=	total enthalpy
h_0	=	stagnation enthalpy per unit volume
i	=	current
k	=	thermal conductivity
k_0	=	power law reference conductivity
ℓ	=	reference length
ℓ_f	=	hot-film length
M	=	Mach number
M_e	=	Mach number at boundary layer edge
m_i^T	=	turbulent mass components
n	=	direction normal to surface
Nu	=	Nusselt number
P	=	static pressure
P_{10°	=	10° cone-static pressure
P_{20°	=	20° cone-static pressure
P_{t2}	=	pitot pressure
Pr	=	Prandtl number
Pr_t	=	turbulent Prandtl number
q_i	=	heat flux components
q_∞	=	freestream dynamic pressure

q_f	=	hot-film power and heat transfer
R	=	gas constant
R_0	=	mass flux ratio, $\overline{\rho v}/\overline{\rho u}$
R_{ref}	=	hot-film resistance at reference temperature
R_f	=	hot-film operating resistance
R_s	=	anemometer resistance in series with hot-film
R_L	=	hot-film lead resistance
r	=	model fin radius of curvature, 1.59cm
Re	=	reference Reynolds number, $\frac{\rho_\infty u_\infty \ell}{\mu_\infty}$
Re_e	=	effective Reynolds number, $\frac{\rho U d}{\mu_0} \cos \varphi$
t	=	time
T	=	temperature (K)
T_f	=	hot-film temperature
T_e	=	equilibrium hot-film temperature
U	=	magnitude of velocity vector
\vec{U}	=	velocity vector
u_τ	=	friction velocity, $\sqrt{\frac{\tau_w}{\rho_w}}$
u^+	=	inner turbulent velocity \bar{u}/u_τ
u, v, w	=	mean Cartesian velocity components
u_1, u_2, u_3	=	u, v, w
E_f	=	hot-film voltage
x, y, z	=	Cartesian coordinates
Y	=	distance from body surface y direction
y^+	=	inner turbulent coordinate yu_τ/ν
α	=	$T/T_t = [1 + \frac{1}{2}(\gamma - 1)M^2]^{-1}$
β	=	$(\gamma - 1)\alpha M_\infty^2$
γ	=	ratio of specific heats, 1.4 for air
δ	=	boundary layer thickness, defined by location where $M=0.95M_e$
δ_0	=	reference boundary layer thickness at $M=2.8$ (6.1mm)
δ_∞	=	reference boundary layer thickness at $M=4.9$ (10.2mm)

\mathcal{E}_X	=	error associated with measurement of X
ε_X	=	normalized uncertainty associated with the measurement or calculation of X
ν	=	molecular kinematic viscosity, μ/ρ
ρ	=	density
τ	=	hot film temperature loading factor
τ_{ij}	=	shear stress tensor components
τ_{ij}^T	=	turbulent shear stress tensor components
θ	=	horizontal flow angularity, $\tan^{-1}(v/u)$
ϕ	=	azimuthal flow angularity, $\tan^{-1}(w/u)$
φ	=	hot-film incidence angle

Subscripts

e	=	equilibrium
f	=	hot-film
L_2	=	Euclidean norm
max	=	maximum
ref	=	reference
t	=	total condition
w	=	wall
$,i$	=	partial derivative in x_i direction
∞	=	free stream condition

Superscripts

$()^T$	=	turbulent
$()'$	=	Reynolds fluctuating component
$()''$	=	Favré fluctuating component
$\overline{()}$	=	Reynolds averaged component
$\widetilde{()}$	=	Favré averaged component

CHARACTERIZATION OF THE FLOWFIELD NEAR A WRAP-AROUND FIN AT SUPERSONIC SPEEDS

1. Introduction

1.1 *Wrap-Around Fins*

Wrap-around fins (WAFs) have been used by designers for several years on low-speed tube launched missiles and dispenser-launched sub-munitions. The term "wrap-around fin" usually refers to a projectile stabilizing or control surface, which has the same curvature as the missile body, and can be *wrapped around* the projectile until deployment (see Figure 1.1). Since stealth capability has become a design parameter for many aircraft, WAFs have become even more attractive for their reduced cross-section and stowability. Wrap-around fins can also simplify the design of airframes that integrate the weapon in partial concealment, avoiding complications associated with fin-fuselage contact.

While WAFs enable several design possibilities, several stability anomalies are inherent for missiles employing them^[1, 6, 52, 113, 119], the most recognized of which is a roll reversal observed near transonic conditions. Also due to the asymmetric fin geometry, missiles with WAFs display a pitch-yaw coupling at all speeds not present on conventional missiles. During recent ballistic range tests^[1, 113], a second rolling moment reversal was observed over a small range of high supersonic speeds ($M \approx 4.5-4.7$) on a WAF configuration. In this regime, yawing moment reversals were also detected. Vitale and Abate^[113] have proposed that this loss of static stability may be related to the complex shock structure in the fin region. Cross-flow induced by missile pitch and spinning may also be a contributing factor. Interaction with the missile bow shock is also plausible at high pitch angles.

The majority of WAF experiments have focused on ascertaining stability characteristics via sub-scale flight tests^[4, 5, 6, 52, 104, 113, 117], most of which emphasized the subsonic

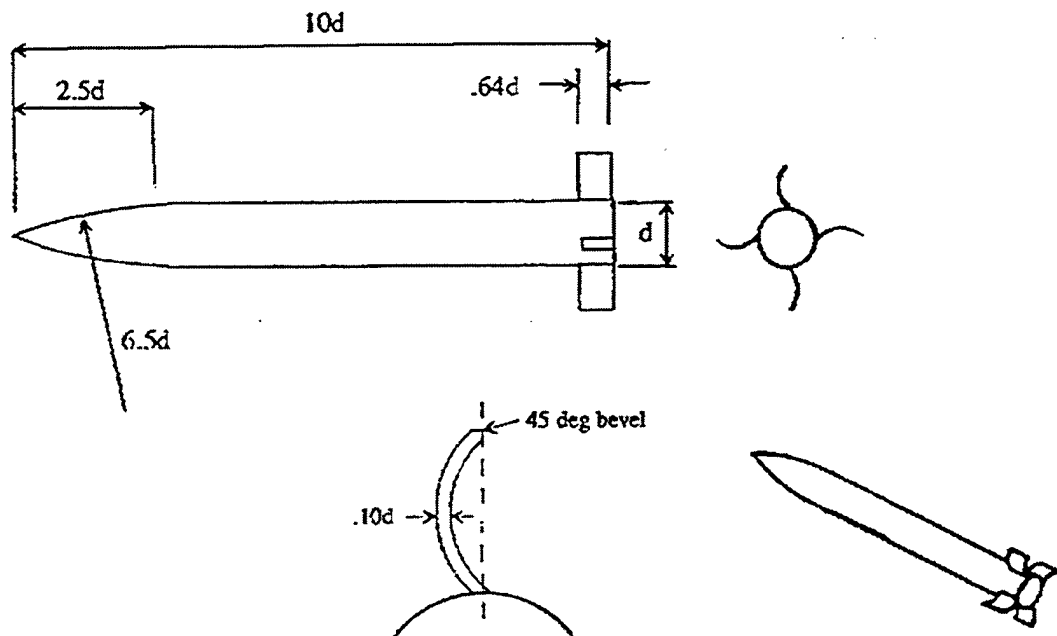
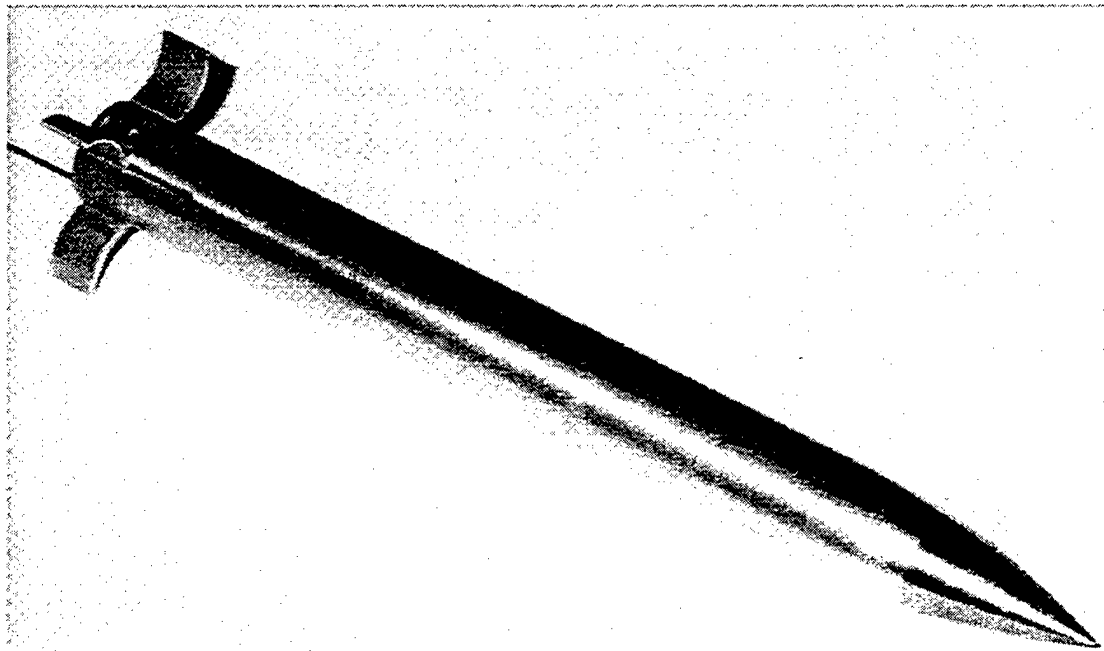


Figure 1.1 Typical WAF missile configuration (Vitale & Abate 1992).

and transonic flight regimes^[4, 5, 6, 52, 117]. These experiments provide no detailed flowfield measurements, and do little to promote an understanding of the flowfield.

A small number of numerical simulations have been performed on missiles employing wrap-around fins. Some have focused on the design of lift and control surfaces by simulating the fin alone^[58]. However, the majority of these simulations have focused on characterizing the structure of the fin shocks and their interaction. The Euler equations were solved by Vitale, et al.^[113] on a swept WAF configuration with no fin thickness. The Euler equations have also been solved by Abate and Cook^[3] for subsonic, transonic, and supersonic flow conditions on a WAF configuration using unswept 10% bi-convex airfoils. While such inviscid simulations have been able to predict the existence of the sonic rolling moment reversal, they have failed to predict the second rolling moment reversal at high Mach numbers. More recently, Edge^[28] has solved the laminar Navier-Stokes equations over a WAF geometry with a relatively low fin aspect ratio and a round leading edge for Mach numbers ranging from 1.3 to 3.0. To date, no WAF geometry has been simulated using turbulence models.

1.2 Objectives of Present Research

The primary goal of the present research was to characterize the flow structure near WAFs at high supersonic speeds. This would be accomplished through a systematic numerical and experimental analysis of the mean and turbulent flowfield in the vicinity of a single WAF. An understanding of the flowfield near WAFs is critical to further development of such configurations, given the dependence of stability characteristics on Mach number. Determination of the flow structure near a single non-spinning WAF is an essential first step toward this understanding.

A second objective was to contribute a complete set of mean flow and turbulence data on this shock/boundary-layer interaction flowfield for numerical turbulence model validation. The data gathering criteria of Settles and Dodson^[96] has been used for guidance. Prior to this study, no detailed flowfield measurements (mean flow or turbulence) existed for WAF missile configurations.

Finally, the suitability of a widely used commercial simulation package, the General Aerodynamic Simulation Program (GASP)^[7], with the turbulence model of Baldwin and Lomax^[11] was to be investigated for this flowfield.

1.3 Overview of Present Research

As a first step toward understanding the flow structure near WAFs, a simple model has been investigated which consists of a single wrap-around fin mounted on a partial fuselage (Figure 3.1). This simplified model allowed experimental data to be obtained at much higher resolution than would have been possible on a full-body four-finned configuration scaled to fit in the available tunnel space. Also, the single-WAF static model isolates the effects of fin curvature from the effects of upstream cross-flow and interaction of the multiple fin shocks. The flow around this single-WAF configuration has been investigated both numerically and experimentally, with the objective of quantifying the flow structure in the region near the fin/body juncture. Numerical and experimental results are examined and compared to gain an understanding of the flow-field in the vicinity of a WAF.

Measured flowfield data were obtained in the AFIT Mach 3 wind tunnel and in the new AFIT Mach 5 wind tunnel on a model composed of a single wrap-around fin on a ceiling-mounted semi-cylindrical fuselage. Shadowgraph and schlieren photographs were also obtained for flow visualization. In the Mach 3 wind tunnel, the flow around the test article was surveyed at several stations along its length, concentrating on the region near the fin. The flowfield was also explored with the model in wall-mounted configurations to enable measurements closer to the fin surface. Detailed mean flow measurements were obtained using conventional cone-static and pitot pressure probes, as well as hot-film cross-wire probes. The flow data measured with the hot-film probes were also used to estimate turbulence quantities using the hot-film anemometry methods outlined by Bowersox and Schetz^[14, 13, 16]. These techniques have been used recently in several experiments^[26, 74, 75, 94] to quantify the effects of pressure gradients on turbulent boundary layers. In the Mach 5 tunnel, mean flow (pressure) measurements, as well as shadowgraph and schlieren photography were obtained.

Experimental data were compared to numerical results obtained with a widely used numerical simulation package (GASP v3.06^[7]) employing the Baldwin-Lomax^[11] algebraic turbulence model. Taken in concert, the experimental and numerical information are examined with a view toward characterizing the net effect of the complex flowfield in the vicinity of the WAF on aerodynamic loading.

1.4 Outline of Document

This section provides a road map of the chapters that follow. First, Chapter 2 provides a survey of research that has been directed toward the solution of other shock/boundary-layer interaction flows sharing some characteristics of the flowfield near supersonic wrap-around fins. The experimental methods used in this investigation are outlined in Chapter 3. Details relating to the reduction of hot-film anemometry data are presented in Appendix B. The uncertainty of these measurements and an analysis of the effect of these uncertainties on the presented results are provided in Appendix C. Chapter 3 also details the facility, apparatus, instrumentation, and model used to obtain the experimental results at Mach 3. A more detailed description of the Mach 5 wind tunnel constructed for this research is included in Appendix D. The numerical strategy used is outlined in Chapter 4, and the governing equations and turbulence model that were employed are detailed in Appendix A. The results of the experimental and numerical investigations at Mach 2.8, including an analysis of the flowfield near the fin, are presented in Chapter 5, while the results at Mach 4.9 are presented in Chapter 6. A set of conclusions and recommendations for further study are given in Chapter 7.

2. Background

In the mid-1960's research on shock interactions was motivated by a desire to quantify the extreme heating loads imparted on bluff bodies by single and multiple impinging shock waves. Heirs and Loubsky^[39] investigated the effects of shock impingement on a cylindrical leading edge in a shock tunnel at supersonic speeds, though the experimental tools of the day limited the accuracy of their heating rate measurements. Meanwhile, Edney^[29] was identifying and categorizing the flowfield structures produced by shock/shock interactions for several shock-generating geometries. The need for improved high-speed bluff body aerodynamic and heating prediction methods for the Shuttle project led to several experimental investigations. Holden^[41, 80] provides a historical review of several of these experiments involving single and multiple shock interactions as they effect aerothermal heating loads. This chapter surveys the experimental and numerical investigations on configurations that exhibit similar flowfield characteristics to those observed in the vicinity of supersonic wrap-around fins, beginning with a discussion of blunt unswept fins.

2.1 Blunt Unswept Fins

Over the past three decades, several efforts have been directed toward understanding and accurately predicting flows having shock/boundary-layer interactions. Efforts have included experimental explorations to obtain a detailed knowledge of the flowfield, as well as computational studies aimed at developing and validating numerical methods and turbulence models for such flows.

The present research has been directed toward detailing the flow structure in the vicinity of a curved fin. It was anticipated that this flow structure would be fundamentally different from the oft-studied flow around blunt unswept fins, given the significant cross-flow component of the mean flow induced by the geometric asymmetry. However, the flowfields over the two geometries share several common attributes, and an understanding of the more fundamental flows over straight-fins aids interpretation of the flow characteristics near wrap-around fins.

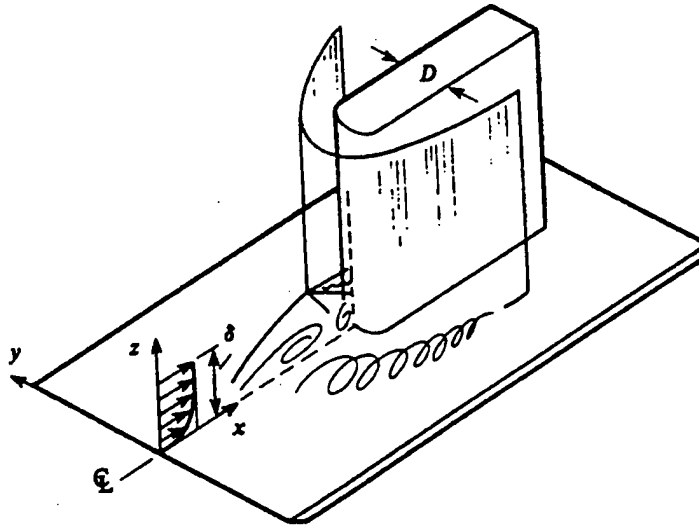


Figure 2.1 Sketch of flow interference near a blunt fin (Hung and Kordulla, 1984).

One commonly studied geometry of particular relevance to the current research is a blunt unswept fin of constant thickness and a rounded leading edge mounted on a flat plate (Figure 2.1). The bow shock produced by the blunt fin forces the incoming plate boundary layer to separate. This separation creates an oblique shock which interacts with the bow shock at a location away from the fin root (Figure 2.2). A supersonic jet forms due to the Edney^[29] Type IV interference associated with the interaction of the separation shock and the bow shock. The entire structure is referred to as the 'λ-shock' pattern. This shock pattern and the associated vortical flowfield are also produced ahead of a cylinder extending from a flat plate in supersonic flow.

2.1.1 Experimental Investigations. As early as 1967, Price and Stallings^[87] investigated supersonic turbulent separated flows in the vicinity of fin-type protuberances. In the decade following, several other experimental investigations on blunt fins in supersonic flows were conducted, most notably by Kaufman, et al.^[50], Sedney and Kitchens^[92, 93], Dolling and Bogdonoff^[24], Ozcan^[82, 83], Saida and Hattori^[91], Fomison^[33, 34], and Settles^[95].

Sedney and Kitchens^[92, 93] experimentally studied the flow near cylinders mounted on a flat plate. The cylinder height and diameter were varied, as well as Mach number ($1.5 < M < 4.5$) and unit Reynolds number ($2 \times 10^6 \text{ m}^{-1} < \text{Re}/\ell < 19.3 \times 10^6 \text{ m}^{-1}$). They found

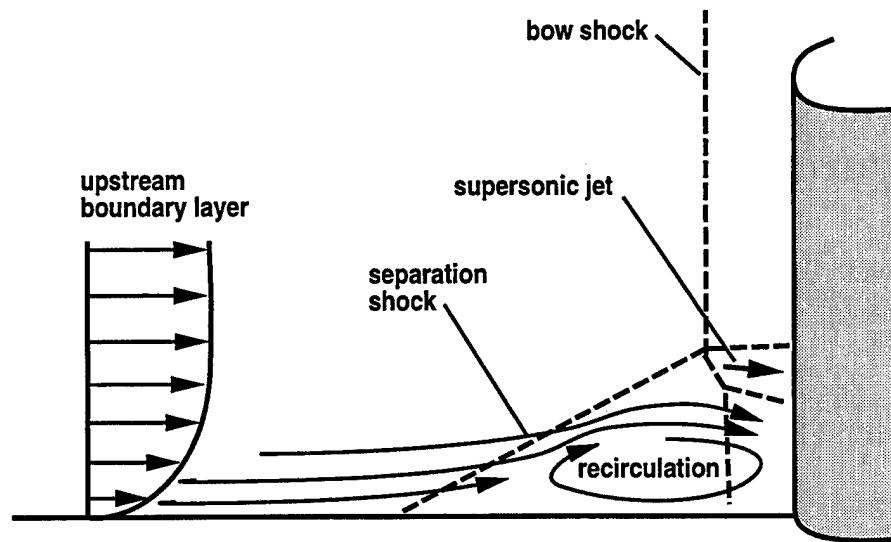


Figure 2.2 The shock structure on symmetry plane ahead of a blunt fin.

that 2, 4, or even 6 vortices could evolve around the juncture at a given Mach number, depending on the unit Reynolds number. The number of vortex pairs generally decreased with increasing Reynolds number. The details of how this structure varies with Re/ℓ is different for each Mach number. However, the unit Reynolds number (and hence number of vortices) was found to have little effect on the location of the primary separation or attachment lines in front of the obstacle.

Dolling and Bogdonoff^[24] demonstrated (using data from several experiments^[50, 87, 120]) that over a large range of Mach number and incoming boundary layer thicknesses (δ/D), the leading edge diameter (D) was a suitable scaling parameter for the centerline plate pressure ahead of the fin. The upstream influence was always found to be between two and three diameters upstream. They also showed that for a given Mach number ($M=3$, $Re/\ell=65 \times 10^6 \text{ m}^{-1} \pm 5\%$), the entire flat plate surface pressure is scaled by the leading edge diameter.^[24] This correlation was later corroborated by Fomison.^[33, 34] It was found that even the leading edge surface pressure ratios were correlated with y/D for a given Mach number, provided that the shock wave structure was well clear of the boundary layer (i.e., $\delta/D \leq 4$). In essence, Dolling and Bogdonoff showed that the spatial extent of the interaction near a straight unswept fin is dominated by inviscid characteristics of the flow.

Fomison^[33, 34], investigating blunt unswept fins with a semi-cylindrical leading edge extending from a flat plate, detailed the effect of fin thickness and incidence on the flow ($M_\infty=2.4$, $Re/\ell=2.6\times 10^6\text{m}^{-1}$). His oil flow visualizations showed that both thick and thin fins produced the same number of vortices (4 at this relatively low Re/ℓ). This was consistent with the hypothesis of Sedney and Kitchens^[92, 93] that the number of vortices was driven by the unit Reynolds number, and not obstacle size. Fomison's oil flow experiments also demonstrated that fin incidence can have a dramatic effect on the flow topology. It was conjectured that at sufficiently high incidence angles, a secondary separation would appear on the wall. This has been shown to occur for sharp swept fins at high incidence angles.^[33] Stollery^[80, 103] has reviewed several experiments which generate flows involving glancing shock/boundary layer interactions, including blunt unswept fins, and has compiled a fairly complete bibliography of the related work.

2.1.2 Numerical Investigations. The flow over a blunt unswept fin appears to have been first solved numerically by Hung, Kordulla, and Bunning^[46, 47] in the mid-1980's ($M=2.95$, $Re/\ell=63\times 10^6\text{m}^{-1}$). They demonstrated good agreement between their Reynolds averaged Navier-Stokes (RANS) solutions and experimental surface pressure distributions obtained by Dolling and Bogdonoff.^[24] Small topology differences were probably due to limited grid resolution.

Soon after, McMaster and Shang^[73] numerically simulated this flow by solving the Favré (mass) averaged Navier-Stokes (FANS) equations with an algebraic turbulence model ($M=2.95$, $Re/\ell=64\times 10^6\text{m}^{-1}$). While the primary focus of this effort was to investigate the effect of fin sweep on the flowfield, solutions obtained on the un-swept fin were similar to those of Hung and Bunning^[46], with the separation line on the plate agreeing slightly better with experimental results. Kubendran, et al.^[59] obtained similar results, and designed a leading-edge fillet that eliminated the leading edge flow separation.

In the early 1990's, Knight^[54, 81] reviewed the available numerically-oriented three-dimensional shock/turbulent boundary layer interaction literature. He considered five basic interactions, assessing the numerical capability of the simulation methods by comparison with available experimental data. One of these interactions was induced by a blunt unswept

fin on a flat plate. At the time of his article, only algebraic turbulence modeling had been employed in any calculations reported over this geometry. Also, while the separation shock wave has been observed to be an unsteady feature^[23, 24, 25], he noted that all computational simulations of the supersonic blunt fin problem were steady, suggesting that this may have been due to inadequate grid resolution or inaccuracies in the turbulence models.^[54] Since the experimentally observed unsteadiness of the flowfield involves dominant frequencies on the order of 1 kHz^[92], direct or large-eddy turbulence simulations would be required to resolve the unsteady flowfield computationally.^[46] Only the time-averaged 'mean' solutions have been sought to date, which are much more economically obtained.

Since Knight's review, Chima and Yokota^[21], Chen and Hung^[20], and Rizzetta^[88] among others have numerically simulated the flow around a cylinder/flat-plate juncture using various methods. While the first two of these studies used algebraic eddy viscosity models with an ad hoc modification to the length scale to account for the multiple intersecting solid surfaces, Rizzetta^[88] employed the two equation k - ϵ turbulence model of Jones and Launder^[48], including low Reynolds number terms ($M=2.5$, $Re/\ell=19.3\times 10^6 m^{-1}$). The results agreed very well with experimental results – somewhat better than did the results of Chen and Hung^[20]. This was probably due in part to higher grid resolution and strategic grid clustering. Only one vortex pair was predicted, while three pairs were experimentally observed by Sedney and Kitchens^[92, 93]. Haidinger and Friedrich^[37] were also unable to accurately reproduce the upstream effects of the shock induced separation using Wilcox's k - ω closure model^[118]. However, the downstream predictions of pressure distribution and skin friction were reasonable. In general, recent efforts to assess the viability of numerical methods for the simulation of similar complex flows^[12, 27, 35, 49, 76] have met with varying degrees of success.

2.2 *Experimental Turbulence Measurements*

Settles and Dodson^[96] recently proposed a set of criteria for experimental data gathering and reporting. Adherence to these criteria is considered necessary in order for the data to be useful for CFD research on supersonic turbulent shock/boundary layer interactions. They advocate inclusion of each experiment satisfying these criteria in a database

to be put forth as a standard for CFD code validation and turbulence model development. The primary focus of these criteria is to provide to the CFD community all of the necessary data required to numerically simulate the experiment. These criteria have been adopted as guidance for the current research effort.

As reported by Settles and Dodson, a great number of experiments have been targeted at measuring turbulent quantities in interacting flows. However, most of these experiments do not meet the high standards required for modern code validation. In fact, at the date of publication, they found only 19 experiments which met their criteria, none involving blunt fin-type geometries. Most experiments were rejected because they were not able to provide data useful for testing turbulence models. Others failed to report error bounds, the incoming boundary layer profile, or simply did not provide the data in a useful form. Their survey rejuvenated efforts to obtain such critical data.

Seven of the experiments accepted into this database considered the interaction between sharp fin-like geometries and flat plates. [43, 51, 55, 60, 61, 62, 63, 64, 65, 89] However, among these experiments, flowfield data are scarce, and field turbulence data are even more rare. The current study represents a continuance of the experiments accepted to date by introducing surface and shock-generator curvature effects, and thus provides experimental data that do not presently exist.

3. Experimental Methodology

This chapter outlines the tools and methods used to extract meaningful flowfield information. Instruments include pitot pressure probes, cone-static pressure probes, and hot-film cross-wire probes. The pressure probes determine mean flow information such as density, pressure, and velocity magnitude. The hot-film cross-wire probes determine velocity components and turbulence values in a form which, when manipulated, are useful for comparative analysis to results obtained numerically.

3.1 WAF Model

The WAF model (Figure 3.1) is comprised of a cylinder of the fin radius, $r=1.59\text{cm}$, blended to a removable test section wall, and has a maximum height of $0.5r$. It is designed to represent a single fin of a typical WAF configuration, and sized to maximize data resolution while avoiding tunnel blockage. The fin has the same proportions as free-flight models which have been tested at the Wright Laboratory Armament Directorate^[1, 113], with a thickness of $0.2r$ (3.18mm), a span of $\sqrt{2}r$ (22.5mm), and a chord length, c , of $1.28r$ (20.3mm). The leading edge and tip of the fin are beveled at 45° . The cylinder is 5.12 fin radii in length with the single fin placed at the downstream base. Upstream, the cylinder is blended to the tunnel floor with a polynomial chosen to ensure second order continuity in the streamwise direction. The blending region is $5r$ long and starts $21.48r$ from the throat of the wind tunnel nozzle.

3.2 Mach 3 Wind Tunnel

The AFIT Mach 3 wind tunnel (Figure 3.2) is an intermittent blow-down tunnel with downstream evacuation. The maximum run time for the tunnel was 30 seconds with an evacuation time of 6 to 10 minutes. The nozzle measures 27.3cm from throat to test section entrance. The test section is 33.0cm long with a square 6.35cm cross-section. The settling chamber total pressure and temperature are 2.0–2.14atm and 294K respectively, yielding a freestream Reynolds number of $Re/\ell=17\text{--}18\times 10^6\text{m}^{-1}$. Figure 3.3 is a photo of the nozzle and removable test sections with the side-walls removed for visibility.

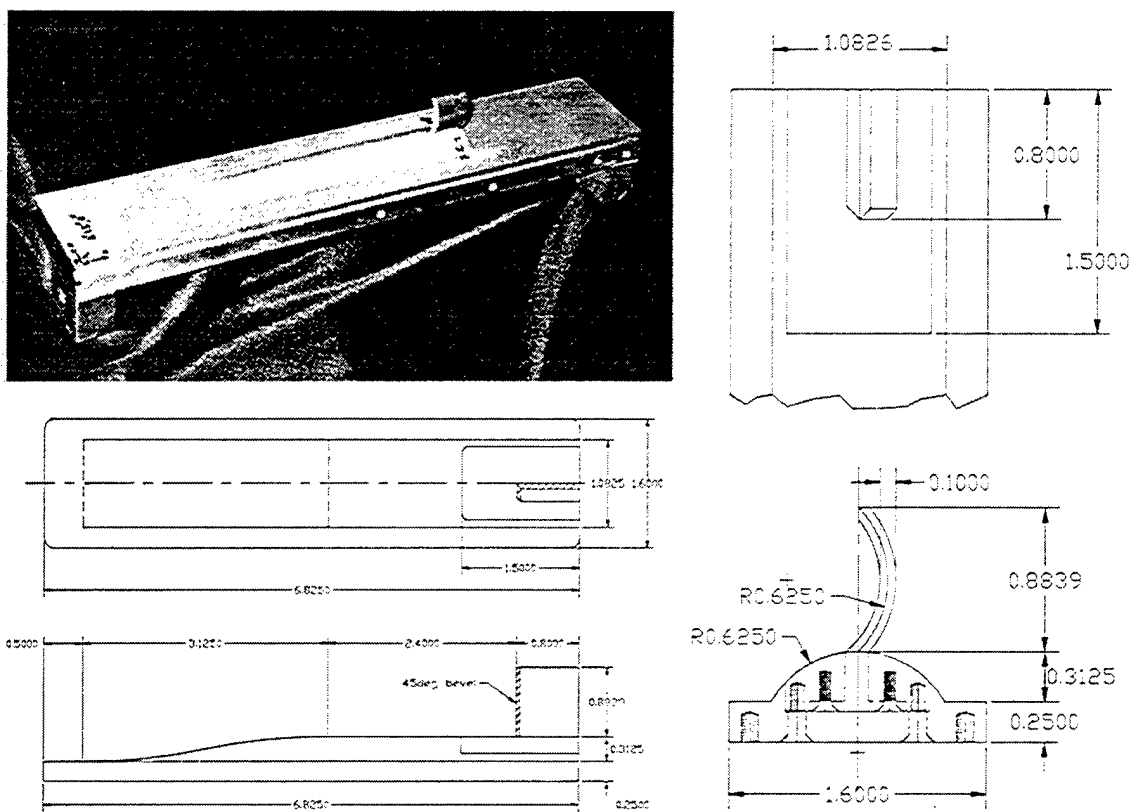


Figure 3.1 Single wrap-around fin model (dimensions in inches).

3.2.1 Operating Conditions. Detailed pitot and cone-static measurements had been previously obtained in an empty test section and used to determine the mean inflow conditions for the test section.^[75] From this survey, the freestream Mach number was determined to be 2.9 ($U_e=607\text{m/s}$). Results from this earlier experiment were used to specify the upstream boundary conditions for the preliminary inviscid numerical simulation.^[109]

During the present research (with the model in the tunnel), the test section entrance conditions were again surveyed. It was determined that at a location just downstream of the test section entrance (8.4c ahead of the fin leading edge) the freestream Mach number was 2.80 ($U_e=601\text{m/s}$), with a measurement uncertainty of 2.8%. The boundary layer on the tunnel ceiling at a location 1.27cm upstream of the model has a measured thickness of 5.3mm at the centerline, defined by the distance from the surface where $M=0.95\% M_e$. A summary of measured freestream mean-flow conditions are presented in Table 3.1.

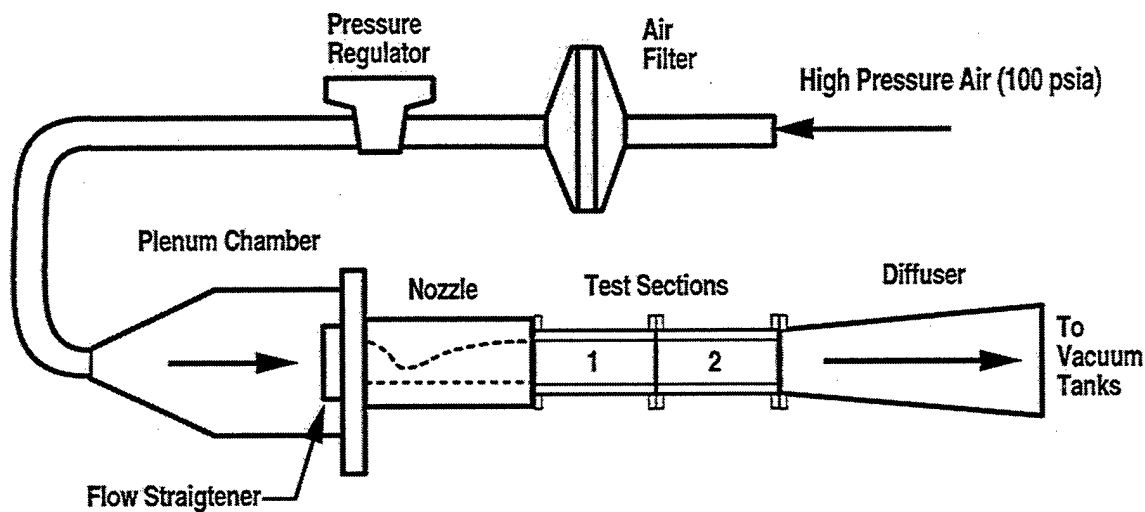


Figure 3.2 Mach 3 wind tunnel schematic.

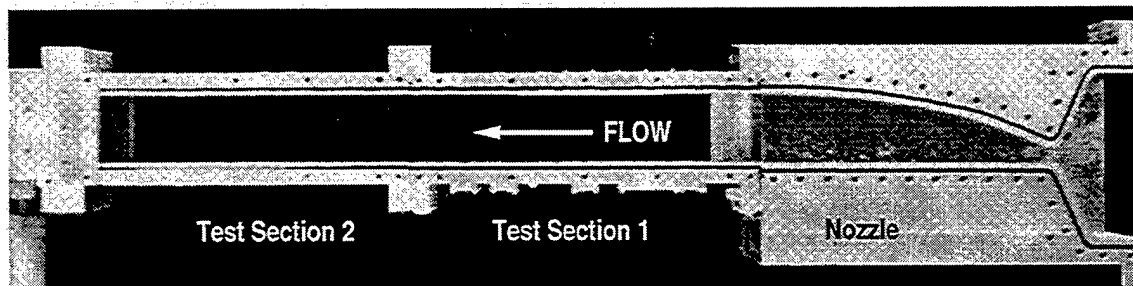


Figure 3.3 AFIT Mach 3 wind tunnel.

3.2.2 Tunnel Instrumentation. Instrumentation for the Mach 3 tunnel included an internal pitot tube and thermocouple in the plenum chamber to measure $P_{t\infty}$ and $T_{t\infty}$. The thermocouple (K-type, Omega part no. SEFE-K-5) had an accuracy of $\pm 1K^{[32]}$, and the pitot (total) pressure was fitted with a 6.7atm pressure transducer (Endevco model 8510C-100).

3.2.3 Traversing Equipment. The probe traverse system used in the Mach 3 tunnel used a stepper motor with 400 steps per revolution. The slide moves on a shaft of 40 threads per 2.54cm, has a total travel distance of 16.51cm, and moves at a maximum speed of about 0.254 cm/sec.^[74] A photograph of the traversing assembly is provided in Figure 3.4 (courtesy of Miller^[74]). Traverse control is accomplished via personal computer.

Table 3.1 Mach 3 tunnel freestream inflow conditions.

Condition	Value
M	2.80
P_t	217kPa = 2.14atm
P	7.99kPa = 0.0789atm
T_t	294K
T	114.5K
u	$601 \frac{m}{s}$
ρ	$0.2431 \frac{kg}{m^3}$

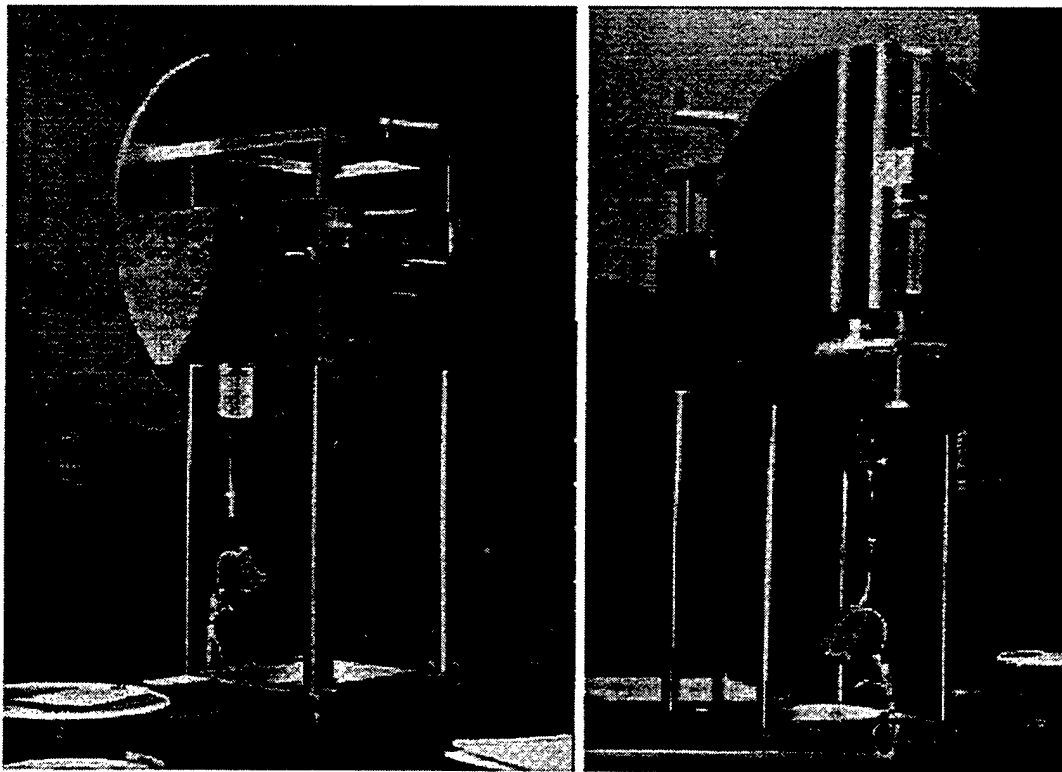


Figure 3.4 Traverse assembly (Miller).

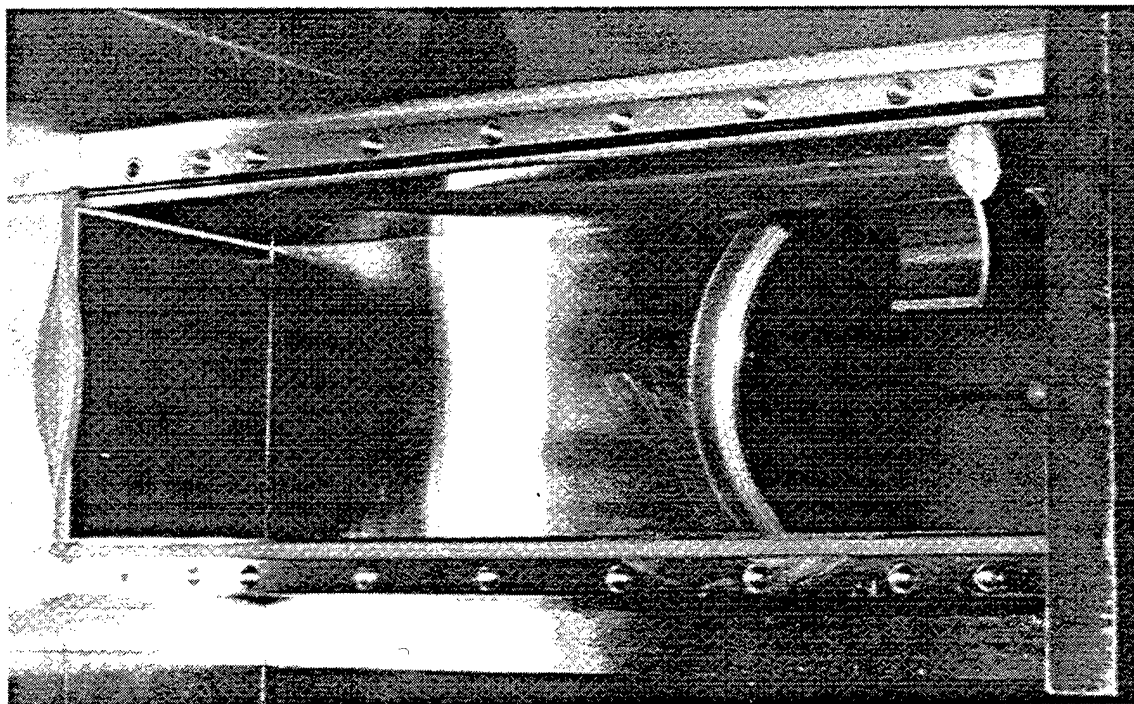


Figure 3.5 AFIT Mach 5 wind tunnel with WAF model.

3.3 Mach 5 Wind Tunnel

Experimental results were also obtained in the new AFIT Mach 5 wind tunnel (Figure D.1). This blow-down wind tunnel has a heated air supply and has been operated over a range of unit Reynolds numbers ($Re/\ell \approx 32-75 \times 10^6 \text{m}^{-1}$). Although the tunnel is capable of producing much longer run-times, the current experiments only required total run-times of 10-15 seconds. The design, construction, instrumentation, and initial calibration of this facility comprised a significant portion of this research effort. More detailed information on the AFIT Mach 5 wind tunnel is available in Appendix D.

3.4 Pressure Probes

A pitot probe and a $10^\circ (\pm 0.03^\circ)$ cone-static probe were used to measure pressures throughout the flowfield in the Mach 3 wind tunnel (Figure 3.6). Total and static pressure data are obtained directly from the pitot and cone-static probes through normal and axisymmetric oblique shock relations. These data can be used to calculate mean flow information such as Mach number, density, and the magnitude of the velocity. Through

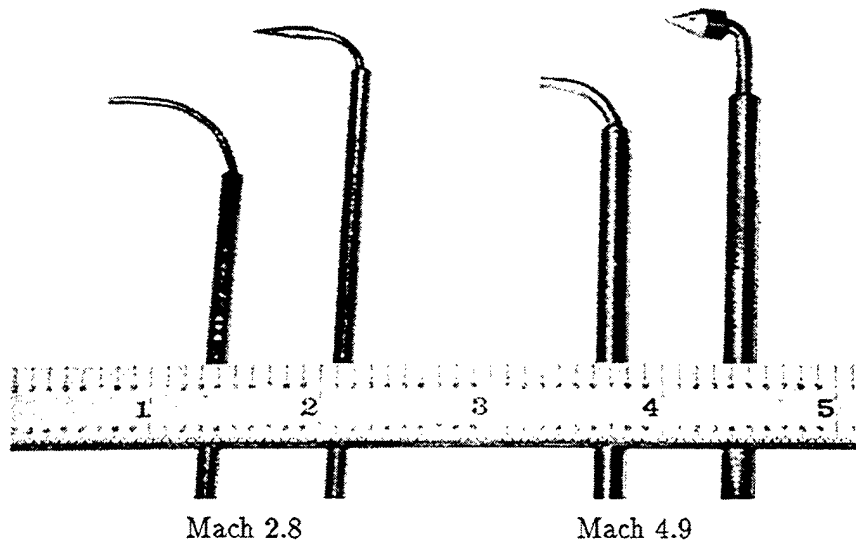


Figure 3.6 Pressure probes.

the manipulation of results from conical^[9, 56] and normal shock relations^[10], the following curve fit was proposed by Bowersox.^[13]

$$\frac{1}{M} = -0.052976 + 4.6840\xi_{10^\circ} - 18.6786\xi_{10^\circ}^2 + 50.7006\xi_{10^\circ}^3 - 54.1577\xi_{10^\circ}^4 \quad (3.1)$$

where ξ_{10° is defined as the ratio of the pressure measured with the 10° cone-static probe to the pitot pressure ($\xi_{10^\circ} = P_c/P_{t2} = fcn[M]$). It has been found that for flow angles less than 6.0° the errors in Mach number are less than 0.03.^[113] Also note Equation 3.1 is valid for Mach numbers in the range from 1.5 to 4.4 and has a standard deviation of 0.06%.^[13]

Stronger pitot and cone-static probes than those used in the Mach 3 tunnel were fabricated from heavy gauge stainless steel to withstand the higher loads associated with the Mach 5 tunnel. This cone-static probe had a semi-vertex angle of 20° , which produces higher measured pressure levels than the 10° probe, enabling more accurate readings. The higher cone angle also minimized the error due to flow angularity. For this new cone angle, and to envelope the higher Mach number range, a new relationship between Mach number and the measured pressures was needed. Again, conical and normal shock solutions were used to develop a direct relationship between Mach number and the ratio of measured

pressures.

$$\frac{1}{M} = 0.3469176 + 0.908347\xi_{20^\circ} - 0.0518062/\xi_{20^\circ} \quad (3.2)$$

This relationship is valid for Mach numbers between 1.5 and 6.5 with a correlation coefficient of 99.990%. Note that this form provides monotonic behavior at high pressure ratios (low Mach numbers), and is nearly as accurate within the range of validity as a fourth-order polynomial.

With the exception of the Mach 5 pitot pressure, all probes were connected with tubing to a 1atm transducer (Endevco model 8510C-15), which sent its signal to a signal processor (Endevco model 4428A). This unit uses the maximum range of the pressure transducer, is self-zeroing, and connects directly to the data acquisition system (Section 3.6). The Mach 5 pitot pressure was sensed with a 6.7atm transducer (Endevco model 8510C-100). Atmospheric pressure was recorded using a Druck resonant sensor barometer.

3.5 Hot-Film Cross-Wire Probes

Presented here is a brief overview of the hot-film cross-wire probes and the associated data reduction techniques. More details on the hot-film anemometry methods employed to determine both mean and turbulent flow information are provided in Appendix B.

Two hot-film probes (Figure 3.7) were used to determine the velocity and fluctuations of the flow in the Mach 3 tunnel. Both probes were two-component cross-wire hot-film probes, each with two thin films of platinum 1mm long and $51\mu\text{m}$ in diameter. One probe had the films oriented in the vertical plane, angled at $\pm 45^\circ$ to the horizontal ($u-v$) plane. The other probe's films were oriented in the horizontal plane and similarly angled ($u-w$ plane). The transverse separation between the two films was 1mm. During most runs, these probes were traversed about 5cm. Since the traverse was moving slowly relative to the flow, pressure and hot-film measurements were taken while the traverse was in motion. This technique has been validated previously in several experiments in the Mach 3 tunnel.^[26, 69, 74, 75, 94] The hot-film probes were connected to a TSI brand Intelligent Flow Analyzer^[111]. A Tektronix 2454B oscilloscope was used to view and tune the frequency response shape and response time for each film on the probe.

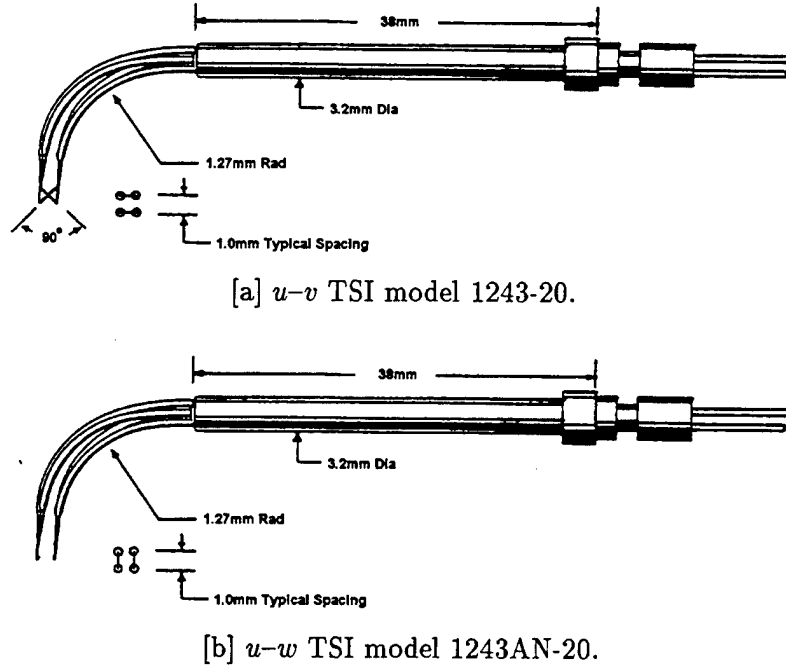


Figure 3.7 Hot film probes.

Cross-film measurements provide a means to resolve the mean mass flux vector into its Cartesian components. When the Mach number normal to the film is greater than 1.2, the Prandtl number may be assumed constant^[57, 98]. When the aspect ratio of the hot-film is also much larger than unity, then the functional form of the Nusselt number may be further simplified. It has been determined experimentally that *King's Law*, the functional relationship between Nusselt number and effective Reynolds number for incompressible flow, is also an acceptable relationship for compressible flow.^[14, 13, 16]

$$Nu = a_k \sqrt{Re_e} + b_k \quad (3.3)$$

The unknowns in Equation 3.3 are the calibration coefficients, a_k and b_k , and Re_e which is the effective cooling Reynolds number normal to the film based on film diameter and reference viscosity. The hot-film calibration is performed by placing the probe in the tunnel free stream, varying the plenum pressure (thus changing Re_e), and measuring the hot-film voltage, providing Nu . The calibration constants a_k and b_k are then determined using a

least squares linear regression on the data. Hence, the calibrated hot-film provides values of local Reynolds number, essentially allowing direct measurement of the mass-flux, $\rho \vec{U}$.

A complication faced by modelers is that the apparent mass terms appearing in the compressible turbulence terms of the RANS equations (Appendix A) cannot be directly measured with conventional methods. One of the key features of cross-wire anemometry is how the Reynolds turbulent shear stress can be directly measured as the negative of the mass-flux correlation term combined with the density fluctuation. Bowersox and Schetz^[16] have shown that these apparent mass terms may be approximated by first noting that

$$\rho\phi = \overline{\rho\phi} + (\rho\phi)' \quad (3.4)$$

and also

$$\rho\phi = (\bar{\rho} + \rho')(\bar{\phi} + \phi') = \bar{\rho}\bar{\phi} + \bar{\rho}\phi' + \rho'\bar{\phi} + \rho'\phi' \quad (3.5)$$

Then, using (3.4) and (3.5) in the Navier-Stokes equations (A.8) and neglecting third order terms allows us to rewrite the Reynolds shear stress (Equation A.11) as

$$\tau_{ij}^T = -\frac{\overline{(\rho u_i)'(\rho u_j)'}}{\bar{\rho}} + \bar{\rho} \bar{u}_i \bar{u}_j \overline{\left(\frac{\rho'}{\bar{\rho}}\right)^2} \quad (3.6)$$

where the second term has been shown to be much less than the first term for thin layer flows. In the present experiments, the second term was always at least an order of magnitude smaller than the first term. The first term may be directly measured with cross-film probes.

Multiple overheat ratios are generally required to determine all of the flow information. However, sensitivity to total temperature fluctuation is often negligible for hot-films operating at high overheat ratios ($\frac{R_{tw}}{R_{ref}} \geq 2.0$). In cases where the fluctuation in total temperature is negligible, only a single overheat ratio is necessary to determine flow field information. Since the AFIT Mach 3 wind tunnel has been found to maintain total temperature fluctuation below about 2.0%.^[44, 45, 70, 75], a single-overheat data reduction method was used. The single-overheat hot-film analysis and its use in the present research is detailed in Appendix B.

3.6 Data Acquisition

The AFIT Mach 3 tunnel is instrumented with a Multipro^[79] data acquisition system. The Multipro has four Model 120 data acquisition boards installed with one megabyte of memory per board. The selection of the sampling frequency was based in part on the criteria of Smits and Muck^[97]. This sampling frequency was selected such that the character of the flow was captured (as indicated by the sampling energy spectra). Experiments were conducted to insure that data were recorded at a sufficiently high frequency. Data acquisition parameters are summarized in Table 3.2.

Table 3.2 Data acquisition system parameters.

Acquisition Parameter	M=2.8 Experiment	M=4.9 Experiment
Pressure Probe Sampling Frequency	200Hz	500Hz
Traverse Speed	.077in/sec	.20in/sec
Hot-film Response Time	8-12 μ s	—
Hot-film Sampling Frequency	16.6kHz	—

3.7 Shadowgraph and Schlieren Optics

The shadowgraph and schlieren images were obtained on Polaroid film using a Xenon^[121] arc light source with a spark duration of 10 nanoseconds. For the shadowgraphs, the light is reflected from a 101.6 cm focal length mirror and photographed with series 52 Polaroid film. The schlieren imaging requires an additional mirror and knife edge to polarize the incoming light to the film. The diagrams for the shadowgraph and schlieren layout are provided in Figures 3.8 and 3.9.

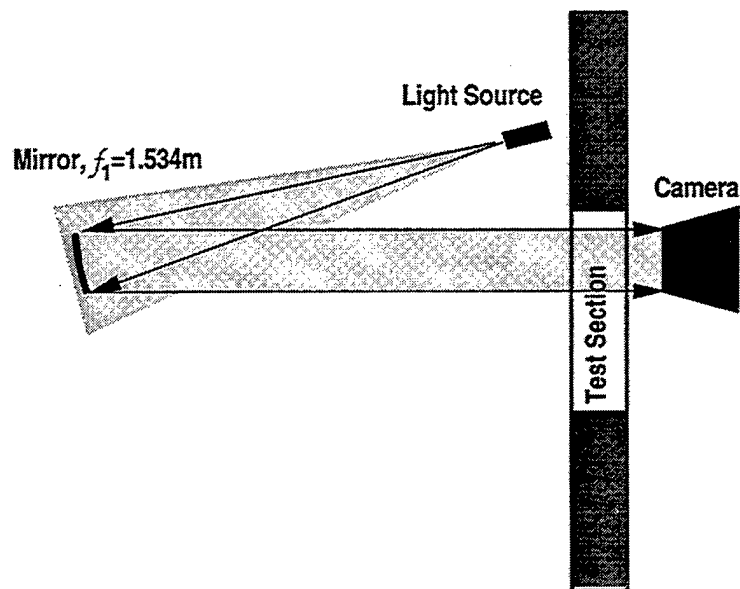


Figure 3.8 Shadowgraph camera and mirror setup.

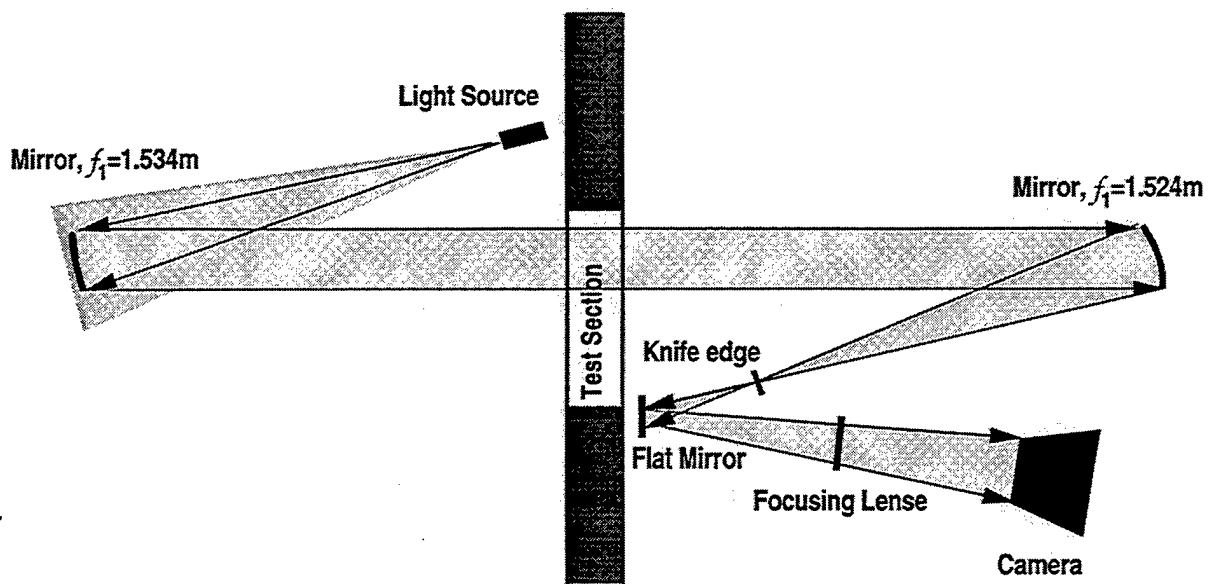


Figure 3.9 Schlieren camera and mirror setup.

4. Numerical Methodology

In this chapter, the numerical methods which have been applied in the present research are presented, along with the associated boundary conditions. Solutions to the governing equations (Appendix A) were obtained using the General Aerodynamic Simulation Program (GASP).^[7, 72] GASP, a fully conservative shock capturing code, has been widely used by the CFD community for the analysis of supersonic and hypersonic flows.^[36, 71, 90, 114] GASP Version 2.0 was used for the inviscid calculations, and GASP Version 3.06 was used for the viscous calculations. A sample GASP 3.0 input deck for the viscous simulation at Mach 2.8 is included in Appendix E.

4.1 Inviscid Calculations ($M=2.9, 5.0$)

As a means of establishing the most suitable locations for experimental measurements, pilot numerical simulations were conducted by solving the Euler equations upstream and in the vicinity of the WAF.^[109] These simulations were conducted on grids representing the WAF model as installed in the Mach 3 and Mach 5 tunnel test sections, and will be discussed further here.

4.1.1 Grid Definition. To resolve the features of the shock structure in the vicinity of the fin, the grid was clustered near the fin and cylinder surfaces. For both Mach numbers, the entire computational mesh consists of 11 computational zones connected via 19 zonal boundaries. Flow variable values are passed through the zonal boundaries via a simple five-point overlap. The entire test section (all four walls) was included in the Mach 2.9 simulation. Since at Mach 5.0 the shock emanating from the body was expected to remain very close to the fin, only two-thirds of the test section was modeled. This simplification provided substantial savings in computational time and memory requirements.

The faces of each zone in the region near the fin were defined with an elliptic grid generator (GRIDGEN^[85]) employing Thomas and Middlecoff^[106] control functions. Grid orthogonality was enforced along the edges of each zone, while constraining the grid points to lie on the geometry surface.^[101, 100] The interior points of each zone were then positioned using a standard trans-finite interpolation (TFI) scheme.^[85] Figure 4.1 shows the numerical

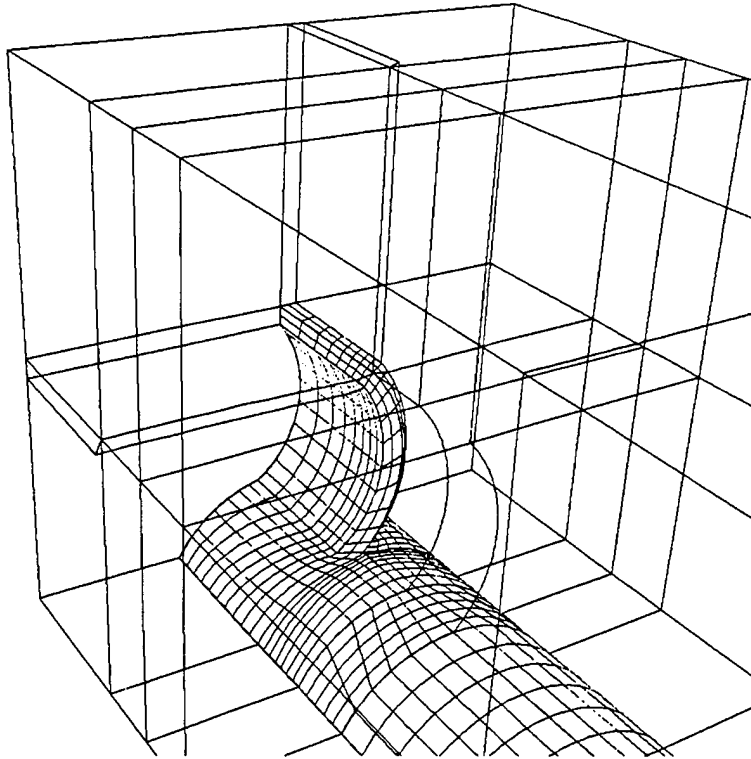


Figure 4.1 Grid boundaries and zonal structure for inviscid Mach 2.9 simulation.

representation of the Mach 3 tunnel test section near the fin. The Mach 5.0 simulation was performed on a grid created by the same methods and defined by the same model geometry. However, the tunnel side walls were moved to represent the wider test section.

4.1.2 Solution Strategy. Since the flow disturbances do not propagate upstream in a fully supersonic flow, the solution was space-marched from an upstream starting plane $0.8r$ ahead of the blended body to a location approximately $0.4c$ ahead of the fin (see Figure 5.1). The location at which the space marching was concluded was chosen to be well ahead of the expected bow shock location. Pilot 2-D simulations over a beveled fin provided early estimates of the position of the shock induced by the fin. These simulations also provided an expedient means to ensure that the grid density and clustering near the fin to be used in the 3-D simulation would be sufficient to capture the key feature of the detached fin shock.

Table 4.1 Freestream conditions used for Euler calculations.

Condition	Value	Value
M	2.9	5.0
P_t	2.0atm	20.4atm
P	0.0633atm	0.03858atm
T_t	294K	375K
T	109.6K	62.5K
U	$607 \frac{\text{m}}{\text{s}}$	$792 \frac{\text{m}}{\text{s}}$
ρ	$0.2039 \frac{\text{kg}}{\text{m}^3}$	$0.2179 \frac{\text{kg}}{\text{m}^3}$

The upstream boundary condition (initial marching condition) was simply prescribed to be the nominal Mach 3 wind tunnel freestream condition^[75] summarized in Table 4.1. The upstream boundary condition for the Mach 5.0 simulation was set at the tunnel freestream design conditions (see Appendix D). Flow tangency was prescribed on all solid surfaces, and was enforced explicitly to first-order accuracy with a full flux method.^[72] For the Mach 5.0 case, flow conditions were extrapolated (first-order) from the interior at the upper boundary of the computational domain (opposite the model). The two-factor approximately-factorized equations were solved at each streamwise marching plane, with relaxation applied in the marching direction. A third order upwind biasing (full flux) scheme was employed in the marching direction, while a second order up-winding scheme with Roe's flux difference splitting was used in the cross-flow plane.

Beginning at a location $0.4c$ ahead of the fin, the three-factor approximately-factorized equations were solved globally to first-order spatial accuracy by employing van Leer splitting of the inviscid fluxes^[112]. The upstream boundary condition for this region is specified to be the solution given at that plane by space-marching. Flow conditions were extrapolated to first-order from the interior at the exit boundary of the computational domain, which is at the trailing edge of the WAF model. Again, flow tangency is enforced on all solid surfaces (including the tunnel walls) explicitly to first-order accuracy with a full flux method. For the Mach 2.9 case, this region is comprised of 8 computational zones, containing a total of 825×10^3 cells. For the Mach 5.0 case, this region is also comprised of 8 computational zones, containing a total of 655×10^3 cells.

4.1.3 Convergence Issues. The inviscid calculations were not intended to be a rigorous computational study. The primary goal of the inviscid study was to obtain a preliminary estimate of acceptable instrument locations for the experimental study. The inviscid computations were assumed to be converged when the residual of the state vector was reduced by three orders of magnitude. At a CFL number of 1.0^[8], this required 838 iterations for the Mach 2.9 calculation and 643 iterations for the Mach 5.0 calculation.

4.1.4 Computational Requirements. The inviscid computations were performed on a Cray C916/161024 supercomputer. The global calculations near the fin required less than 16mWords of memory and 23.5 seconds per iteration to complete. The calculations on the slightly smaller Mach 5.0 grid required 17.5 seconds per iteration.

4.1.5 Inviscid Fin Simulations at Other Mach Numbers. The flow near the fin has also been numerically investigated at several Mach numbers other than 2.9 and 5.0 using the same methods discussed above. For these simulations, the effect of the blending region and tunnel were neglected by imposing the freestream boundary condition shortly upstream of the fin. This assumption minimized computational and solution storage requirements. For this study, the computational grid was identical to the 8-zones near the fin from the inviscid Mach 2.9 study (Figure 4.1).

4.2 Viscous Calculations

The Reynolds-averaged Navier-Stokes (RANS) equations were solved over the model geometry using GASP version 3.06^[7], with the algebraic turbulence model of Baldwin and Lomax^[11].

4.2.1 Grid Definition. The numerical representation of the test article used for the viscous calculations is provided in Figure 4.2. A multi-zone approach was again taken. The entire computational mesh consisted of 12 computational zones (the edges of which are shown in Figure 4.2) connected by 21 zonal boundaries and was comprised of 8.2×10^6 cells. The flow variable values were passed through the zonal boundaries via a simple five-point overlap.

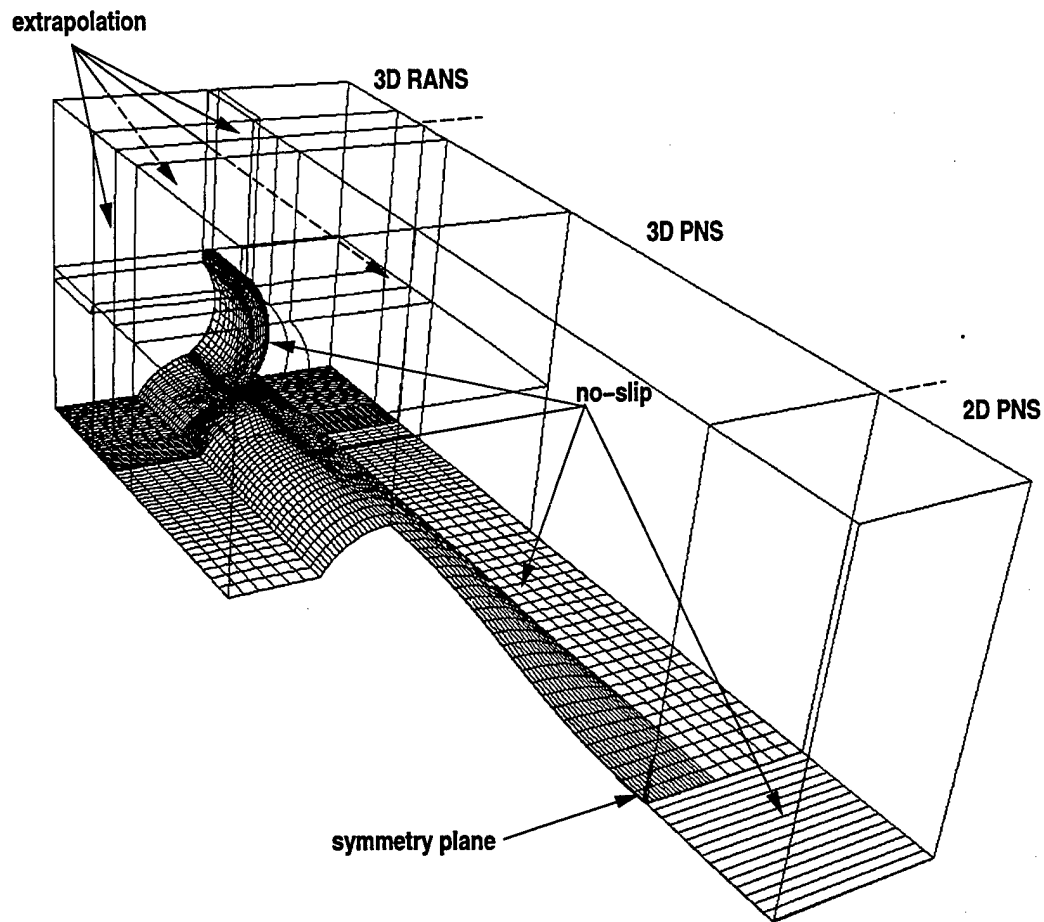


Figure 4.2 Grid boundaries and zonal structure for viscous simulations.

To resolve the features of the flowfield in the vicinity of the fin and to provide the resolution required by turbulence models, the grid was clustered near the fin and cylinder surfaces. At a location $0.4c$ upstream of the fin leading edge the wall grid spacing corresponded to a y^+ value of roughly 0.15 for both Mach numbers investigated. At this location, approximately half of the points in the normal direction were contained in the boundary layer. Zone faces near the fin were defined using an elliptic grid generator (GRIDGEN^[85]) employing Thomas and Middlecoff^[106] control functions. Grid orthogonality was enforced along the edges of each zone, while constraining the grid points to lie on the geometry surface.^[101, 100] The interior points of each zone were then positioned using a standard trans-finite interpolation (TFI) scheme.^[85]

4.2.2 Solution Strategy. For all calculations the thin layer viscous terms (with Sutherland's viscosity model) were included in the governing equations. The algebraic eddy viscosity model of Baldwin and Lomax^[11] was also used to simulate turbulence. Details of this turbulence model are available in A.5. Since flow disturbances do not propagate upstream in a fully supersonic flow, and since experimental results indicated that the blended body produced no separated flow regions, the parabolized Navier-Stokes (PNS) equations were solved to a location $0.5c$ ahead of the fin. This location was deemed sufficiently far upstream of the fin interaction region based on previously conducted visualization experiments.^[45, 109]

To allow for the specification of a two-dimensional upstream boundary condition, the PNS equations were solved on a two-dimensional grid for a short distance ($0.8r$) ahead of the model body. At the inflow boundary, an experimental profile determined using pitot, cone-static, and hot-film probes was prescribed (see Appendix E). Owing to probe volume effects, experimental data could not be obtained sufficiently close to the wall to include the laminar sublayer. However, the two-dimensional PNS region allowed the boundary layer to develop into a fully turbulent profile upstream of the blended body region. The two-dimensionality of the flow in the AFIT Mach 3 wind tunnel has been well documented.^[75, 109] For the simulation of the fin in the Mach 5 wind tunnel, inflow conditions were derived from pitot pressure data. The two-dimensionality of the flow in the AFIT Mach 5 tunnel is documented in Appendix D.

The two-dimensional solution was mapped to the three-dimensional grid at the leading edge of the blended body. As in the inviscid simulations, the two-factor approximately-factorized equations were solved at each marching plane by employing a third order upwind biasing scheme with relaxation in the marching direction and a second order up-winding scheme with Roe's flux difference splitting in the cross-flow plane. The symmetry of the model body was exploited by solving the PNS equations over only half of the blended body region and by employing an x - y symmetry condition at the $z=0$ plane. GASP was modified to allow the solution at the final symmetric marching plane to be reflected across x - y plane. The solution at this plane was then used as the upstream condition for the downstream asymmetric region. In the vicinity of the fin (behind the plane at $0.5c$ ahead of

the fin) the RANS equations were solved to third-order spatial accuracy using Jacobi inner iterations^[7]. The inviscid fluxes were split by the method of van Leer^[112], and the min-mod limiter^[40] was used. This region is comprised of 8 computational zones, containing a total of 4.2×10^6 cells.

On the model surfaces, shown as a mesh in Figure 4.2, a no-slip condition on the velocity, an isothermal wall temperature, and vanishing normal pressure gradient (boundary layer approximation) were enforced.

$$u_i = 0 \quad T = T_{wall} \quad \frac{\partial P}{\partial n} = 0$$

The wall temperature was 294K for the Mach 2.8 simulation. For the Mach 4.9 simulation, the effect of wall temperature was investigated by enforcing relatively cold (294K) and hot (340K) isothermal boundary conditions at the wall. An adiabatic wall condition was also examined. From these simulations, it was determined that the thermal boundary condition at the wall has a negligible influence on the solution. The results presented here were obtained with a 294K isothermal boundary condition, and are indistinguishable from those obtained using the other thermal boundary conditions.

The solid surface boundary conditions were enforced explicitly to second-order accuracy with a full flux method^[7]. Based on the results of the previously conducted experimental and inviscid numerical investigations^[45, 109], it was presumed that the side and opposing tunnel walls had a minimal influence on the flowfield near the fin. Thus, although the size of the computational domain represents the test section, flow conditions were extrapolated (first-order) from the interior at these boundaries. This afforded great computational savings by avoiding the need to enforce a no-slip condition on the opposite and side walls. Also, since the side and opposing tunnel walls were not modeled, the same grid was used for both the Mach 2.8 and Mach 4.9 calculations. The flow conditions were also extrapolated at the downstream plane.

A substantial savings of computational resources was realized through the use of a grid sequencing method. This method reduces the mesh resolution by combining every N computational cell edges into one cell edge in a given direction, where N is the sequencing

level. Therefore the cellular dimension of the finer grid in the sequenced direction must be divisible by N . This coarser grid may again be sequenced if it has suitable dimensions. In the present research, the finest grid was dimensioned such that it could be sequenced twice with $N=2$ in all three grid directions. This simply means that the dimension of every computational block and of every face which defined a geometry had to be evenly divisible by both 2 and 4. Initial iterations were performed on the 'coarse' grid, then that solution interpolated to the 'medium' and the 'fine' grids. This resulted in a huge savings of computational effort, as each iteration on a $N=2$ sequenced grid requires only about one-eighth the CPU time and memory as an iteration on its parent grid. Comparisons between the solution on the sequenced grids were made to investigate grid consistency and convergence issues.

4.2.3 Convergence Issues.

4.2.3.1 *Grid Consistency.* Grid sequencing not only accelerates solution convergence in almost all temporally integrated problems, but it also affords an expedient means to evaluate grid consistency. Grid sequencing was also employed in the upstream region which was evaluated by space-marching the PNS equations ($x \leq -0.5c$) as a means to determine grid consistency. Solutions indicate (Figure 4.3) that the boundary layer predicted on the 'medium' grid on centerline at the exit plane of the space marched region is unchanged by further grid refinement. Data from the fine-grid solution was used to establish the upstream boundary condition for the adjoining region which surrounded the fin.

Although the grid was defined with sufficient resolution at the solid surfaces to employ the algebraic turbulence model on the finest grid, the wall spacing increases with sequencing, possibly leading to erroneous eddy viscosity values. Since the implementation of algebraic closure models in regions having more than one physical length scale (i.e. near two or more solid surfaces) may cause convergence difficulties, convergence studies were conducted by solving the *laminar* form of the RANS equations in the fin region.

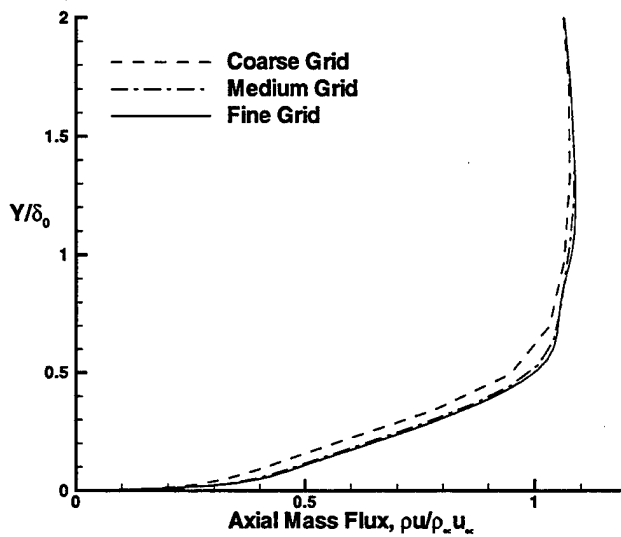


Figure 4.3 Effect of grid refinement on predicted boundary layer profile at the exit of the space-marched region ($z=0, x=-.5c$).

Pitot pressures from converged solutions on each sequence are presented in Figure 4.4 with experimental data obtained at locations aft of the bow shock. The solutions provided by the two finest grids both exhibit the same physical characteristics such as the pitot pressure increase in the boundary layer on the convex side of the fin ($Y/\delta_0 < 0.5$) and a small separation near the body on the concave side of the fin. On the convex side of the fin, the predicted pitot pressures become more similar to the experimental data with grid refinement. On the concave side of the fin, the pressure profiles computed on the two finest grids are very similar, but the extent of the flattening of the pitot pressures near the wall is underpredicted, and the pitot pressure levels in the inner boundary layer are overpredicted. As will be shown in Chapter 5, the extent of the separation region on the concave side of the fin (Figure 4.4[b]) was predicted more accurately with the subsequent addition of an algebraic turbulence model. It will also be shown that there are very large turbulent shear stresses on the concave side of the fin are probably responsible for the overprediction of the momentum levels in the boundary layer.

Examination of the vortical structures ahead of the fin leading edge (Figure 4.5) indicates that the *structure* of the flowfield obtained on the coarsest grid is different than that predicted on the two finer grids. The first grid refinement provides enough resolution

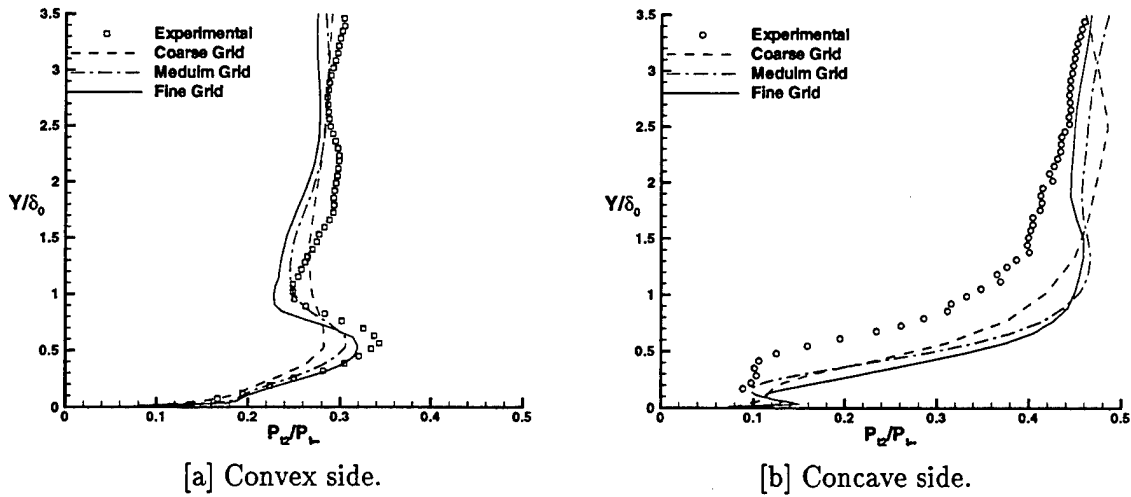


Figure 4.4 Effect of grid refinement on pitot pressure at downstream location.

to predict a 4-vortex structure. Further grid refinement moves the predicted locations of these vortices slightly toward the fin. It is important to note that this region is the most difficult area of the flowfield to resolve, since the flow character is changing drastically over short distances. However, previous numerical studies on blunt fins and cylinders have indicated that it may not be necessary to resolve this region of the flow precisely. This is primarily due to the fact that these particular vortical structures are swept away from the fin, minimizing the effects of their inner composition on the fin loading. Indeed, the agreement can be very good between calculated and experimental quantities away from this region such as surface pressure on the fin and on the body near the fin, even when the number of vortices within the structure is incorrectly predicted.^[37, 88] In the present case, while the pressures gradients ahead of the fin on the model surface are slightly elevated by the last grid refinement, the pressures on the fin surface were virtually identical. Predicted rolling moment coefficients calculated by integrating the surface pressures on the fin sides for the two finest meshes are 0.002077 (medium) and 0.002074 (fine), indicating that grid convergence was achieved in the region of interest. This moment coefficient is about the virtual missile x -axis and based on body diameter and cross-sectional area.

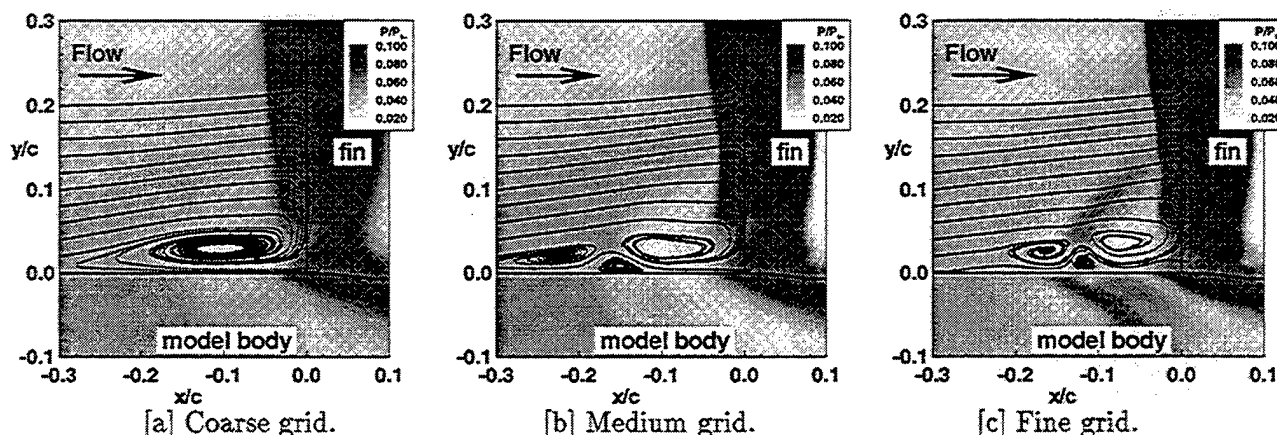


Figure 4.5 Effect of grid resolution on the computed vortical structure ahead of the fin leading edge: $M=2.8$ laminar RANS simulation.

4.2.3.2 Temporal Convergence. For the laminar calculations, the two coarsest sequences were time-integrated until $R_{L_2} < 10^{-4}$, where R_{L_2} is defined as the Euclidean (L_2) norm of the residual vector, and is normalized its value on the first iteration of the current sequence (Figure 4.6). When approaching convergence on the finest grid, the residual vector was dominated by fluctuations in the vicinity of shock waves. This behavior is exhibited in many problems where the flowfield is comprised of regions in which the fluid motion occurs on greatly disparate time scales. In such simulations, convergence must be based on some physical properties of the flow. For the current problem, the pitot pressure on lines corresponding to the experimental data was chosen to determine temporal convergence. The turbulent calculations were performed on the finest grid only with the laminar solution as the initial condition. Temporal convergence was established in the same fashion as it was for the laminar calculation.

4.2.4 Mach 4.9 Calculations. The Mach 4.9 calculation was conducted following the same strategy used for the Mach 2.8 investigation, except that no laminar computations were performed. The Baldwin-Lomax turbulence model was used throughout the simulation, including the solutions on the sequenced grids. The convergence behavior observed during these calculations was very similar to that observed in the laminar computations at Mach 2.8 (Figure 4.7). Changes in the vortical flow structure ahead of the fin due

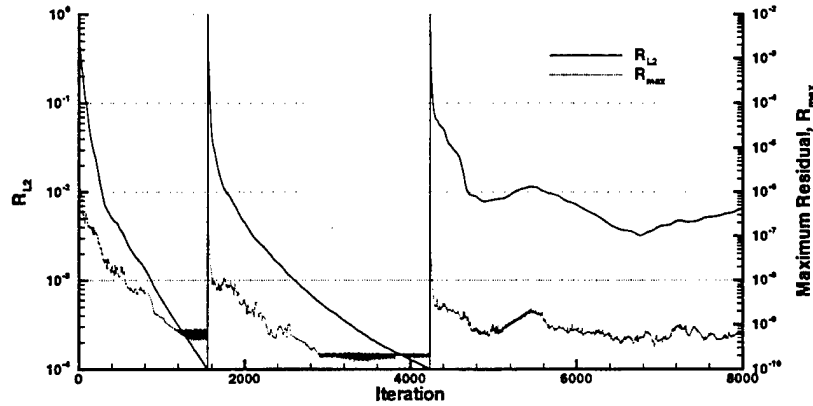


Figure 4.6 Residual history for M=2.8 laminar calculations in global region.

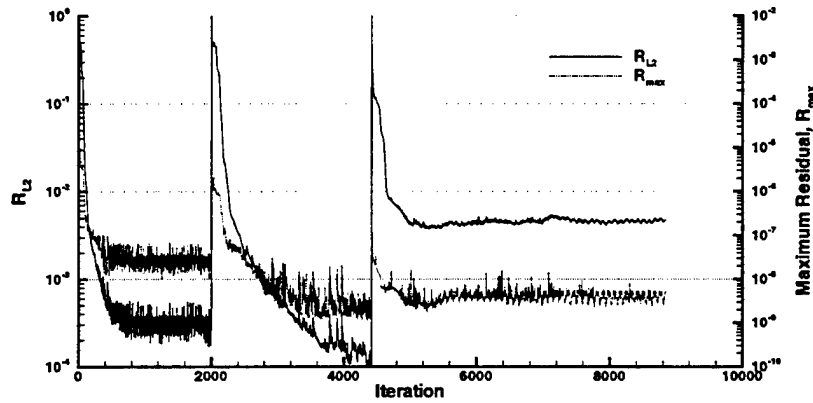


Figure 4.7 Residual history for turbulent M=4.9 calculations in global region.

to grid refinement (Figure 4.8) were also similar to those seen in the laminar Mach 2.8 computations (Figure 4.5).

4.2.5 Computational Requirements. The computational requirements for all of the RANS calculations are provided in Tables 4.2 and 4.3. As expected, the computational requirements, both in terms of memory and CPU, increase by approximately a factor of eight with each grid refinement. The Baldwin-Lomax turbulence model required about 5.5% extra memory, and 34% more time per iteration. All viscous computations were performed on a Cray C916 supercomputer.

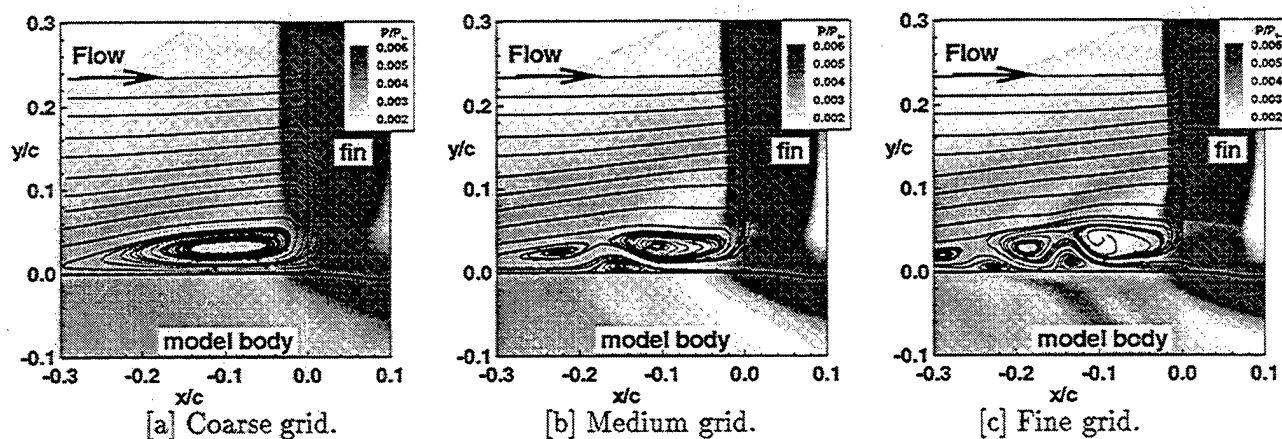


Figure 4.8 Effect of grid resolution on the computed vortical structure ahead of the fin leading edge: $M=4.9$ RANS simulation with Baldwin-Lomax.

Table 4.2 Computational requirements for Mach 2.8 RANS calculations.

Solution Method	Grid Sequence	Number of Cells	Required Memory	Time (sec/itn)
Laminar	3	65168	3.9mW	2.45
Laminar	2	521344	15.3mW	14.5
Laminar	1	4170752	107.mW	97.0
B-L turb	1	4170752	113.mW	134.

Table 4.3 Computational requirements for Mach 4.9 RANS calculations.

Solution Method	Grid Sequence	Number of Cells	Required Memory	Time (sec/itn)
B-L turb	3	65168	4.1mW	3.1
B-L turb	2	521344	16.1mW	19.2
B-L turb	1	4170752	113.mW	133.

5. WAF Flowfield at Mach 2.8

The mean and turbulent structure of the flowfield around a single wrap-around fin mounted on a semi-cylindrical body has been investigated using the experimental and numerical methods outlined in Chapters 3 and 4. In this chapter, the results of the investigations of the WAF at Mach 2.8, including an analysis of the flowfield near the fin, are presented. Experimental and numerical results are used to describe the flowfield around the single-WAF configuration under consideration. The majority of the results at Mach 2.8 have already been published^[45, 108, 109, 110].

First, the results of pilot inviscid calculations and photographic visualization experiments are presented. Then results of the viscous simulation and experimental exploration of the complex flowfield in the vicinity of the fin are then presented, culminating in a discussion of the aerodynamic loading.

5.1 Pilot Inviscid Calculations

The first numerical results in this study were provided by solving the Euler equations over the model geometry in the tunnel's test section (Figure 5.1). These preliminary inviscid results guided the placement of the experimental measurement stations.

5.2 Shadowgraph and Schlieren Photography

To get an initial understanding of the flowfield ahead of the fin, shadowgraph and schlieren images were obtained with the model in the test section. A shadowgraph image of the region near the fin is presented in Figure 5.2. Note how the bow shock remains detached over the full height of the fin at this Mach number. The compression waves induced by the blended forebody of the model can be seen coalescing into a shock and reflecting off of the opposing tunnel wall just above the fin. The bow shock created by the fin is also visible, although the structure at the fin/body intersection is somewhat obscured by the boundary layer on the model body. The boundary layers on the model and opposing wall are also identifiable.

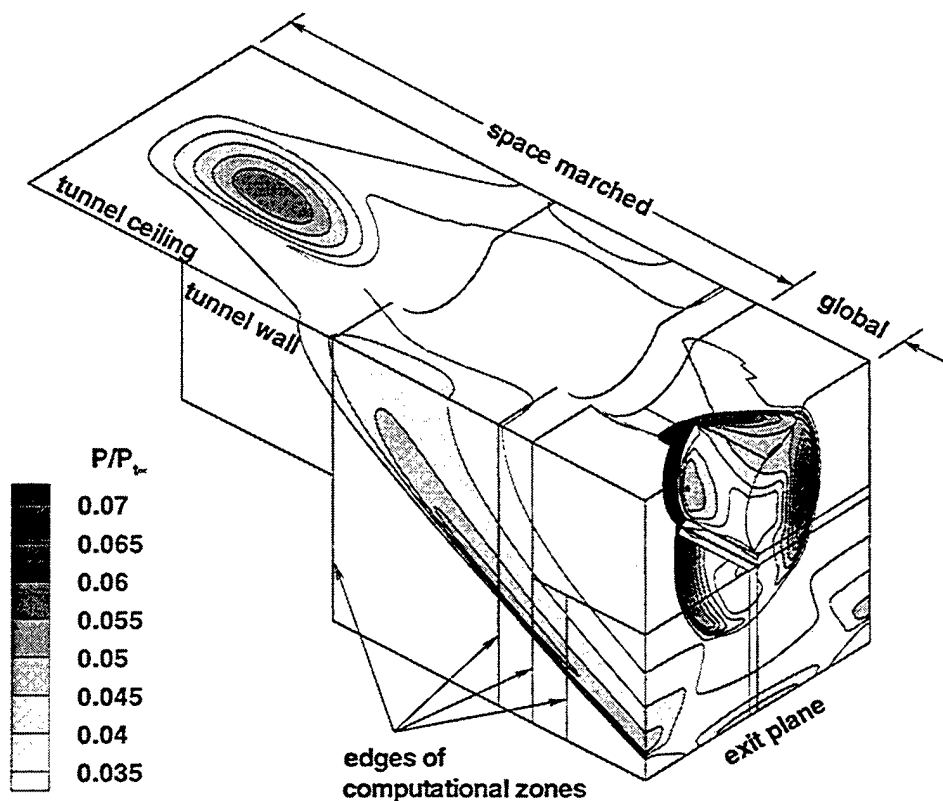


Figure 5.1 Computed inviscid test section surface pressures (at $M=2.9$).

Composite schlieren images of the test section with the model installed are presented in Figures 5.3 and 5.4. These were made with the horizontal knife edge blocking the top and bottom of the light, respectively, thus are theoretically negatives of one another. The turbulent boundary layer on the model is quite visible in Figure 5.3 whereas the shock structure near the fin/body juncture is most easily seen in Figure 5.4. The blending shock is again visible, as is the bow shock created by the fin. The other structures in the images which extend from the floor upward are compression weak compression waves. These disturbances are caused by small imperfections in the tunnel floor associated with the removable plugs which are inserted into the probe access slots and extend across most of the test section. Although these disturbances appear distinctly, subsequent measurements have shown them to be very small compared to the blending shock and the bow shock. Their strength is exaggerated in the photographs primarily due to their two-dimensional nature. In contrast, the bow and blending shocks are three-dimensional structures.

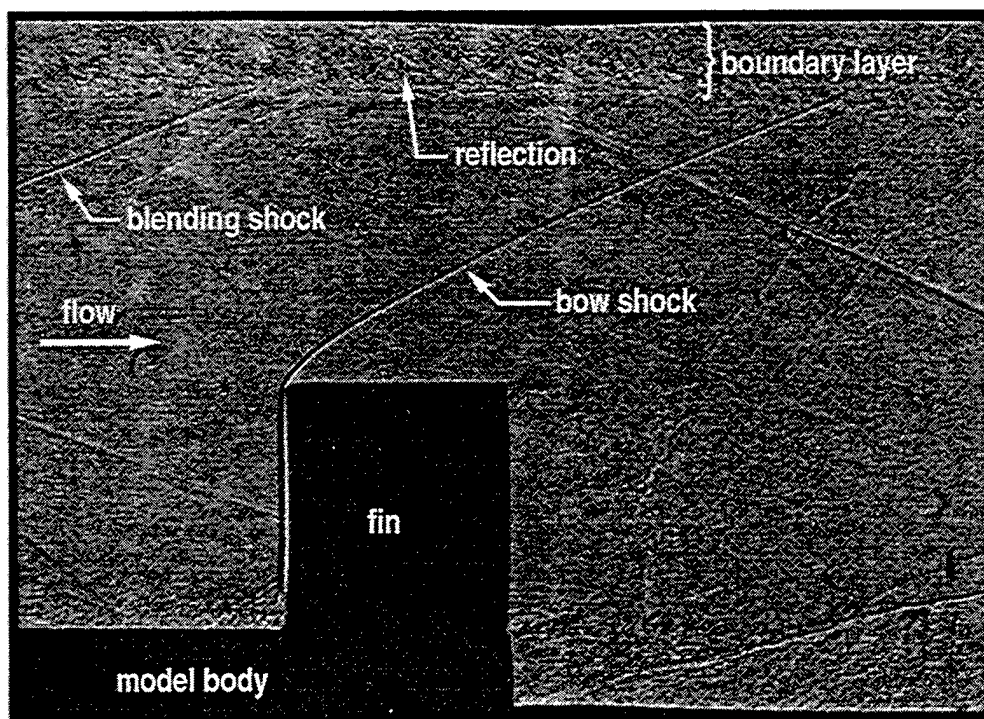


Figure 5.2 Shadowgraph of fin region.

5.3 *Lambda Shock*

Figures 5.5 and 5.6 are images produced by schlieren and shadowgraph photography which have been enlarged to show the detail of the flow structure in front of the base of the fin. The shock-boundary layer interaction produces the same type of λ -shock typically observed in front of blunt fins and cylinders mounted on flat plates in supersonic flowfields.^[29, 39] The λ -shock structure was observed to shift slightly in position from photograph to photograph.

Configurations possessing blunt leading edges have a stagnation point on the leading edge which corresponds to the end of a 'parting line' in the flowfield, indicating the furthest location from the body at which particles become entrained into the vortical flow ahead of the leading edge. The investigated model has a sharp leading edge, making it difficult to identify any stagnation point in the numerical solutions. However, particle traces of the viscous numerical solutions (Figures, 4.5[c], 5.8[e], & 5.9[e]) indicate that the distance from the body at which streamlines diverge as they encounter the fin leading edge is at $y \approx 0.19c$. This agrees quite well with the λ -shock height indicated by photography of $y \approx 0.20c$.

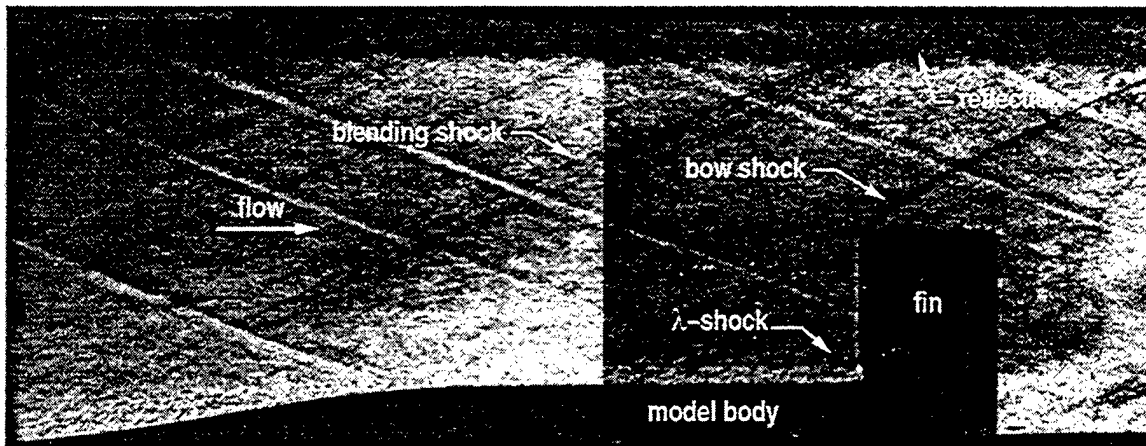


Figure 5.3 Composite schlieren photograph – knife edge on top.

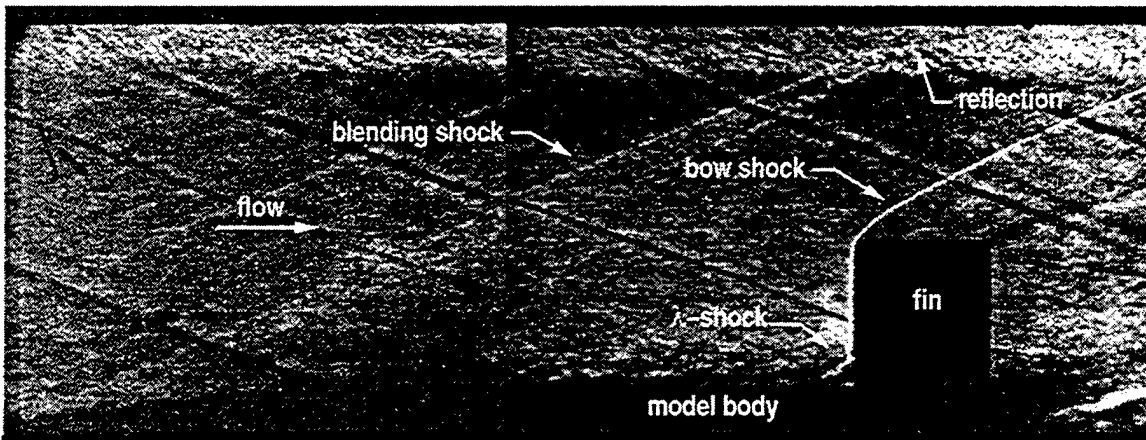


Figure 5.4 Composite schlieren photograph – knife edge on bottom.

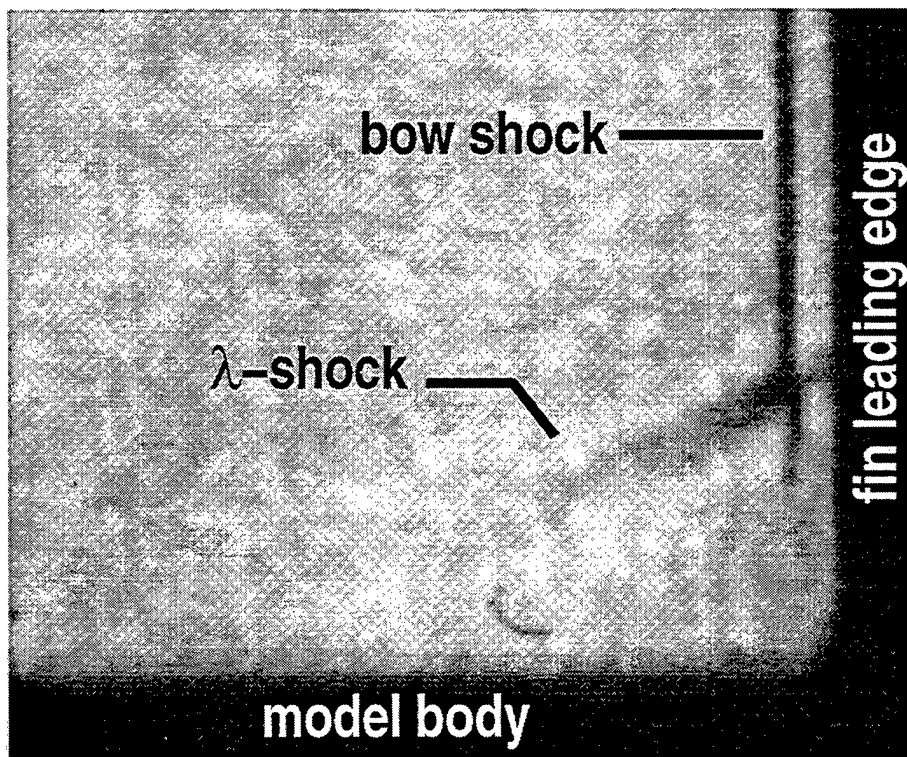


Figure 5.5 Schlieren photograph showing lambda-shock structure.

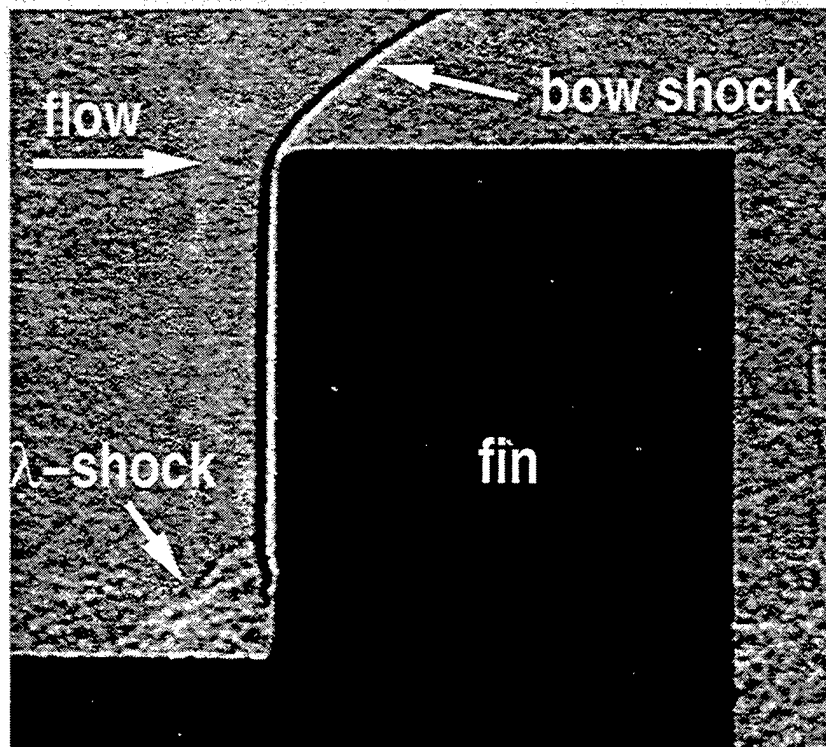


Figure 5.6 Shadowgraph of the lambda-shock region.

5.4 Effect of Fin Curvature on the Flowfield

While 2-D photography indicates flow features similar to those seen on straight fins, conventional pressure probes, hot-film anemometry, and CFD all demonstrate that the flow near the fin is highly asymmetric.^[45, 108, 109, 110]

It is convenient to discuss the flowfield in terms of three regions; an *upstream* region which is ahead of the shock structure, and two *downstream* regions, one on either side of the fin. The present study indicates that each of the *downstream* regions can be further divided into two regions; an *outer* region which is characterized by inviscid behavior, and an *inner* region near the body in which viscous effects are dominant.

The flowfield near the single-WAF geometry has been experimentally explored^[45, 109] by extensively probing the flowfield near the model. In addition to probing the outer flow at several locations near the fin on the ceiling mounted model^[109], measurements were obtained nearer to the fin by mounting the model on the tunnel side-walls. The fuselage boundary layer was also surveyed at four locations on the ceiling mounted model as shown in Figure 5.7.^[45] These locations were chosen to represent the *upstream* and *downstream* regions on either side of the fin, since two of the stations set the reference for the flow upstream of the fin bow shock (at $x=-0.41c$) and the other two stations were positioned downstream of the shock (at $x=+0.69c$). At each of these axial locations, the flow was surveyed on the concave (Cc) side and on the convex (Cv) side of the fin (at $z=\pm 0.47c$) with pressure probes and hot-film cross-wires. Results from the companion numerical study were compared with the experimental data at these locations, and the combined numerical and experimental information were examined for the purpose of characterizing the flowfield. Note that the pressure and hot-film probes flexed slightly ($\approx 2^\circ$) during the experiments under aerodynamic loading. The locations at which the numerical solution was ‘probed’ were canted to mimic this flexing.

In the data presentation, the probe position (x,y,z) is nondimensionalized by the fin chord, $c=20.3\text{mm}$, where the coordinate origin is located at the intersection of the body surface centerline and leading edge of the fin. Negative x values are upstream of the leading edge, and negative z values are to the concave side of the fin. Boundary layer data are

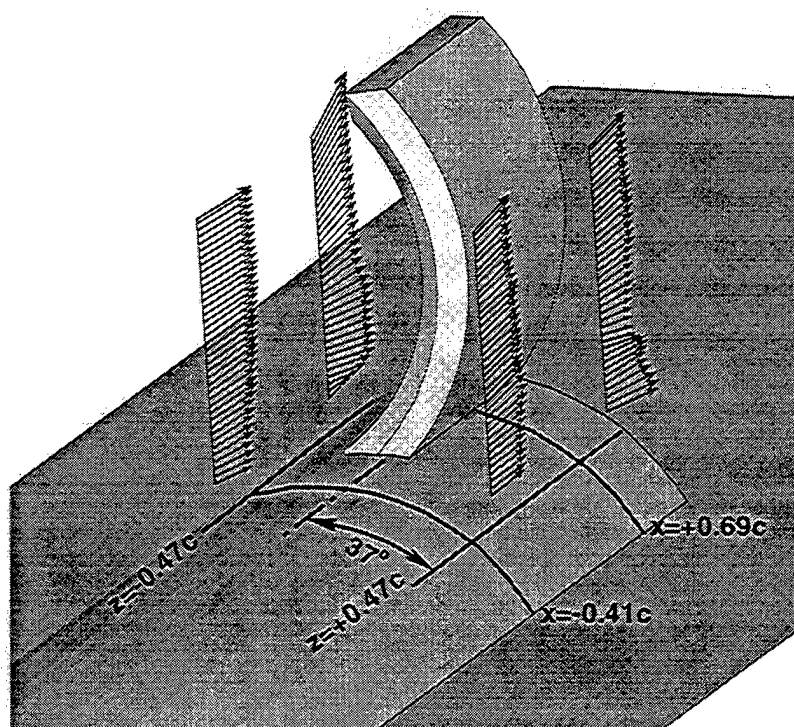
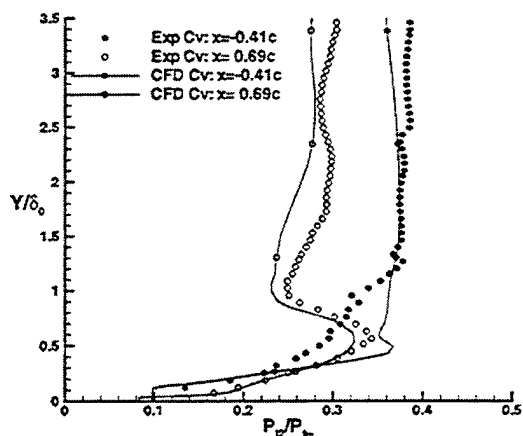


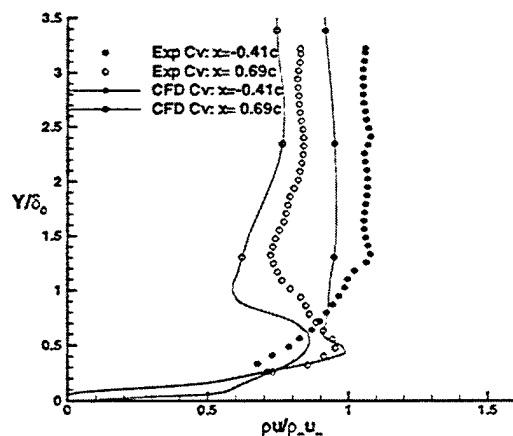
Figure 5.7 Probe locations.

presented as a function of the distance, from the model body, Y . This relative position from the body is normalized by a reference boundary layer thickness, $\delta_0 = 6.1\text{mm}$, which was measured on the model centerline $0.41c$ ahead of the leading edge of the fin.

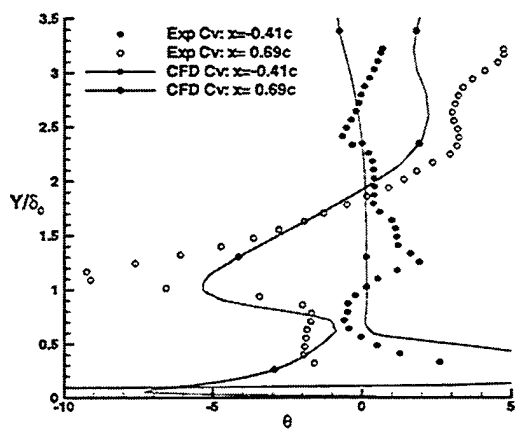
5.4.1 Flow Ahead of the Bow Shock. At the upstream measurement location, both computed and experimental pitot pressures and mass-flux profiles (see Figures 5.8 and 5.9) correspond to those of a largely “undisturbed” boundary layer. While it appears that the numerical solution predicts a thinner boundary layer than measured experimentally, the agreement is good in the outer flow region. The calculations also suggest a high degree of flow symmetry in the outer flow at the upstream measurement locations, while the degree of measured asymmetry was within the experimental uncertainty (Appendix C). At these upstream locations, the numerical results indicate that the flow in the boundary layer is moving slightly away from the centerline (Figures 5.8[d] and 5.9[d]). The flow very near the body is being swept away from the centerline at a very high angle, indicating this part of the boundary layer feels the presence of the fin.



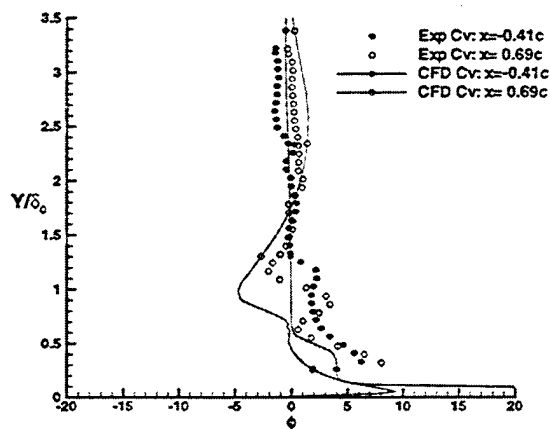
[a] Pitot pressure, $P_{t2}/P_{t\infty}$.



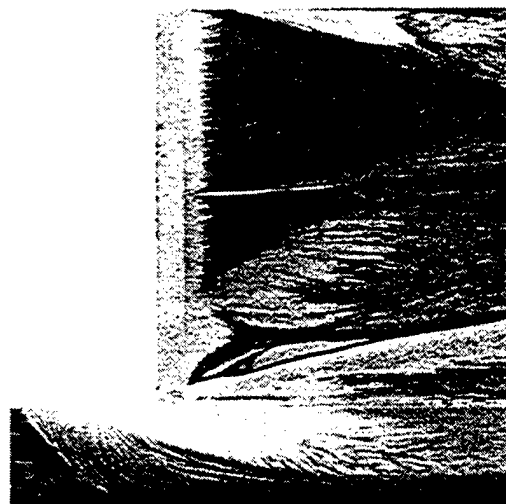
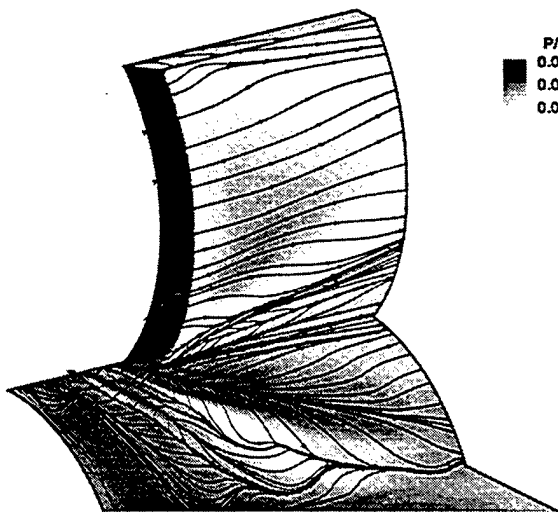
[b] Axial mass-flux, $\rho u/\rho u_{\infty}$.



[c] Horizontal flow angularity, θ (degrees).

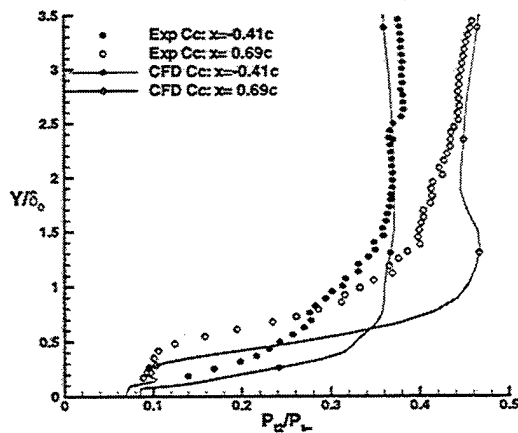


[d] Azimuthal flow angularity, ϕ (degrees).

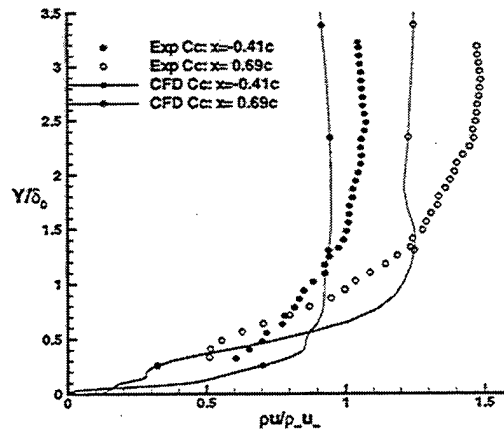


[e] Calculated limiting surface streamlines. [f] Oil flow at Mach=2.06 (Abate and Berner).

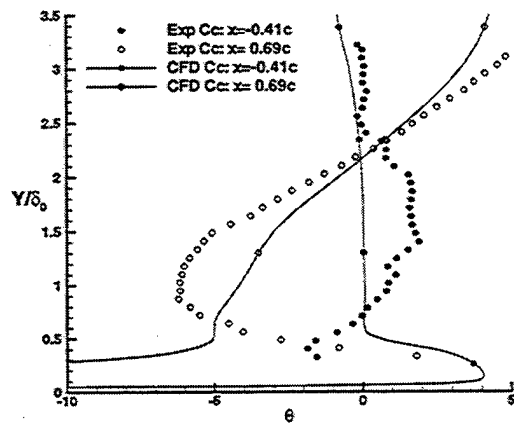
Figure 5.8 Numerical and experimental flow variables; convex side of fin.



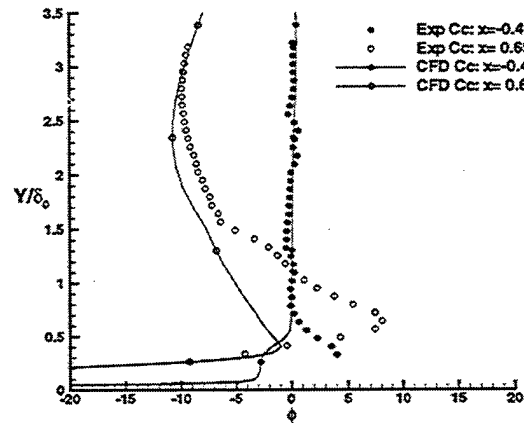
[a] Pitot pressure, $P_{t2}/P_{t\infty}$.



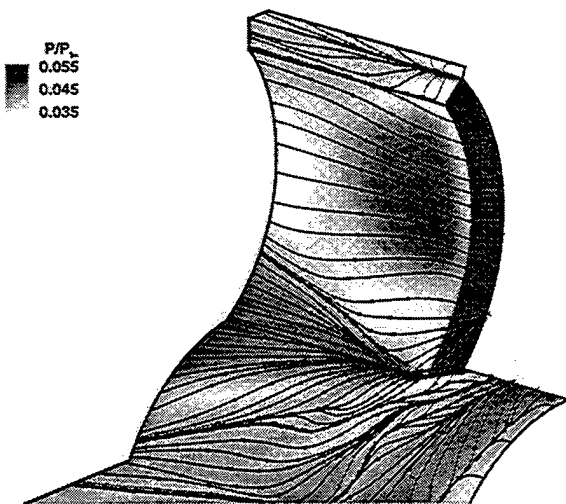
[b] Axial mass-flux, $\rho u/\rho u_{\infty}$.



[c] Horizontal flow angularity, θ (degrees).



[d] Azimuthal flow angularity, ϕ (degrees).



[e] Calculated limiting surface streamlines.



[f] Oil flow at Mach=2.06 (Abate and Berner).

Figure 5.9 Numerical and experimental flow variables; concave side of fin.

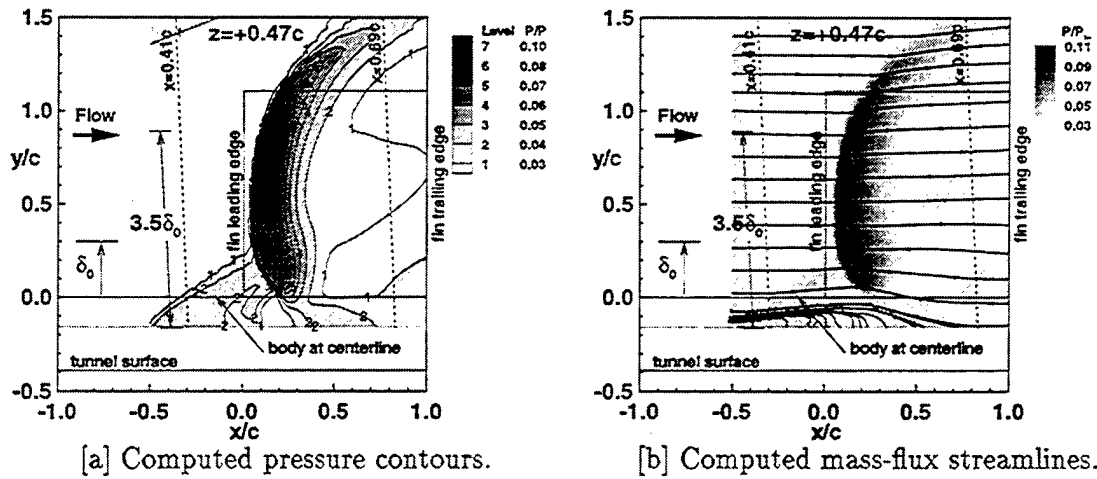
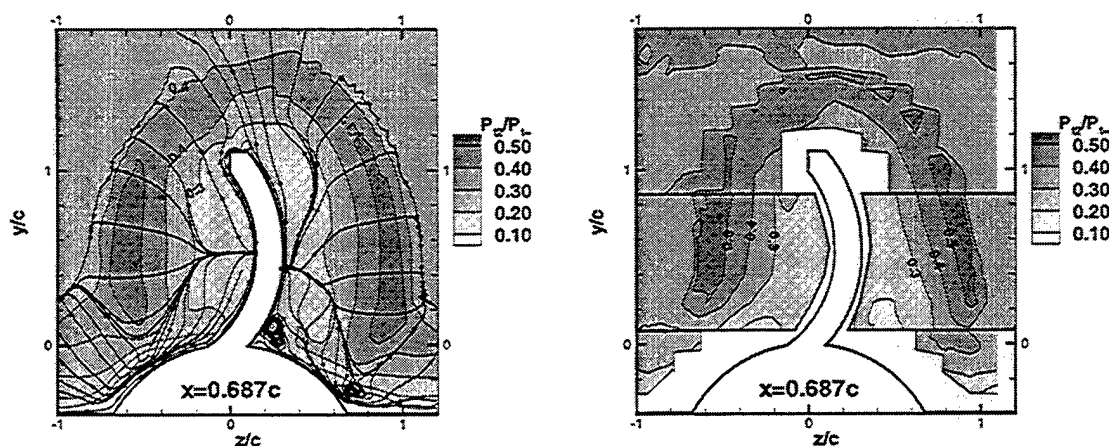


Figure 5.10 Convex measurement plane ($z=+0.47c$) pressure contours and mass-flux streamlines ($\rho u, \rho v$) given by numerical simulation. Outline of fin is overlaid. Dashed lines represent survey locations in the Mach 3 tunnel.

5.4.2 Flow on the Convex Side of the Fin. As the flow nears the fin on the convex side, the outer flow ($Y/\delta_0 > 1.5$) passes through a strong shock (Figure 5.10). This shock induces a strong compression and deceleration. As the fluid passes the fin it is expanded through a large region of favorable pressure gradient between the shock and the downstream measurement location (seen in Figure 5.10) due primarily to the convex fin curvature.

At the downstream survey location, the pitot pressure and mass-flux in the outer flow have been decreased on the convex side relative to the upstream reference plane. This effect has been captured by both inviscid^[109] and viscous numerical results (Figures 5.8[a]&[b]). At this measurement station the outer flow is directed away from the body, but only mildly away from the fin. This behavior is seen in both the experimental data and the computational results (Figures 5.8[a]&[b]).

Profiles of pressure and momentum in the boundary layer at this location are characterized by a large inflection (Figure 5.8[a]&[b]). The flow near $Y/\delta_0 \approx 1.1$ has passed *over* the horseshoe vortex system produced by the shock/boundary-layer interaction ahead of the fin (see Figure 5.10). In this process, the flow greatly expands while only slightly accelerating; the net result is a decrease in the mass-flux. Flow in this region is directed strongly toward the body as indicated by the inflection in the horizontal flow angularity



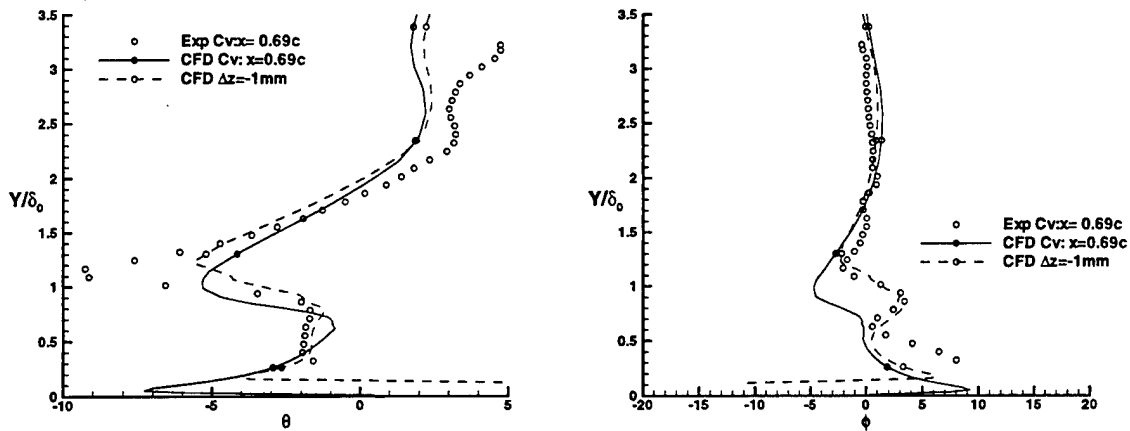
[a] Numerical pitot pressure and streamlines.

[b] Experimental pitot pressure.

Figure 5.11 Flow at $x=0.69c$ measurement plane given by numerical simulation and experiment.

(Figure 5.8[c]). Agreement with experimental data is considered excellent, although the flow turning angle is somewhat underpredicted. Examination of the numerical results indicate that this turning effect is due to a vortex embedded in the fin/fuselage juncture which entrains fluid, pulling it toward the body (seen in Figure 5.11[a]). This vortex creates the pressure minimum seen both numerically and experimentally in Figure 5.8[a]. At roughly the same location, a mild secondary flow component toward the fin ($\phi < 0^\circ$) is observed in the numerical solution; while a corresponding inflection is observed in the experimental results (Figure 5.8[d]). Although the numerical and experimental ϕ profiles are somewhat different, the discrepancies may be attributed to probe volume effects and probe location errors (see Section C.4). Notably, if the location at which the numerical solution is examined is shifted by the probe volume (1mm) closer to the fin, the predicted inflection in ϕ very closely resembles the experimentally obtained data (Figure 5.12[b]). Also, the flattening of the θ profile in the experimental data over the range $0.3 < Y/\delta_0 < 0.8$ is closely duplicated (Figure 5.12[a]). It is notable that the juncture vortex and the associated acceleration toward the body are viscous phenomena and thus have not been captured by inviscid methods.^[109] The significance of this finding is addressed in Section 5.5.

Slightly closer to the body ($Y/\delta_0 \in [0.3, 1.0]$), the flow experiences a compression from above while is at the same time aligned with the x -axis near the body. The net effect is



[a] Horizontal flow angularity, θ (degrees). [b] Azimuthal flow angularity, ϕ (degrees).

Figure 5.12 Effect of $\Delta z = -1\text{mm}$ on flow angularity; convex side of fin.

a sharp increase in mass-flux. Below $Y/\delta_0 \approx 0.3$, wall effects force a decrease in mass-flux and pitot pressure. The flow is directed downward and away from the fin over a very small region ($Y/\delta_0 < 0.2$), following the contour of the body. The numerical results and oil flow patterns at Mach 2.06^[2] (discussed below) suggest that the azimuthal flow angularity, ϕ , at this location tends toward zero at the wall.

Given its proximity to the fin, and hence its effects on the aerodynamic loading, more discussion on the ‘junction’ vortex is warranted. The junction vortex (Figure 5.13) originates near the leading edge of the fin/body junction and remains tucked into the fin/body junction, growing in strength and size as it progresses along the fin. The size and orientation of this vortex is clearly evident in limiting surface streamlines calculated from the numerical solution (Figure 5.8[e]) and in the surface oil flow patterns obtained by Abate and Berner^[2] at Mach 2.06 (Figure 5.8[f]). Surface streamlines starting at the leading edge travel downward along the beveled edge and join with streamlines flowing up from the root to form an accumulation of oil film (or convergence of streamlines) on the surface. This convergence line marks the separation line formed by the junction vortex, and moves away from the junction as it travels toward the trailing edge. The complicated flow structure observed in the oil flow patterns closely resembles that predicted by the numerical solution, suggesting that the flow structure near the junction changes little within this Mach number range. On the body, a weak attachment line (surface streamline

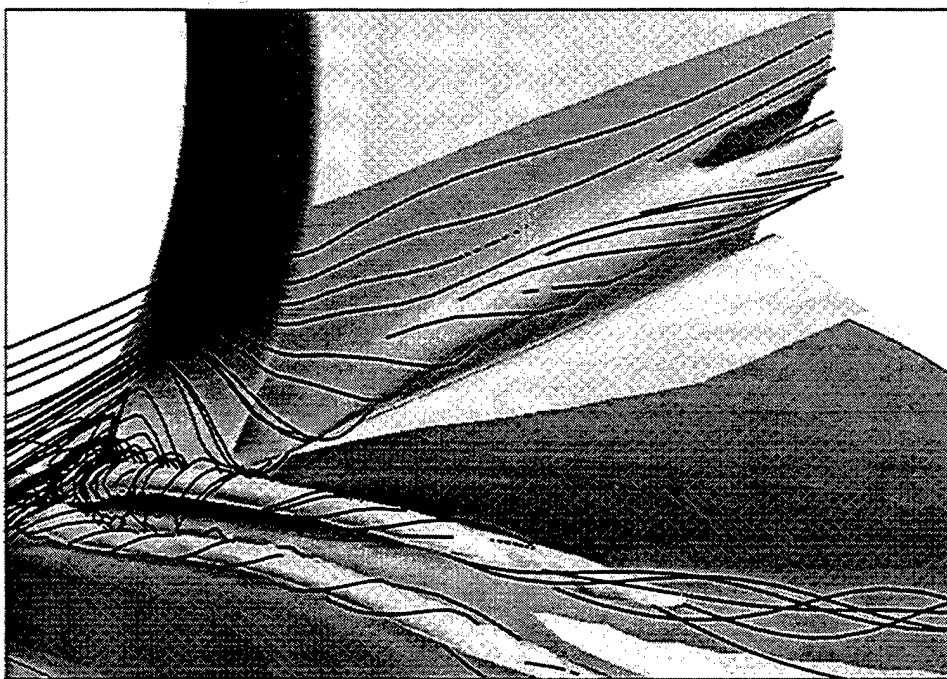


Figure 5.13 Stagnation pressure iso-surfaces and streamlines in juncture vortex region on convex side of the fin.

divergence) moving outward from the leading edge is clearly evident in both the numerical solution (Figure 5.8[e]) and the oil flow (Figure 5.8[f]).

Evidence of such a vortex has also been observed in oil flow patterns on straight blunt fins mounted on flat plates.^[24, 34] Such vortices have been observed to change rotational direction on straight fins depending on incidence angle.^[34] The viscous numerical results indicate that the rotation of the juncture is of the same sense as that seen on the compression side of a straight fin at incidence. Thus, with respect to the juncture vortex, fin curvature and attachment angle can induce similar effects to those produced by cross-flow.

5.4.3 Flow on the Concave Side of the Fin. In contrast to the flow on the convex side of the fin, the flow on the concave side passes through a somewhat weaker shock (Figure 5.14). Thus, the flow undergoes a much more modest deceleration. Also, the post-shock expansion is partially offset by the compressive effects of fin curvature. The net effect is a dramatic increase in the mass-flux (up to 30%) at the downstream measurement

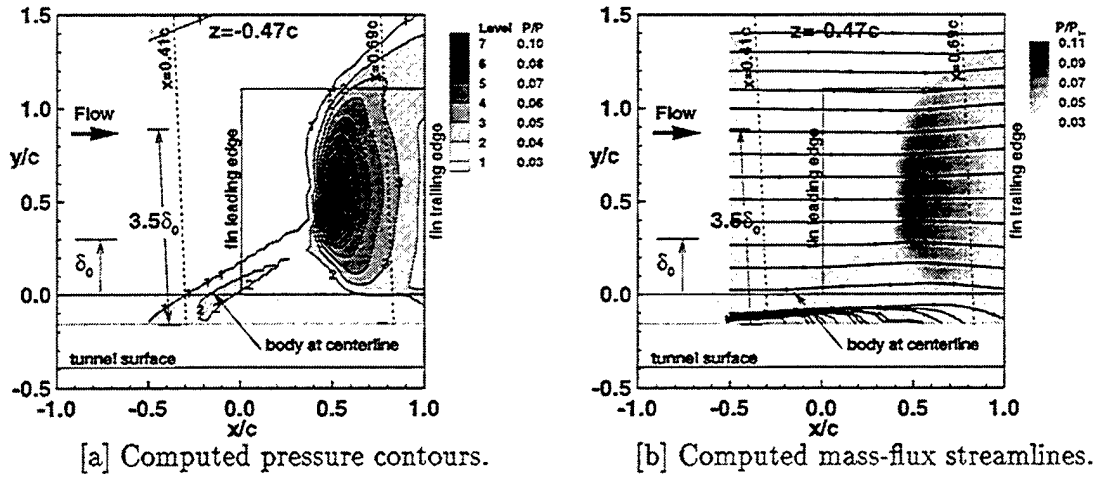


Figure 5.14 Concave measurement plane ($z = -0.47c$) pressure contours and mass-flux streamlines ($\rho u, \rho v$) given by numerical simulation. Outline of fin is overlaid. Dashed lines represent survey locations in the Mach 3 tunnel.

location as compared to the upstream location; This is evident in both the numerical and experimental data. On this side of the fin, the outer flow is strongly directed away from the fin (Figure 5.9[d]) at flow angles, ϕ , up to 10° at the mid-span ($Y/\delta_0 \approx 2.5$). Here, numerical and experimental results indicate that $\theta = 0^\circ$, meaning that the flow is directed toward the center of fin curvature (Figures 5.9[c] and 5.11[a]).

Approaching the body, the fluid momentum decreases (Figure 5.9[a] & [b]). Over a small region inside the boundary layer ($Y/\delta_0 \in [0.5, 1.1]$), the numerical solution suggests that there is a large inflection in the azimuthal angularity (Figure 5.9[d]) where the flow is almost aligned with the vertical plane ($\phi \approx 0^\circ$). This inflection is more pronounced in the experiment data, but occurs at the same location. This effect is likely to be a combination of the flow wrapping around the fin and an expansion which reflects off of the bow shock as a compression. Inviscid numerical results^[45, 109, 110] only faintly hinted at this trend. Over this same range, the experimental data (Figure 5.9[c]) suggest that the magnitude of the horizontal flow angularity is greatly reduced (i.e. $\theta \rightarrow 0$ at $Y/\delta_0 \approx 0.3$). However, this change in flow angularity was not present in the numerical solution at the nominal measurement location. This discrepancy can be attributed to probe volume effects and probe location errors (see Section C.4). Notably, this trend is clearly present in the numerical solution at a probe width (1mm) further from the fin (Figure 5.15[a]).

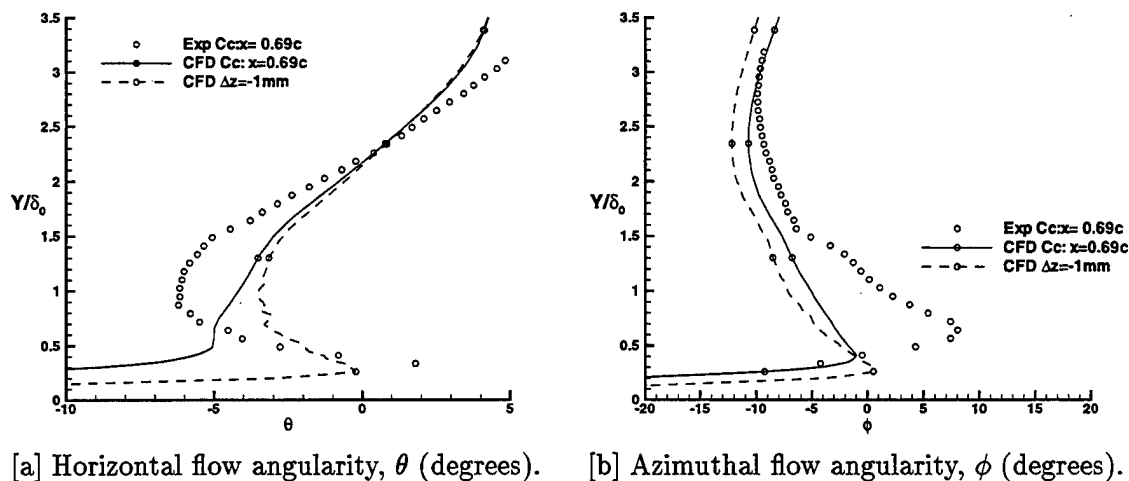


Figure 5.15 Effect of $\Delta z=+1\text{mm}$ on flow angularity; concave side of fin.

Closer to the body ($Y/\delta_0 < 0.5$) there is a small region in which measured and computed pitot pressures do not change. The numerical results suggest that the flow is moving downward and away from the fin ($\theta \approx -30^\circ, \phi \approx -39^\circ$), leading to the flattening of pitot pressure. Cross-wire volume effects precluded experimental examination of this region.^[45]

On this side of the fin, surface streamlines starting at the leading edge also travel downward along the beveled edge and join with streamlines flowing up from the root. However the streamline convergence is 'incomplete' from below, and no juncture vortex is indicated. As on the convex side, the similarities between the predicted surface streamlines and the observed oil flow patterns of Abate and Berner at Mach 2.06^[2] suggest that the flow structure near the juncture on this side of the fin changes little within this Mach number range. The downstream measurement station on this side of the fin is located just behind a separation line on the body, which is seen in the computational results and oil flow pattern. Due to the oblique attachment angle ($\approx 135^\circ$), no juncture vortex was observed on the concave side of the fin in either the numerical or experimental studies, nor is one indicated by the oil flow visualizations^[2] at Mach 2.06 (Figures 5.9[e]&[f]).

In comparing the numerical results to the oil flow patterns of Abate and Berner^[2], it is notable that the latter was obtained on a four-finned missile. Thus the similarity between fin surface streamline patterns suggests that the single-fin model produces the relevant flow features present on configurations with multiple wrap-around fins.

5.5 Aerodynamic Loading on the Fin

The diverse flow topologies on either side of the WAF produce an asymmetric load distribution on the fin surface. While previous inviscid calculations have captured many of the essential flow features, the juncture vortex on the convex side of the fin is dominated by viscous effects and its position and growth near the fin root may provide a significant aerodynamic load, particularly at higher Mach numbers.

The fin surface pressures computed in the inviscid and viscous simulations are shown in Figures 5.16 and 5.17, respectively. On the concave side of the fin, the bow shock is “focused”, producing a high pressure region between the fin and its center of curvature (Figure 5.11) where mass flux levels are increased to 50% over the free-stream value. This produces large region of relatively high surface pressures near the half-span of the fin that contributes to a negative rolling moment (Figures 5.16[b] and 5.17[b]). Here, *rolling moment* will be defined in the vehicle stability sense, thus a negative value indicates a moment acting in the direction of negative curvature. The inviscid calculations predicted that the convex side of the fin also had a region near the fin root over which high pressure levels nearly reach the magnitudes seen on the concave side. This compression had been attributed to the fin being canted in the convex direction ($\approx 45^\circ$) at the fin/body intersection.^[109] However, the viscous numerical results show that this high pressure region is displaced by the boundary layer, and weakened greatly (Figure 5.17[a]). Instead of high pressure, the root region is dominated by low pressures induced by the juncture vortex. Using inviscid numerical methods, Abate and Cook^[3] have shown that the rolling moment is a function of both the fin curvature and fin attachment angle. However, it is now clear that the effect of fin attachment angle is not fully captured by an inviscid analysis. While the Euler analysis predicted a rolling moment coefficient of -0.0102 , the viscous simulation predicted a value of -0.0112 , a 10% increase.

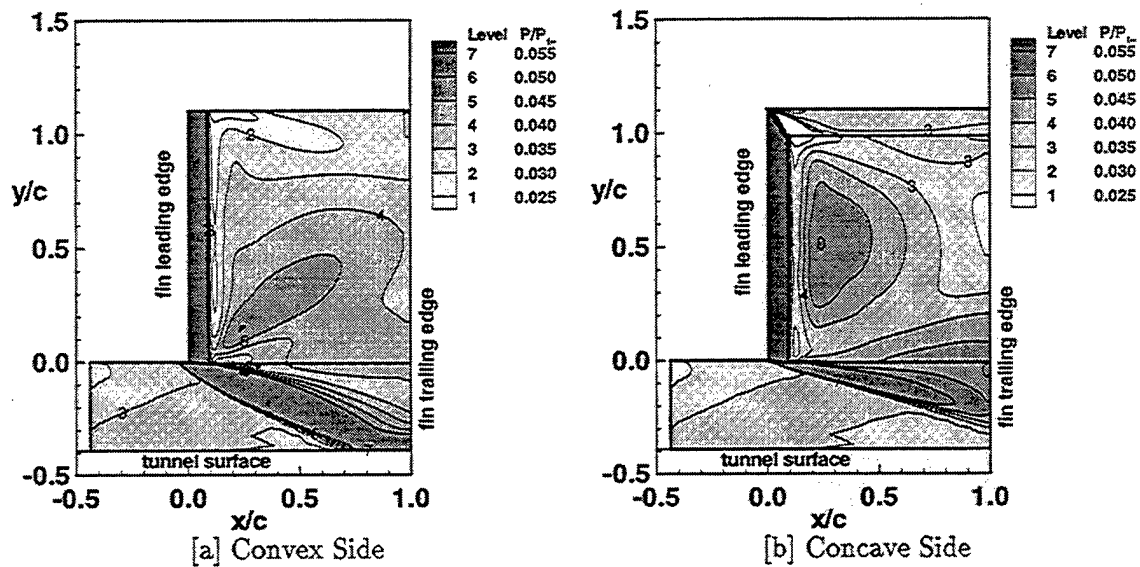


Figure 5.16 Computed inviscid fin surface pressures.

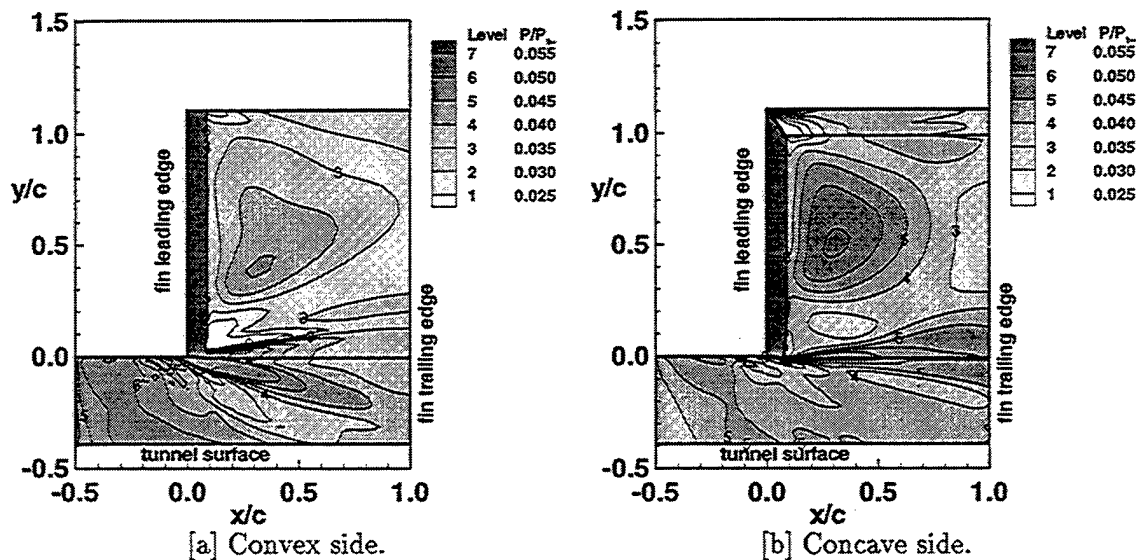


Figure 5.17 Computed viscous turbulent (Baldwin-Lomax) fin surface pressures.

5.6 Effect of the Fin on Fuselage Boundary Layer Turbulence

Turbulence quantities were also measured at the same locations discussed in Section 5.4 (see Figure 5.7).^[45] Although the downstream probe location on the concave side of the fin is in a region of mild favorable pressure gradient, it is also very close to the bow shock. Examination of the turbulence intensity in this region indicates that the shock induces an increase in the axial (Figure 5.18[a]) and transverse (Figures 5.18[b] and 5.18[c]) turbulence intensity, which is consistent with the destabilizing effects of adverse pressure gradients on turbulent boundary layers.^[99]

On the convex side, the turbulence intensities at the same streamwise location are far lower, since the flow has experienced a favorable pressure gradient over an extended streamwise distance (Figure 5.10). Expansions have been reported to *stabilize*, or reduce, the turbulence levels.^[99] Also contributing to this dramatic recovery is the rapid flow acceleration induced by the convex curvature of the fin. Both of the secondary mass-flux turbulence intensities experience a sharp rise near $Y/\delta_0=1.1$, but not so the axial component. The rise in cross-flow turbulence intensity occurs at the same location where the mean flow is being turned sharply toward the body by the juncture vortex.

The net effect of the bow shock and fin curvature are illustrated in Figures 5.19 and 5.20 via the nondimensional turbulent kinetic energy (TKE), K_c , defined by

$$K_c = \frac{1}{2} \left[\overline{\left(\frac{(\rho u)'}{\rho u} \right)^2} + \overline{\left(\frac{(\rho v)'}{\rho u} \right)^2} + \overline{\left(\frac{(\rho w)'}{\rho u} \right)^2} \right]$$

The TKE is significantly elevated on the concave side of the fin and reduced on the convex side relative to values upstream of the shock (Figure 5.19).

Figure 5.20 shows the nondimensional TKE at two streamwise stations; one at the same location as the boundary layer measurements ($x=+0.69c$), and one further upstream at $x=+0.38c$. These surveys, which included the upper portion of the boundary layer, indicate that TKE levels on the convex side are markedly greater than those on the concave side at both stations. Also, TKE is dissipating in the axial direction on both sides of the fin, as the flow passes through regions of favorable pressure gradient. Thus, as the flow

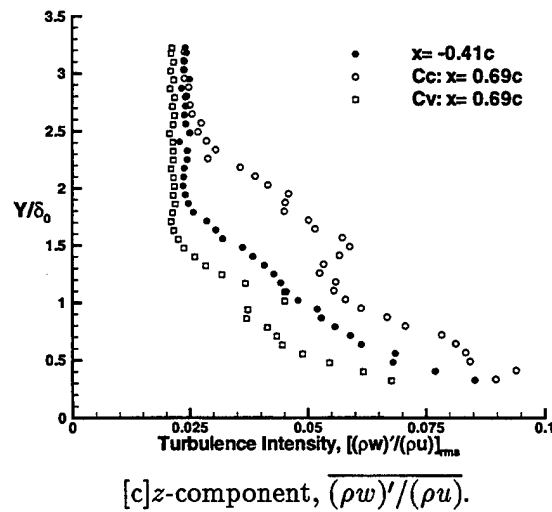
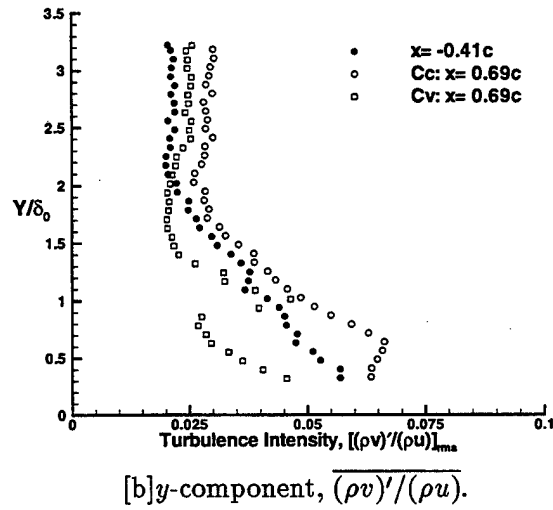
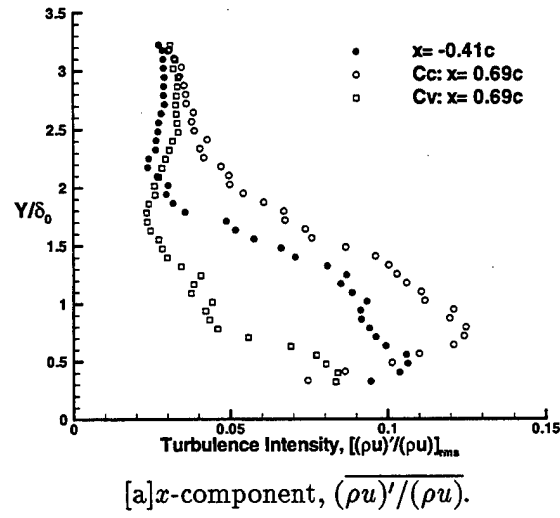


Figure 5.18 Turbulence intensity profiles.

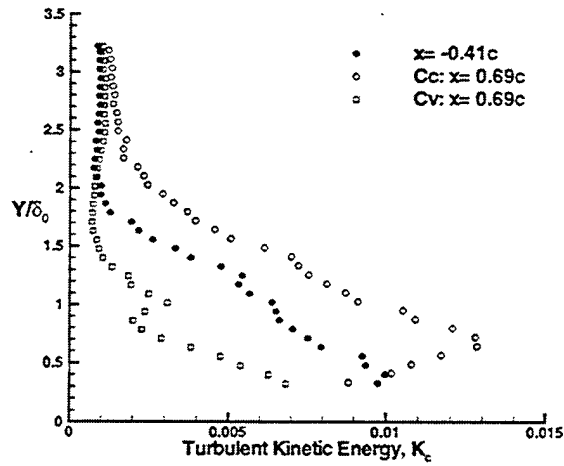


Figure 5.19 Turbulent kinetic energy, K_c .

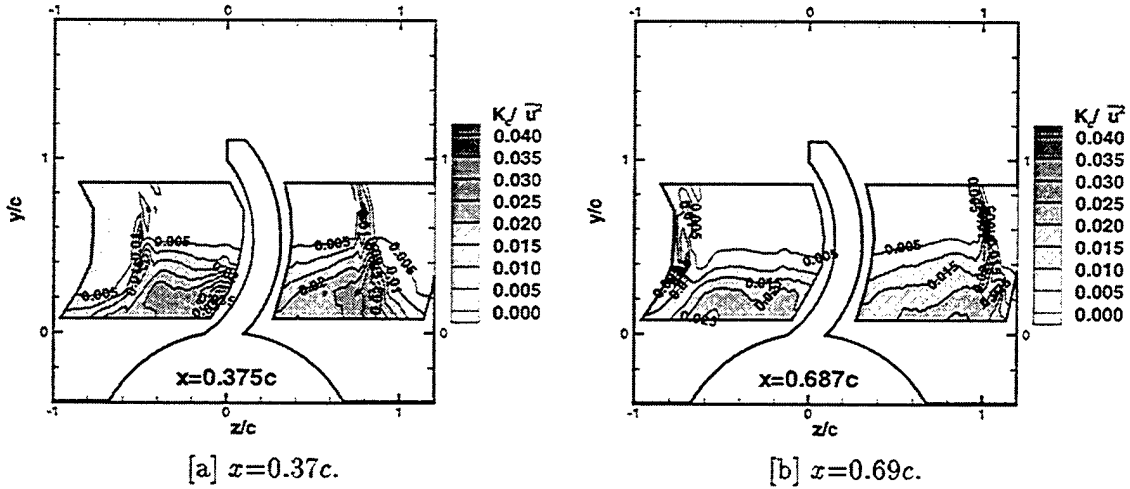


Figure 5.20 Turbulent kinetic energy, K_c .

continues to recover, the TKE levels on the concave side of the fin are likely to continue decreasing in the downstream direction, possibly to the levels seen on the convex side.

The stabilizing and destabilizing effects on turbulence to either side of the fin are also revealed in the Reynolds shear stress estimates measured with the cross-wire (Equation 3.6, Chapter 3) presented in Figure 5.21. Upstream of the fin, the shear stress profile corresponds to that of an undisturbed boundary layer, with levels comparable to those upstream of the model. This indicates that the effects of the compression caused by the blended region of the model have been damped to levels comparable to an equilibrium

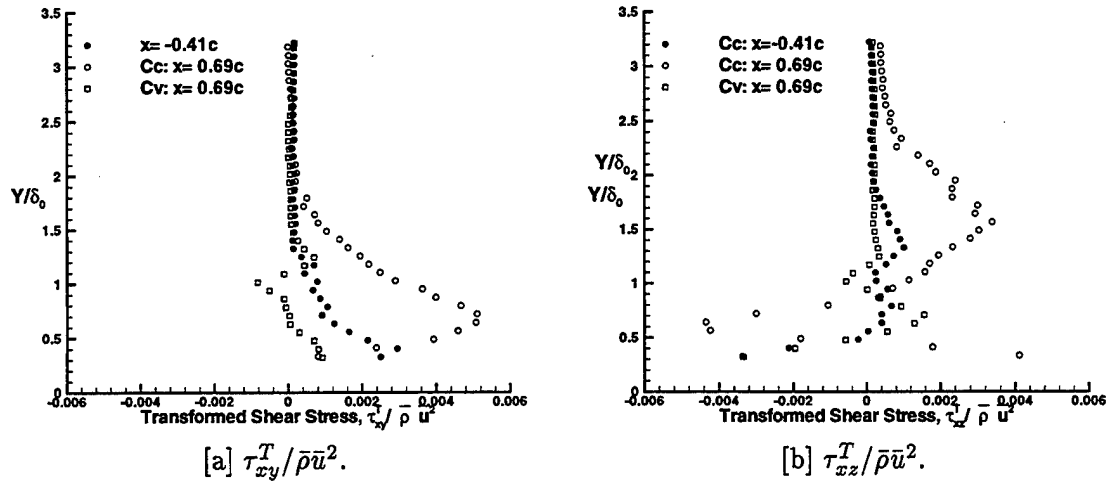


Figure 5.21 Measured turbulent shear stresses, $\tau_{ij}^T = -\frac{(\rho u_i)' (\rho u_j)'}{\bar{\rho}} + \bar{\rho} \bar{u}_i \bar{u}_j \left(\frac{\rho'}{\bar{\rho}} \right)^2$.

turbulent boundary layer. Note that the second term of the total turbulent shear stress in Equation 3.6 has been determined to be at least an order of magnitude smaller than the first term for all surveyed regions, even in those having large flow angularity. Therefore, only the total turbulent shear stress is presented.

On the convex side of the fin, a reduction of turbulent shear stress with downstream position is indicative of the strong stabilizing effect of favorable pressure gradient. Indeed, as observed by other researchers investigating the correlation between streamline distortion and turbulence^[15], the expansion associated with a favorable pressure gradient can result in reduced (or even negative) turbulent shear stress. Conversely, the shear stress on the concave side is increased by roughly 100-200%, commensurate with the previously noted increases in turbulence intensity and turbulent kinetic energy. This pattern is consistent with other measurements obtained in regions of large compression.^[15] Note too that the boundary layer thickness has dramatically increased (by about 60-70%) on the concave side, while it was reduced slightly on the convex side. The large increase in turbulent shear stress on the concave side of the fin may be the primary reason that measured pitot pressure and mass flux levels were less than those predicted by the numerical simulation in the outer boundary layer (Figure 5.9[a]&[b]), since the Baldwin-Lomax turbulence model was not designed to simulate the effects of pressure gradient on turbulence.

6. WAF Flowfield at Mach 4.9

The single-WAF model has also been investigated experimentally and numerically at Mach 4.9 and a unit Reynolds number of $Re/\ell \approx 65-75 \times 10^6 m^{-1}$. These investigations were aimed at determining the structure of the mean flowfield at a high-speed condition.

In the experiment, the mean flow around the ceiling-mounted WAF configuration was surveyed using pitot and cone-static probes and was visualized using shadowgraph and schlieren photography in the AFIT Mach 5 wind tunnel (Appendix D). Fuselage boundary layer surveys were obtained upstream and downstream of the bow shock. The fuselage boundary layer flow was explored near the fin on the ceiling mounted model, as it was in the Mach 3 tunnel. Placement of the measurement stations for the experiment was guided by the inviscid computations (Figure 6.1) and by experience gained from the experiment in the Mach 3 tunnel. The probe locations were the same in the span-wise direction ($z = \pm 0.47c$) as they were in the Mach 2.8 experiment, and the stations that set the reference for the flow were again placed just upstream of the flow interaction at $x = -0.41c$. However, the probes were positioned further aft at the downstream locations ($x = +0.84c$) so as to remain well behind the bow shock.

In the viscous numerical simulation, the Navier-Stokes equations were solved using the same computational grid and numerical strategy used for the Mach 2.8 simulation. The algebraic turbulence model of Baldwin and Lomax^[11] was again employed. Experimental pressure data were used to define the upstream boundary condition for this calculation. The resulting numerical solution is compared with the experimental data and the combined sets of information are examined to characterize the flowfield.

In the presentation of the results, the probe position (x, y, z) is nondimensionalized by the fin chord as it was for the Mach 2.8 results. Boundary layer data are presented as a function of the distance from the model body, Y . This relative position from the body is normalized by a reference boundary layer thickness, $\delta_\infty = 10.2mm$, which was measured on the tunnel centerline $0.8r$ ahead of the blended body. Note that this is larger than the dimension ($\delta_0 = 6.2mm$) by which the Mach 2.8 results were normalized. Although the pressure probes used in the Mach 5 wind tunnel experienced higher loadings than

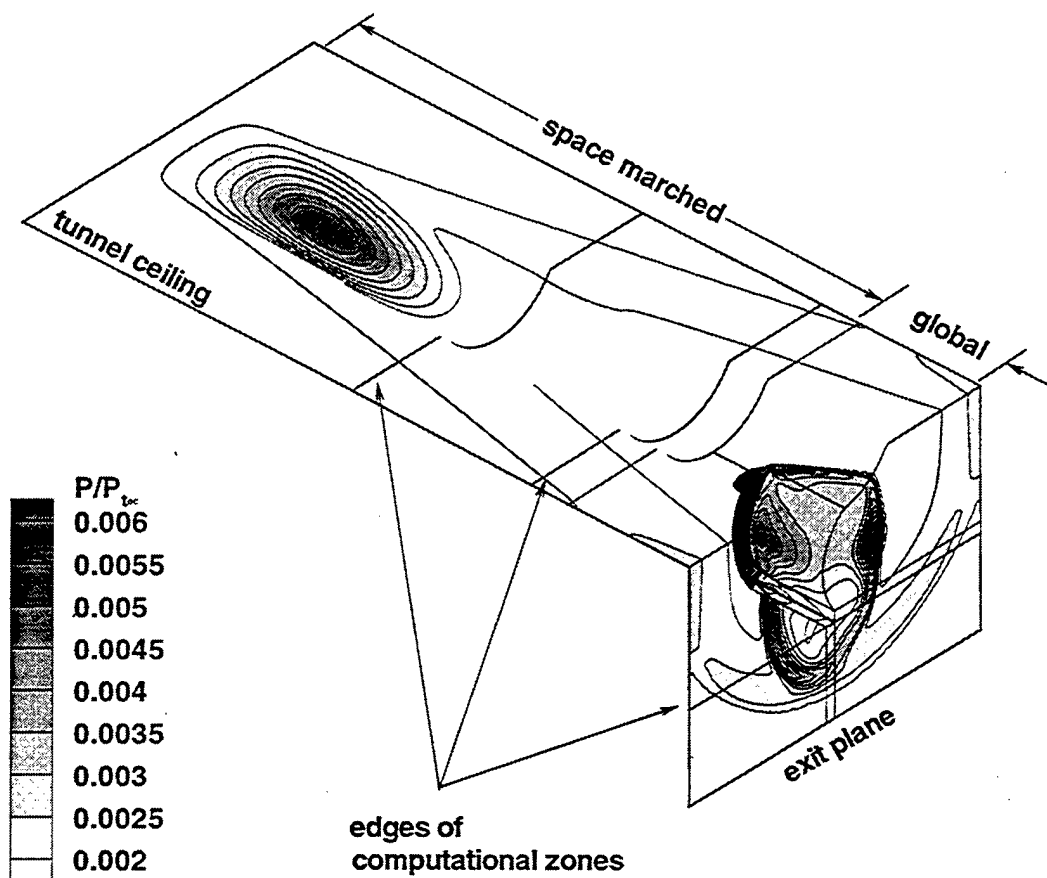


Figure 6.1 Computed inviscid test section surface pressures (at $M=5.0$).

the probes used in the Mach 3 tunnel, they were much stiffer and experienced less flexing ($\approx 1.1^\circ$). The locations at which the numerical solution is compared to experimental results are canted to mimic this flexing.

6.1 Shadowgraph and Schlieren Photography

Shadowgraphs and schlieren images of the fin region (Figures 6.2 and 6.3) again indicate that fin shock remained detached over the full span of the fin as it did at Mach 2.8, although stand-off distance was reduced. The same principal features observed at the lower Mach number were again visible, including the shock caused by the blended forebody and the bow shock, both of which were more highly swept than at Mach 2.8. The λ -shock

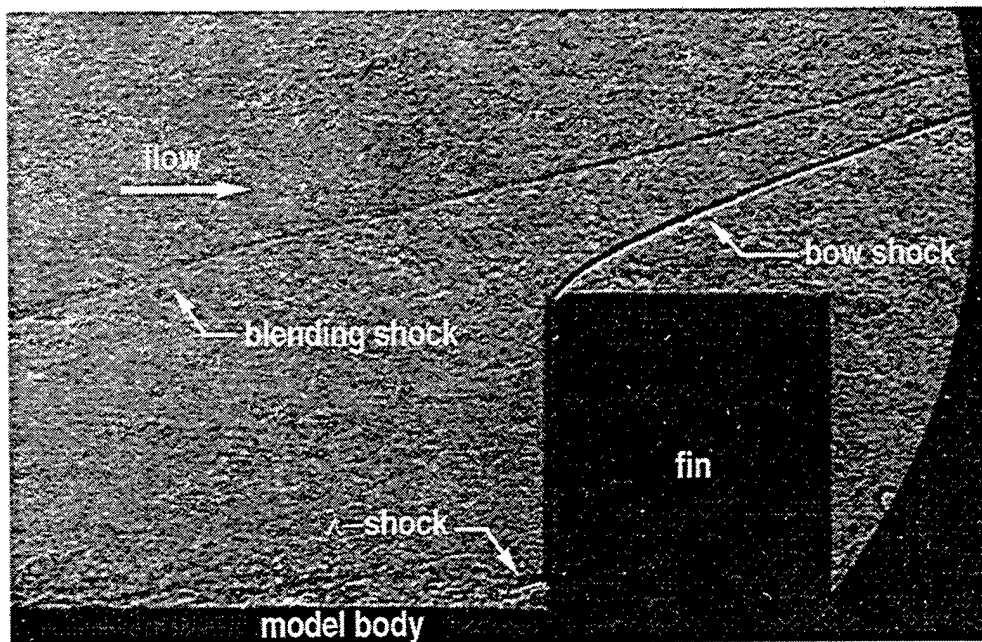


Figure 6.2 Shadowgraph of fin region ($M=4.9$).

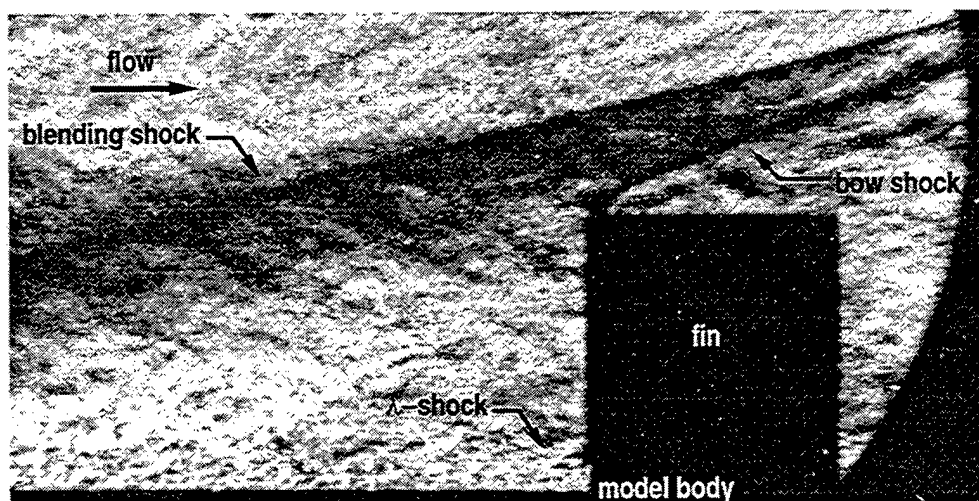


Figure 6.3 Schlieren photograph ($M=4.9$).

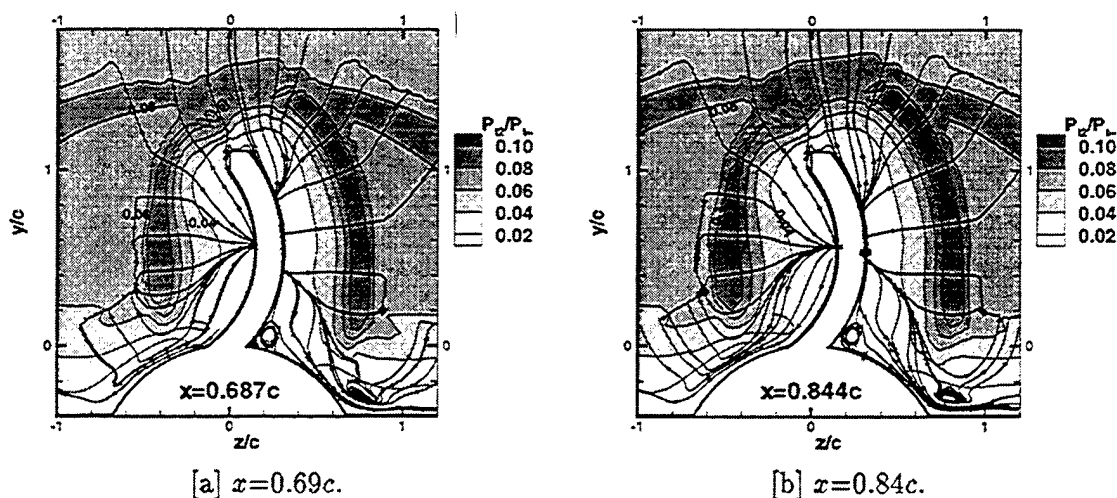


Figure 6.4 Computed pitot pressure and secondary streamlines at $M=2.8$ measurement plane, and at present measurement plane ($x=0.84c$).

was also distinct, though somewhat unsteady, and positioned slightly closer to the body and at a shallower angle than observed in the Mach 2.8 experiment (*cf* Figures 5.2 and 6.2). This trend was also captured in the viscous numerical solutions (*cf* Figures 4.5 and 4.8).

6.2 Effect of Fin Curvature on the Mean Flowfield

The experimental and numerical results suggest that the flow near the fin is highly asymmetric as it was at Mach 2.8. In fact, most of the qualitative discussion on the flowfield structure at Mach 2.8 (Chapter 5) applies at Mach 4.9 as well. As expected, the fin's domain of influence in the outer flow was reduced from that at Mach 2.8 (Figure 6.4).

The measured flow asymmetry at the upstream measurement plane was minimal (Figure 6.5), and well within the experimental uncertainty (especially considering that the data were acquired on different days). At this upstream location, there is a much larger pressure gradient in the direction away from the body than was observed at Mach 2.8 due to the relative proximity of the blending shock.

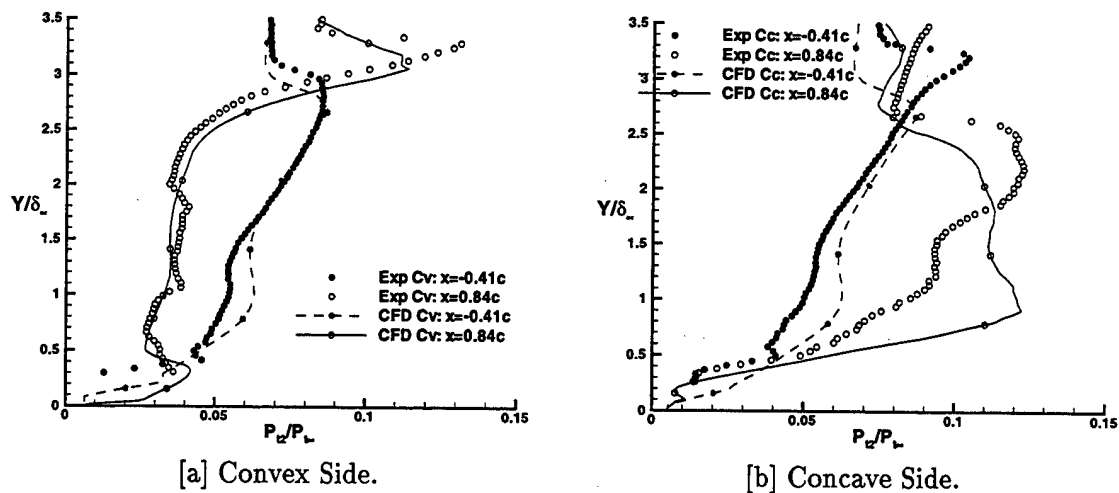


Figure 6.5 Experimental and numerical pitot pressure.

6.2.1 Flow on the Convex Side of the Fin. As seen at Mach 2.8, the flow on the convex side of the fin passes through a strong shock (Figure 6.6[a]), and then expands through a large region of favorable pressure gradient between the shock and the downstream measurement location due to the convex fin curvature. Relative to its upstream value, the pitot pressure in the outer flow at the downstream measurement station has been decreased by about 40% (Figure 6.5[a]). Agreement between experimental and computed pitot pressures is considered excellent on this side of the fin.

The calculated pitot pressure profile features a large inflection in the inner region (Figure 6.5[a]). This inflection is more difficult to identify in the experimental results than it was at Mach 2.8. While the larger volume of the pitot probe used at Mach 5 precluded a definitive assessment of this feature, it appears that the inflection may be closer to the body and not as large as that predicted by the numerical simulation. The computed pressure peak is at approximately the same physical distance from the wall at both Mach numbers ($0.3\delta_\infty \approx 0.5\delta_0$).

Recall from the Mach 2.8 discussion that this inflection in pitot pressure was associated with the existence of a juncture vortex. This vortex is also present in the solution at Mach 4.9 (Figure 6.7), and is probably present in the experimental flowfield, although the pressure data do not provide conclusive evidence. The predicted rotational direction at Mach 4.9 is the same as it was at Mach 2.8, but the predicted location of the junc-

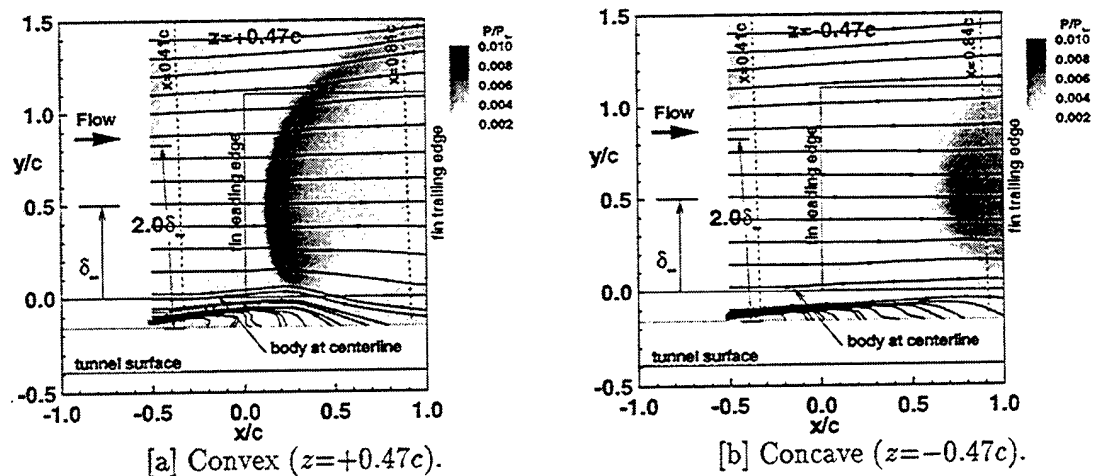


Figure 6.6 Computed pressure and mass-flux streamlines ($\rho u, \rho v$) on measurement planes ($M=4.9$). Outline of fin is overlaid. Dashed lines represent survey locations.

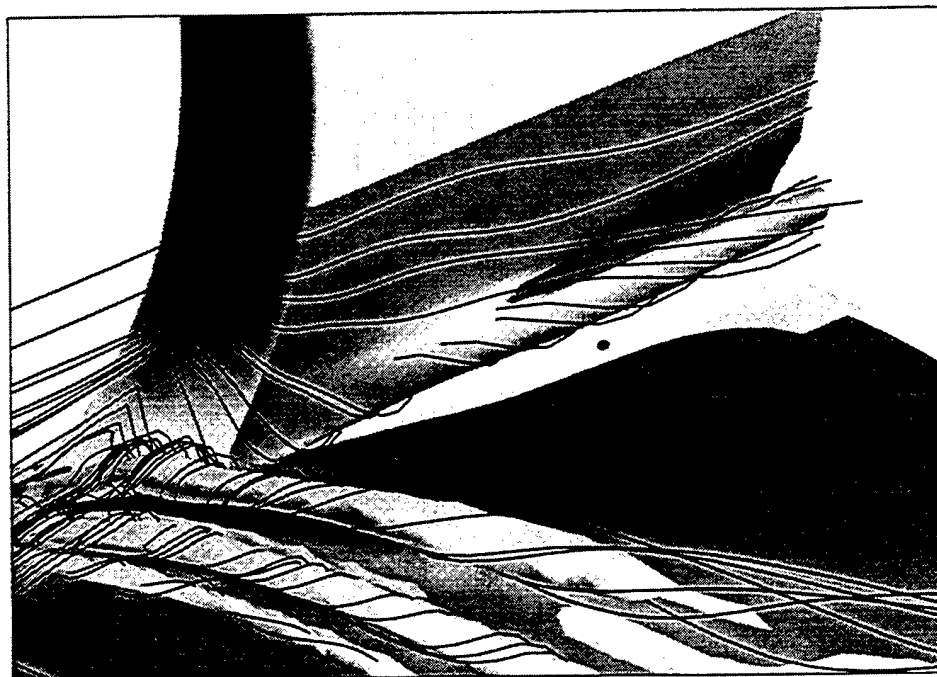


Figure 6.7 Stagnation pressure iso-surfaces and streamlines in juncture vortex region on convex side of the fin.

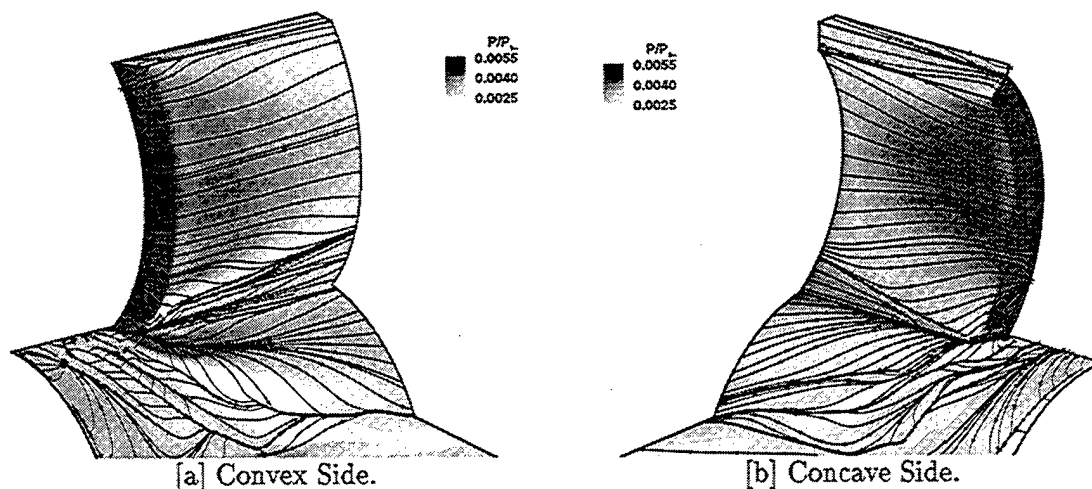


Figure 6.8 Computed limiting surface streamlines at $M=4.9$.

ture vortex is slightly closer to the fuselage (*cf* Figures 5.11[a] and 6.4[a]). The size and orientation of this vortex is also indicated by the calculated limiting surface streamlines (Figure 6.8[a]). While the structure of the surface streamlines on the fin are very similar to those calculated at Mach 2.8, the separation line formed by the juncture vortex is slightly closer to the body. Also, the weak attachment line on the body moving outward from the leading edge is slightly closer to the fin than predicted at Mach 2.8.

6.2.2 Flow on the Concave Side of the Fin. As was the case at Mach 2.8, the outer flow ($Y/\delta_\infty > 1.0$) on the concave-side measurement plane passes through a somewhat weaker shock than on the convex side (Figure 6.6[b]). Again, the post-shock expansion is partially offset by the compressive effects of fin curvature. The net effect is a very large increase in the pitot pressure (up to 90%) and momentum by the time the flow reaches the downstream measurement location. This increase is observed in both the numerical and experimental data (Figure 6.5[b]), and is even more dramatic than at Mach 2.8. The overprediction of the pitot pressure in the outer boundary layer on this side of the fin is probably again the result of the lack of pressure gradient effects in the turbulence model.

Close to the body ($Y/\delta_\infty < 0.4$) there is a small region over which measured and numerical pitot pressures do not change. The viscous simulations suggest that the flow in this region is moving down and away from the fin at angles comparable to those predicted

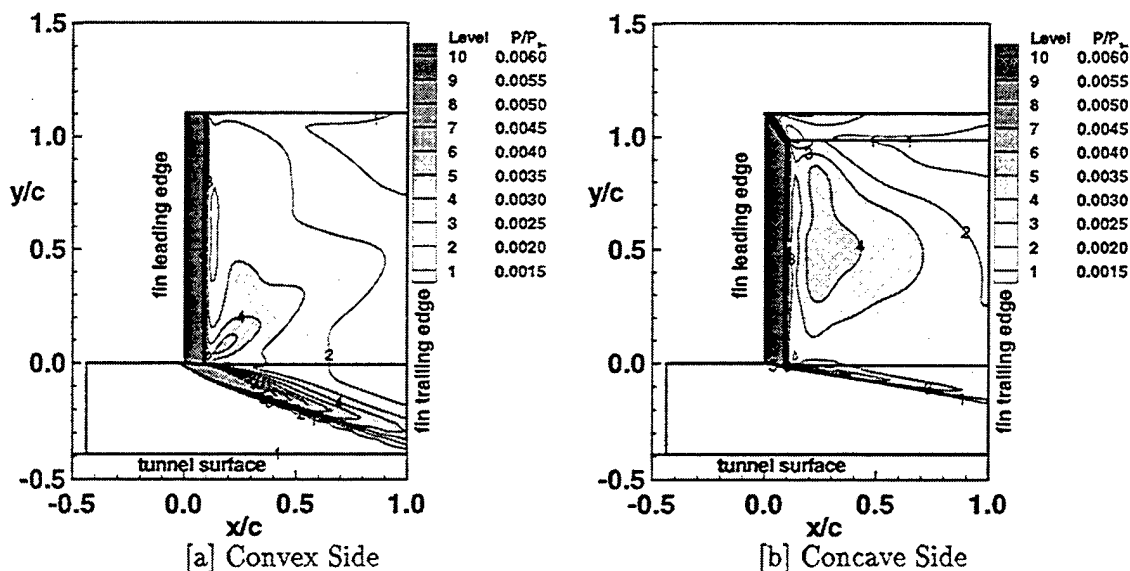


Figure 6.9 Computed inviscid fin surface pressures.

at Mach 2.8, leading again to a ‘flattening’ of pitot pressure. The similarities between the calculated flowfields the two Mach numbers ($M=2.8, 4.9$), as well as the similarity of calculated surface streamline patterns to the oil flow patterns of Abate and Berner at Mach 2.06^[2], suggest that the flow structure on the concave side of the fin changes little with Mach number. The exception is the trajectory of the incomplete surface streamline convergence on the fin, which becomes more obtuse with decreasing Mach number. The downstream measurement station on this side of the fin is again located just behind a separation line on the body which is at approximately the same location as it was at Mach 2.8. On this side of the fin, the calculated secondary flow structure is also very similar to that predicted at Mach 2.8 (*cf* Figure 6.4[a] and 5.11[a]). The outer flow is strongly directed away from the fin toward the center of fin curvature at the mid-span, and again, no juncture vortex is observed on this side of the fin.

6.3 Aerodynamic Loading on the Fin

As was true at Mach 2.8, diverse flow topology on either side of the WAF produce a dramatically different load distributions on the opposing fin surfaces. The fin surface pressures predicted by the inviscid and viscous simulations are shown in Figures 6.9 and 6.10, respectively. The computed rolling moment from this simulation at Mach 4.9 is about

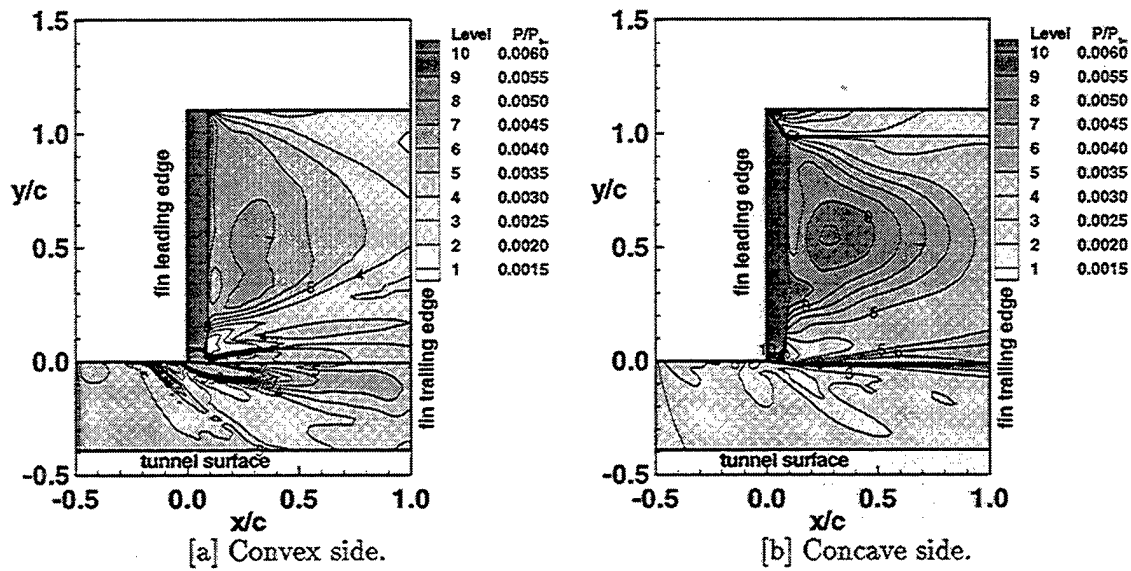


Figure 6.10 Computed viscous turbulent (Baldwin-Lomax) fin surface pressures.

one-third of that predicted at Mach 2.8, and is about 60% of that predicted by inviscid simulation. As shown in Figure 6.11, the viscous simulations suggest that Mach number has a stronger influence on rolling moment that inviscid simulations would imply.

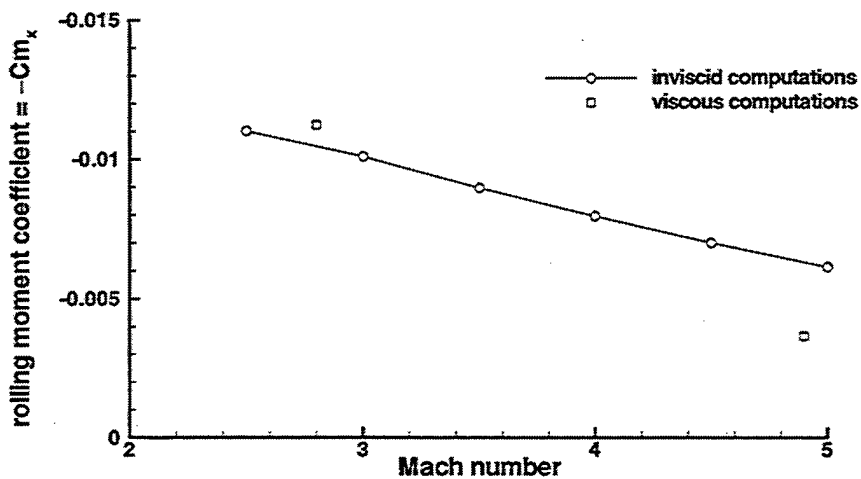


Figure 6.11 Computed rolling moments.

7. Conclusions and Recommendations

7.1 Conclusions

The structure of the flowfield near a single wrap-around fin (WAF) mounted on a semi-cylindrical body has been characterized using both experimental and numerical methods at Mach numbers of 2.8 and 4.9. A single-finned model was first extensively tested in the AFIT Mach 3 wind tunnel. In this experiment, the flow around the test article was surveyed at several stations along its length, concentrating on the region near the fin. While the boundary layer on the fin was determined to be too thin to survey with pressure or hot-film cross-wire probes, the boundary layer on the missile fuselage was easily explored using these devices. The result was a mapping of the pressure, velocity, and turbulent properties near the fin. The mean flow near the model was also obtained in the AFIT Mach 5 wind tunnel. Taken together, these experimental studies comprise a set of mean flow and turbulence data not previously available for curved fins.

Companion numerical studies were also performed wherein the Reynolds averaged Navier-Stokes equations were solved with the algebraic turbulence model of Baldwin and Lomax^[11] in the vicinity of the single-WAF model. The excellent agreement with experimental data suggests that the calculations have captured the relevant flow physics involved in this complicated flowfield. It is notable that the oil flow pattern of Abate and Berner^[2] to which these results compared so favorably was obtained on a four-finned missile. Thus the resemblance of computed and observed surface streamline patterns on the fin suggests that the present study, which uses a simplified single-fin model, captures the relevant flow features in the fin region for a non-spinning missile with *multiple* wrap-around fins. Taken in concert, the experimental and numerical results have been interpreted to characterize the flowfield in the vicinity of a wrap-around fin. Based on the results of this research, several conclusions may be made regarding the nature of the flowfield near wrap-around fins.

One of the more significant findings of the present study is that both inviscid and viscous properties play significant roles in determining the structure of the flowfield near WAFs. The outer flowfield exhibits asymmetries brought about by the effects of pressure

gradient, streamline curvature, and differing shock/expansion structures – while viscous phenomena induce asymmetries near the fuselage. Regarding the latter, the Navier-Stokes simulations predicted a vortex in the fin/body juncture on the convex side of the fin. This vortex, not present on the concave side presumably due to the oblique fin attachment angle, increases the pressure loading near the fin root. The net result is a pressure differential across the fin which alters the rolling moment. Both hot-film anemometry and surface flow visualizations corroborate the existence of this viscous-induced vortical structure. Inviscid simulations cannot capture this vortex and thus may not be expected to reasonably predict the stability behavior of missiles having WAFs.

That said, many aspects of the flowfield were accurately captured by solving the Euler equations. The bow shock created by the wrap-around fin is an inviscid phenomenon. Except in the immediate vicinity of the fin/body intersection where the bow shock interacts with the missile body boundary layer, the pressure field is dominated by inviscid effects. This has been demonstrated through the excellent agreement between measured quantities and those predicted by inviscid (as well as viscous) numerical methods in the outer region of the flow. The shock remains detached over the full span of the fin at Mach 2.8 and at Mach 4.9, and its interaction with the fuselage boundary layer creates the same type of λ -shock associated with blunt fins in supersonic flowfields.

The reduction of data from the pitot, cone-static and hot-film probes at Mach 2.8 produced a significant amount of turbulence data. Prior to this study, no detailed mean flow or turbulence measurements existed for WAF missile configurations. These data yielded some interesting insights. As expected, the bow shock causes a dramatic increase in turbulent kinetic energy and Reynolds shear stress on both sides of the fin. The flow experiences an expansion as it passes the fin which reduces the turbulence intensity. However, for a fixed streamwise location, the reduction is far greater on the convex side of the fin, where the flow experiences a stronger favorable pressure gradient over a longer distance. This results in lower turbulence intensities, producing lower, though still significant, shear stresses. It is notable that the turbulence model used was not designed to account for the effects of pressure gradient and streamline curvature. This may be largely responsible for the over-prediction of momentum levels in the outer boundary layer on the concave side of the fin in

the present numerical simulations. It is expected that these turbulence data will be useful for validation of turbulence closure models intended to predict flows having large pressure gradients.

At Mach 4.9, both the numerical and experimental results qualitatively resemble those obtained at Mach 2.8. Examination of the computed surface streamline patterns suggests that the flow structure in the inner viscous region is somewhat invariant over this range of Mach number. However, the juncture vortex is observed to shift slightly toward the body with increasing Mach number, causing a dramatic reduction in computed rolling moment compared to that predicted by inviscid theory. While the viscous computations did not predict a rolling moment reversal at either of the Mach numbers investigated, the predicted rolling moment had a much greater dependence on Mach number (in a manner consistent with a moment reversal) than inviscid simulations have projected. Again, this underscores the importance of viscous effects on the rolling moment.

7.2 *Recommendations*

Although the present study has provided clearer picture of the flowfield near a WAF in the given environment, it was by necessity limited in scope, and thus represents a first step toward understanding the flowfield dynamics of deployed missiles employing WAFs. What follows are suggested research areas that could expand the understanding of WAF aerodynamics. Unquestionably, this problem should continue to be addressed using both experimental and numerical means.

7.2.1 General. As a means of addressing the problems induced by the variation in rolling moment with Mach number, the current research suggests that remedies which act to alter, or perhaps even eliminate, the juncture vortex may provide fruitful. Techniques which act to reduce or eliminate much of the loading asymmetry near the root by altering the effective fin attachment angles should be explored.

7.2.2 Experimental. It is recommended that the experiment at Mach 4.9 be extended to include a hot-film exploration of the flowfield near the WAF model. The

data from such experiments would provide the same type of detailed flow angularity and turbulence data that were obtained at Mach 2.8. The AFIT Mach 5 wind tunnel is currently being modified to enable such measurements.

It is also suggested that surface flow visualization (oil film and/or pressure-sensitive paint) be obtained at several Mach numbers on both spinning and non-spinning WAF configurations to identify significant changes or bifurcations in the flow structure near the juncture. Such flow visualizations may also provide insight as to the effects of unit Reynolds number on the flow structure.

7.2.3 Numerical. From a numerical prospective, a reasonable next-step would be to study the effects of cross-flow on the flowfield near the fin. WAFs most certainly encounter cross-flow due to missile spinning and yaw (among other factors), which are likely to have significant effects on fin loading, perhaps further increasing the predicted effect of Mach number on the rolling moment. Experiments on sharp-fin/flat-plate geometries have demonstrated a considerable dependency of juncture vortex structure on cross-flow.^[33, 34] The effect of cross-flow could be numerically investigated for the current geometry by solving the governing equations subject to periodic boundary conditions.

Clearly numerical simulations which address fin interaction issues as well as the effects of Mach number and Reynolds number should be conducted. Further, simulations which employ turbulence models capable of resolving flowfields which are characterized by regions of large pressure gradient should be evaluated against the current body of experimental data.

8. Bibliography

1. Abate, Gregg L. *Aerodynamic Research of Wrap Around Fin Missile Configurations and Alternative Wrap Around Fin Designs.* , WL-TR-94-7015, February 1994.
2. Abate, Gregg L. and Claude Berner. "Wind Tunnel Measurements Wrap-Around Fins at Mach 2.06." Number AIAA Paper 94-3499. August 1994.
3. Abate, Gregg L. and Theresa Cook. "Analysis of Missile Configurations with Wrap-Around Fins using Computational Fluid Dynamics." Number AIAA Paper 93-3631. August 1993.
4. Abate, Gregg L. and W. Hathaway. "Aerodynamic Test and Analysis of Wrap Around Fins with Base Cavities." Number AIAA Paper 94-0051. January 1994.
5. Abate, Gregg L. and Wayne H. Hathaway. "Aerodynamics of Missiles with Offset Fin Configurations." Number AIAA Paper 89-3367. 1989.
6. Abate, Gregg L. and Gerald L. Winchenbach. "Aerodynamics of Missiles with Slotted Fin Configurations." Number AIAA Paper 91-0676. January 1991.
7. Aerosoft, Inc., Blacksburg, Virginia. *The General Aerodynamic Simulation Program, Version 3 Users Manual*, 1996.
8. Anderson, Dale A., et al. *Computational Fluid Mechanics and Heat Transfer*. Series in Computational Methods in Mechanics and Thermal Sciences, New York: Hemisphere Publishing Corporation, 1984.
9. Anderson, John D. *Modern Compressible Flow; with Historical Perspective* (Second Edition). New York: McGraw-Hill, Inc., 1990.
10. Anderson, John D. *Fundamentals of Aerodynamics* (Second Edition). New York: McGraw-Hill, Inc., 1991.
11. Baldwin, B. S. and H. Lomax. "Thin Layer Approximation and Algebraic Model for Separated Turbulent Flow." Number AIAA Paper 78-0257. January 1978.
12. Bardina, J. E. "Three-Dimensional Navier-Stokes Simulations with Two-Equation Turbulence Models of Interacting Shock-Waves/Turbulent Boundary Layer at Mach 8.3." *AIAA Paper 94-1905*. June 1994.
13. Bowersox, R. D. W. *Compressible Turbulence Measurements in a High-Speed High Reynolds Number Mixing Layer*. PhD dissertation, Virginia Polytechnic Institute and State University, Blacksburg, Virginia, September 1992.
14. Bowersox, R. D. W. *Thermal Anemometry*, chapter 15.4.2, 965-983. John Wiley & Sons, 1995.
15. Bowersox, R. D. W. and T. A. Buter. "Mass-Weighted Turbulence Measurements in a Mach 2.9 Boundary Layer Including Mild Pressure Gradients," *AIAA Journal*, 34(12):2479-2483 (December 1996).
16. Bowersox, R. D. W. and J. A. Schetz. "Compressible Turbulence Measurements in a High-Speed High Reynolds Number Mixing Layer," *AIAA Journal*, 32(4):758-764 (April 1994).

17. Cebeci, T. and A. Smith. *Analysis of Turbulent Boundary Layers* (Second Edition). London: Academic Press, Inc., 1974.
18. Cebeci, T., et al. "Solution of the Incompressible Turbulent Boundary Layer Equations with Heat Transfer," *Journal of Heat Transfer*, 92C:113-143 (1970).
19. Cebeci, T., et al. "Calculation of Compressible Adiabatic Turbulent Boundary Layers," *AIAA Journal*, 8(11):1974-1982 (October 1974).
20. Chen, C. L. and C. M. Hung. "Numerical Study of Juncture Flows," *AIAA Journal*, 30(7):1800-1807 (July 1992).
21. Chima, R. V. and J. W. Yokotsa. "Numerical Analysis of Three-Dimensional Viscous Internal Flow," *AIAA Journal*, 28(5):796-806 (May 1990).
22. Degani, D. and L. B. Schiff. "Computation of Supersonic Viscous Flows Around Pointed Bodies at Large Incidence." Number AIAA Paper 83-0034. January 1983.
23. Dolling, D. S. and S. M. Bogdonoff. "An Experimental Investigation of the Unsteady Behavior of Blunt Fin-Induced Shock Wave Turbulent Boundary Layer Interaction." Number AIAA Paper 81-1287. 1981.
24. Dolling, D. S. and S. M. Bogdonoff. "Blunt Fin-Induced Shock Wave Turbulent Boundary Layer Interaction," *AIAA Journal*, 20(12):1674-1680 (December 1982).
25. Dolling, D. S. and L. Brusniak. "Separation Shock Motion in Fin, Cylinder, and Compression Ramp-Induced Turbulent Interactions," *AIAA Journal*, 27(6):734-742 (June 1989).
26. Dotter, J. *Compressible Turbulence Measurements in a Supersonic Boundary Layer Including Adverse Pressure Gradient Effects*. MS thesis, School of Engineering, Air Force Institute of Technology (AU), Wright-Patterson AFB OH, December 1994.
27. Driver, Capt Mark A. *High-Resolution TVD Schemes for the Analysis of I. Inviscid Supersonic and Transonic Flows II. Viscous Flows with Shock-induced Separation and Heat Transfer*. PhD dissertation, School of Engineering, Air Force Institute of Technology (AU), Wright-Patterson AFB OH, December 1991.
28. Edge, Harris L. "Computation of the Roll Moment for a Projectile with Wrap-Around Fins," *Journal of Spacecraft and Rockets*, 31(4):615-620 (July-August 1994).
29. Edney, B. *Anomalous Heat Transfer and Pressure Distributions on Blunt Bodies at Hypersonic Speeds in the Presence of an Impinging Shock*. , FFA Report 115, Aeronautical Research Institute of Sweden, 1968.
30. Endevco Corporation, San Juan Capistrano, California. *General Catalog Binder*, 1992.
31. Endevco Corporation, San Juan Capistrano, California. *MODEL 4428A Pressure Indicator Instruction Manual*, 1994.
32. Engineering, Omega. *The Temperature Handbook*. Stanford, CT: Omega Engineering, Inc, 1990.

33. Fomison, N. R. *The Effects of Sweep and Bluntness on a Glancing Shock Wave Turbulent Boundary Layer Interaction*. PhD dissertation, Cranfield Institute of Technology, Bedford, United Kingdom, September 1986.
34. Fomison, N. R. and J. L. Stollery. "The Effects of Sweep and Bluntness on a Glancing Shock Wave Turbulent Boundary Layer Interaction." *AGARD Conference Procedures 428*. 8:1-8:18. North Atlantic Treaty Organization, 1987.
35. Gaitonde, D. and et. al. "A Systematic Comparative Study of Several High Resolution Schemes for Complex Problems in High Speed Flows." *AIAA Paper 91-0636*. January 1991.
36. Garrett, J. L. and S. A. Syed. "Application of Computational Fluid Dynamics to the Design of Space Transportation Main Engine Subscale Nozzel." Number AIAA Paper 92-3225. 1992.
37. Haidinger, F. A. and R. Friedrich. "Computation of Shock Wave/Turbulent Boundary Layer Interactions Using a Two-Equation Model with Compressibility Corrections," *Applied Scientific Research (The Hague)*, 51(1-2):501-505 (June 1993).
38. Hasen, G. "Turbulence Lecture Notes (AERO 827 - Unpublished)." January 1993.
39. Hiers, R. S. and W. J. Loubsky. *Effects of Shock-Wave Impingement on the Heat Transfer on a Cylindrical Leading Edge*. , NASA TN D-8859, February 1967.
40. Hirsch, C. *Numerical Computation of Internal and External Flows, Volumes 1 and 2*. New York: John Wiley and Sons, 1992.
41. Holden, M. S. "Shock-Shock Boundary Layer Interactions." *AGARD Report Number 764 - Special Course on Three-Dimensional Supersonic/Hypersonic Flows Including Separation*. 4:1-4:92. North Atlantic Treaty Organization, January 1990.
42. Holoman, J.P. *Experimental Methods for Engineers* (Fourth Edition). McGraw-Hill, Inc., 1984.
43. Hsu, J. C. and G. S. Settles. "Holographic Flowfield Density Measurements in Swept Shock Wave/Turbulent Boundary-Layer Interactions." Number AIAA Paper 92-0746. January 1992.
44. Huffman, Richard E., Jr. *Mach 2.9 Investigation Into the Flow Structure in the Vicinity of a Wrap-Around Fin*. MS thesis, School of Engineering, Air Force Institute of Technology (AU), Wright-Patterson AFB OH, December 1995.
45. Huffman, Richard E., Jr., et al. "Experimental Flow Structure Investigation of a Wrap-around Fin at Mach 2.9." Number AIAA Paper 96-2450. June 1996.
46. Hung, C-M. and P. G. Buning. "Simulation of Blunt-fin-induced Shock-wave and Turbulent Boundary Layer Interaction," *Journal of Fluid Mechanics*, 154:153-185 (January 1985).
47. Hung, C-M. and W. Kordulla. "A Time-Split Finite-Volume Algorithm for Three-Dimensional Flowfield Simulation," *AIAA Journal*, 22(11):1564-1572 (November 1984).

48. Jones, W. P. and B. E. Launder. "The Prediction of Laminarization with a Two-Equation Model of Turbulence," *International Journal of Heat and Mass Transfer*, 15(2):301-314 (1972).
49. Josyula, E., et al. "Nonequilibrium Hypersonic Flow Solutions Using the Roe Flux-Difference Split Scheme." *AIAA Paper 91-1700*. June 1991.
50. Kaufman, L. G., et al. *Shock Impingement Caused by Boundary Layer Separation Ahead of Fins.*, ARL TR-72-0118, August 1974.
51. Kim, K. S., et al. "Laser Skin Friction Measurements and CFD Comparison of Weak-to-Strong Swept Shock/Boundary Layer Interactions." Number AIAA Paper 90-0378. January 1990.
52. Kim, Y. H. and Gerald L. Winchenbach. "The Roll Motion of a Wraparound Fin Configuration at Subsonic and Transonic Mach Numbers." Number AIAA Paper 85-1777. August 1985.
53. Kistler, A. "Fluctuation Measurements in a Supersonic Turbulent Boundary-Layer," *Physics of Fluids*, 2(3):290-296 (1959).
54. Knight, Doyle D. "Numerical Simulation of 3-D Shock Wave Turbulent Boundary Layer Interactions." *AGARD Report 792*. North Atlantic Treaty Organization, August 1993.
55. Knight, Doyle D., et al. "The Flowfield Structure of the 3-D Shock Wave - Boundary Layer Interaction Generated by a 20 deg Sharp Fin at Mach 3." Number AIAA Paper 86-0343. January 1986.
56. Kopal, Z. *Tables of Supersonic Flow Around Cones*. Cambridge, MA: Murray Printing Company, 1947. MIT Center of Analysis Technical Report Number 1.
57. Kováshay, L. S. G. "The Hot-Wire Anemometer in Supersonic Flow," *Journal of the Aeronautical Sciences*, 17(9):565-572,584 (September 1950).
58. Kretschmar, R., et al. "Aerodynamic Characteristics of Wrap Around Fins on a Tube Launched Tactical Missile." Number AIAA Paper 95-1897. June 1995.
59. Kubendran, L. R., et al. "Experiments and Code Validation for Juncture Flows." *AGARD, Validation of Computational Fluid Dynamics. Volume 2: Poster Papers*. December 1988.
60. Kussoy, M. I. and K. C. Horstman. *Documentation of Two- and Three-Dimensional Shock-Wave/Turbulent Boundary-Layer Interaction Flows at Mach 8.2.*, NASA TM 103838, 1991.
61. Kussoy, M. I. and K. C. Horstman. "Three-Dimensional Shock-Wave/Turbulent Boundary-Layer Interactions," *AIAA Journal*, 31(1):8-9 (January 1993).
62. Kussoy, M. I., et al. "An Experimental Study of Three-Dimensional Shock-Wave/Turbulent Boundary-Layer Interactions at Hypersonic Mach Number." Number AIAA Paper 91-1761. June 1991.
63. Law, C. H. *3D Shock Wave - Turbulent Boundary Layer Interactions at Mach 6.*, ARL TR-75-0191, 1974.

64. Lee, Y. *Heat Transfer Measurements and Computations of Swept Shock Wave/Turbulent Boundary-Layer Interactions*. PhD dissertation, Department of Mechanical Engineering, Pennsylvania State University, June 1992.
65. Lee, Y., et al. "Heat Transfer Measurements and Computations of Swept Shock Wave/Turbulent Boundary-Layer Interactions," *AIAA Journal*, 32(4):726-734 (April 1992).
66. Liou, W. W. and T.-H. Shih. *On the Basic Equations for the Second-Order Modeling of Compressible Turbulence*. Lewis Research Center, Cleveland, Ohio: NASA Technical Memorandum 105277, October 1991.
67. Lomas, C. *Fundamentals of Hot Wire Anemometry*. Cambridge, MA: Cambridge University Press, 1986.
68. Marvin, Joseph G. "Turbulence Modeling for Computational Aerodynamics," *AIAA Journal*, 21(7):941-955 (July 1983).
69. McCann, G. *Compressible Turbulence Measurement in Low-Angle Injection into a Supersonic Flow*. MS thesis, School of Engineering, Air Force Institute of Technology (AU), Wright-Patterson AFB OH, May 1995.
70. McCann, G. and R. D. W. Bowersox. "Measurements Across the Plume of a Low Angled Supersonic Gaseous Injection into a Supersonic Free Stream," *AIAA Journal*, 34(2):317-323 (February 1996).
71. McGrory, W. D., et al. "Development and Application of GASP 2.0." Number AIAA Paper 92-5067. 1992.
72. McGrory, W. D., et al. *Version 2, The General Aerodynamic Simulation Program*. Aerosoft, Inc., Blacksburg, Virginia, 1992.
73. McMaster, D. L. and J. S. Shang. "A Numerical Study of Three-Dimensional Separated Flows Around a Sweptback Blunt Fin." *AIAA Paper 88-0125*. January 1988.
74. Miller, R. *Compressible Turbulence Measurements in a Supersonic Boundary Layer Including Favorable Pressure Gradient Effects*. MS thesis, School of Engineering, Air Force Institute of Technology (AU), Wright-Patterson AFB OH, December 1994.
75. Miller, R., et al. "Compressible Turbulence Measurements in Supersonic Boundary Layers With Favorable and Adverse Pressure Gradients," *Transactions of the ASME, Journal of Fluids Engineering, FED-224*:193-200 (August 1995).
76. Moran, Capt Kenneth J. *An Aerodynamic and Static-Stability Analysis of the Hypersonic Applied Research Technology (HART) Missile*. PhD dissertation, School of Engineering, Air Force Institute of Technology (AU), Wright-Patterson AFB OH, April 1994.
77. Morkovin, M. "Effects of High Acceleration on a Turbulent Supersonic Shear Layer," *Proceedings of the Heat Transfer and Fluid Mechanics Institute*, 4:1-17 (1955).
78. Morkovin, M. "Effects of Compressibility on Turbulent Flow." *The Mechanics of Turbulence* edited by A. Favré, New York: Gordon and Beach, 1964.

79. Nicolet Instrument Corporation, Madison, Wisconsin. *Nicolet MultiPro Systems Operation Manual: Data Acquisition Systems*, 1991.
80. North Atlantic Treaty Organization. *Special Course in 3-D Supersonic/Hypersonic Flows Including Separation*, January 1990.
81. North Atlantic Treaty Organization. *Special Course on Shock-Wave/Boundary-Layer Interactions in Supersonic and Hypersonic Flows*, August 1993.
82. Ozcan, O. *An Experimental Investigation of Three-Dimensional Boundary-Layer Separation in Supersonic Flow Past a Circular Cylinder on a Flat Plate*. PhD dissertation, University of California, Berkeley, March 1982.
83. Ozcan, O. and M. Holt. "Supersonic Separated Flow Past a Cylindrical Obstacle on a Flat Plate," *AIAA Journal*, 22(5):611-617 (May 1984).
84. Perry, A.E. *Hot-wire Anemometry*. Cambridge, MA: Oxford University Press, New York, 1982.
85. Pointwise, Inc., Bedford, Texas. *Gridgen Version 11 User's Manual*, 1996.
86. Pope, A. and K. Goin. *High-Speed Wind Tunnel Testing*. New York: John Wiley and Sons, Inc., 1965.
87. Price, A. E. and R. L. Stallings. *Investigation of Turbulent Separated Flows in the Vicinity of Fin Type Protuberances at Supersonic Mach Number*. , NASA TN D-3804, February 1967.
88. Rizzetta, Donald P. "Numerical Simulation of Turbulent Cylinder Juncture Flowfields." Number AIAA Paper 93-3038. July 1993.
89. Rodi, P. E. and D. S. Dolling. "An Experimental/Computational Study of Heat Transfer in Sharp Fin Induced Turbulent Interactions at Mach 5 : Experimental Results." Number AIAA Paper 92-0749. January 1992.
90. Rogers, M. *A Numerical Investigation of Pressure Gradient Effects on Supersonic Turbulent Flow*. MS thesis, School of Engineering, Air Force Institute of Technology (AU), Wright-Patterson AFB OH, September 1994.
91. Saida, N. and H. Hattori. "Shock Wave-Turbulent Boundary Layer Interaction Produced by a Blunt Fin," *Trans. Japan Soc. for Aeronautical and Space Sciences*, 27(76):67-77 (1984).
92. Sedney, Raymond and Clarence W., Jr. Kitchens. "Separation Ahead of Protuberances in Supersonic Turbulent Boundary Layers." *AGARD CP-168 - Flow Separation* 37:1-37:15, North Atlantic Treaty Organization, June 1975.
93. Sedney, Raymond and Clarence W., Jr. Kitchens. "Separation Ahead of Protuberances in Supersonic Turbulent Boundary Layers," *AIAA Journal*, 15(4):456-552 (April 1977).
94. Senseney, M. B. *Performance Characterization of a Highly Offset Diffuser With and Without Blowing Vortex Generator Jets*. MS thesis, School of Engineering, Air Force Institute of Technology (AU), Wright-Patterson AFB OH, December 1994.

95. Settles, Gary S. *Experimental Research on Swept Shock Wave/Boundary Layer Interactions Annual Report, 1 Apr. 1987 - 31 Mar. 1988.* , Pennsylvania State Univ., University Park. Dept. of Mechanical Engineering. Report No.: AD-A196938; PSU-ME-R-87/88-0031; AFOSR-88-0637TR, April 1988.
96. Settles, Gary S. and Lori J. Dodson. "Supersonic and Hypersonic Shock/Boundary-Layer Interaction Database," *AIAA Journal*, 32(7):1377-1383 (July 1994).
97. Smits, A and K. C. Muck. "Three Shock Wave/Turbulent Boundary Layer Interactions," *Journal of Fluid Mechanics*, 182(10):291-314 (1987).
98. Spangenberg, W. *Heat-Loss Characteristics of Hot-Wire Anemometers at Various Densities in Transonic and Supersonic Flow.* NACA-TN-3381, National Advisory Committee on Aeronautics, 1955.
99. Spina, E., et al. "The Physics of Supersonic Turbulent Boundary Layers," *Annual Review of Fluid Mechanics*, 26:287-319 (January 1994).
100. Steinbrenner, J. P., et al. *The GRIDGEN 3D Multiple Block Grid Generation System, Volume II: User's Manual.* , WRDC-TR-90-3022, 1991.
101. Steinbrenner, John P., et al. *The GRIDGEN 3D Multiple Block Grid Generation System, Volume 1: Final Report.* , WRDC-TR-90-3022, Flight Dynamics Laboratory, Wright Research and Development Center, July 1990.
102. Stoer, J. and R. Bulirsch. *Introduction to Numerical Analysis* (Second Edition). Springer-Verlag, 1993.
103. Stollery, J. L. "Glancing Shock-Boundary Layer Interactions." *AGARD Report Number 764 - Special Course on Three-Dimensional Supersonic/Hypersonic Flows Including Separation.* 6:1-6:30. North Atlantic Treaty Organization, January 1990.
104. Swenson, M., et al. "Aerodynamic Test and Analysis of Wrap-Around Fins at Supersonic Mach Numbers Utilizing Design of Experiments." Number AIAA Paper 94-0200. January 1994.
105. Tenekes, H. and J. L. Lumley. *A First Course in Turbulence.* Cambridge, Massachusetts: MIT Press, 1972.
106. Thomas, P.D. and J. F. Middlecoff. "Direct Control of the Grid Point Distribution in Meshes Generated with Elliptic Equations," *AIAA Journal*, 18:652-656 (1979).
107. Tilmann, Carl P. *Numerical and Experimental Investigation of the Turbulent Shock/Boundary-layer Interaction on a Wrap-Around Fin Configuration.* , AFIT PhD Prospectus, December 1994.
108. Tilmann, Carl P., et al. "Characterization of the Flowfield Near a Wrap-around Fin at Mach 2.8." Number AIAA Paper 97-0522. January 1997.
109. Tilmann, Carl P., et al. "Characterization of the Flow Structure in the Vicinity of a Wrap-around Fin at Supersonic Speeds." Number AIAA Paper 96-0190. January 1996.
110. Tilmann, Carl P., et al. "Experimental Investigation of the Flow Structure Near a Single Wrap-around Fin," *Journal of Spacecraft and Rockets*, 34(6):729-736 (November-December 1997).

111. TSI Incorporated, St. Paul, Minnesota. *IFA 100 System: Instruction Manual*, 1987.
112. van Leer, B. "Flux-Vector Splitting for the Euler Equations," *Lecture Notes In Physics*, 170 (1982).
113. Vitale, 1Lt Rico E., et al. "Aerodynamic Test and Analysis of a Missile Configuration with Curved Fins." Number AIAA Paper 92-4495. August 1992.
114. Vitt, P. H., et al. "The Validation and Application of Numerical Modeling to Supersonic Mixing and Reacting Flows." Number AIAA Paper 93-0606. January 1993.
115. Volluz, R. *Handbook of Supersonic Aerodynamics*. , NAVORD Report 1988, 1961.
116. White, Frank M. *Viscous Fluid Flow* (Second Edition). New York: McGraw-Hill, Inc., 1991.
117. Whyte, R. and W. Hathaway. "Subsonic and Transonic Aerodynamics of a Wraparound Fin Configuration." Number AIAA Paper 85-0106. January 1985.
118. Wilcox, D. *Turbulence Modeling for CFD*. Glendale, CA: DCW Industries, Inc., 1993.
119. Winchenbach, Gerald L., et al. "Subsonic and Transonic Aerodynamics of a Wraparound Fin Configuration." Number AIAA Paper 85-0106. January 1985.
120. Winkelmann, A. E. *Experimental Investigation of a Fin Protuberance Paritally Immersed in a Turbulent Boundary Layer at Mach 5*. , Naval Ordnance Laboratory Report NOLTR-72-33, January 1972.
121. Xenon Corporation, Woburn, Massachusetts. *Installation, Operation and Maintenance Manual*, 1994.

Appendix A. Turbulent Navier-Stokes Equations

A.1 Overview

It has become clear that computational fluid dynamics (CFD) will play an increasing role in the design of future high speed vehicles and weapons. In fact, due to the difficulties and large expense associated with ground testing such configurations, CFD is becoming a necessity in the design process. The flow over such vehicles is characterized by turbulent structures that are not well understood. This lack of understanding has remained the major obstruction to accurately simulating complicated high-speed flows, and turbulence modeling has remained the controlling factor in the accuracy of predicting such flows. Recently, Settles and Dodson^[96] pointed out that the modeling community is sorely lacking adequate experimental data that meets the high standards required by modern code validation. One of the objectives of the experimental portion of the research was to help fill that void.

Direct simulations (of relatively low Reynolds number flows over simple geometries) have shown that the Navier-Stokes equations are indeed the governing equations for turbulent flows. However, since turbulent flows are characterized by temporal and spatial scales that range over several orders of magnitude, direct numerical solutions of the unsteady Navier-Stokes equations for turbulent problems of practical interest are highly unlikely in the near future. Thus, researchers are restricted to considering time averages of turbulent motion, and to rely on approximation methods to provide solutions to high Reynolds number problems.

The two most prevalent forms of the governing equations are the Reynolds (time) averaged and Favré (mass-weighted-time) averaged forms of the N-S equations (RANS and FANS, respectively). In either case, additional fluctuation cross-correlation terms appear in the averaged form of the equations, resulting in a mathematical system having more unknowns than equations (details follow this section). Reducing the number of unknowns to the number of equations is known as the "closure" problem.^[68] Thus, the function of turbulence modeling is to accurately represent for these terms, either by expressing them as functions of mean flow properties, or by expressing them in terms of additional transport

equations. The form of the closure model depends on the type of averaging, Favré (FANS) or Reynolds (RANS). In the past, researchers have often made use of ad hoc assumptions to achieve closure of the N-S equations. The assumptions result in turbulence models that are rigorously incorrect. While these simplified turbulence models do serve a purpose and have had some degree of success, they are inadequate for predictions of compressible viscous/inviscid interactions such as shock/boundary-layer interaction.^[66, 96]

The Reynolds averaged equations are obtained by un-coupling the instantaneous flow properties into a time-average mean value plus a fluctuating turbulent contribution, e.g.,

$$\phi = \bar{\phi} + \phi'$$

where $\bar{\phi}$ is the time-averaged quantity, and ϕ' is the instantaneous turbulent fluctuating component. The Favré-averaged quantity and the Favré turbulent fluctuation of the quantity are given by

$$\tilde{\phi} = \frac{\overline{\rho\phi}}{\bar{\rho}} \quad \text{and} \quad \phi'' = \phi - \tilde{\phi}$$

respectively. Note that, by definition, the time average Reynolds fluctuation $\bar{\phi}'$, is zero, however, the time average of the Favré fluctuation, $\bar{\phi}''$, is non-zero. The form of the *compressible* FANS cross-correlation terms are very similar in appearance to those of the *incompressible* RANS. This coupled with Morkovin's hypothesis^[77] which states that "the turbulence structure is unaffected by compressibility as long as the fluctuation Mach number is less than unity" has led to the current virtually universal trend of adopting the FANS equations for high speed compressible flows. As a result, practically all compressible turbulence models represent direct extensions of incompressible formulations, where the constants are adjusted and the density is allowed to vary. Such corrections do little more than correlate the data upon which the models are based.^[75] In fact, Morkovin's own Mach 1.77 expansion fan/boundary layer interaction data^[78] suggests that the compressible $\overline{u\rho'v'}$ term in the Reynolds shear stress is of the same order as the typical incompressible $\overline{\rho u'v'}$ term.

A.2 Navier-Stokes Equations

In Cartesian coordinates the Navier-Stokes equations may be written^[66]:

Conservation of Mass

$$\rho_{,t} + (\rho u_j)_{,j} = 0 \quad (\text{A.1})$$

Conservation of Momentum

$$(\rho u_i)_{,t} + (\rho u_i u_j)_{,j} = \sigma_{ij,j} \quad (\text{A.2})$$

Conservation of Energy

$$(\rho E)_{,t} + (\rho E u_i)_{,i} = (\sigma_{ij} u_j)_{,i} - q_{i,i} \quad (\text{A.3})$$

or

$$(\rho H)_{,t} + (\rho H u_i)_{,i} = p_{,t} + (\tau_{ij} u_j)_{,i} - q_{i,i} \quad (\text{A.4})$$

where

$$\begin{aligned} E &= e + \frac{1}{2} u_i u_i, & H &= e + \frac{p}{\rho} + \frac{1}{2} u_i u_i, & e &= C_v T \\ \sigma_{ij} &= -p \delta_{ij} + \tau_{ij}, & \tau_{ij} &= 2\mu s_{ij} - \mu^* u_{k,k} \delta_{ij}, & s_{ij} &= \frac{1}{2} (u_{i,j} + u_{j,i}) \\ \mu^* &= \frac{2}{3} \mu - \mu_{bulk}, & q_i &= -\kappa T_{,i} \end{aligned} \quad (\text{A.5})$$

A.3 Reynolds (Time) Averaged Navier-Stokes Equations

When using Reynolds averaging, any given primitive flow quantity, ϕ , is expressed as the sum of a time-averaged component, $\bar{\phi}$ and a fluctuating component, ϕ' , as follows^[66]:

$$\begin{aligned} \rho &= \bar{\rho} + \rho' & u_i &= \bar{u}_i + u'_i & p &= \bar{p} + p' & T &= \bar{T} + T' & E &= \bar{E} + E' \\ H &= \bar{H} + H' & \mu &= \bar{\mu} + \mu' & \mu^* &= \bar{\mu}^* + \mu^{*'} & C_v &= \bar{C}_v + C'_v & C_p &= \bar{C}_p + C'_p \end{aligned}$$

The time average is defined by

$$\bar{\phi} = \frac{1}{T} \int_{t_0}^{t_0+T} \phi dt \quad (\text{A.6})$$

where the characteristic time T is long in comparison to the cycle times of the fluctuating component, but still permits gradual time-dependent fluid motion for non-stationary flows.

To obtain the mean flow equations, these expressions for the decomposed variables are substituted into the governing equations. These instantaneous equations are then time averaged, expanded, and simplified.^[105, 116] The results are the time averaged (or Reynolds averaged) Navier-Stokes equations given below in conservative form.^[38, 66, 13]

Mean Continuity

$$\bar{\rho}_{,t} + (\bar{\rho} \bar{u}_j - m_j^T)_{,j} = 0 \quad (\text{A.7})$$

Mean Momentum

$$(\bar{\rho} \bar{u}_i + \bar{\rho}' u_i')_{,t} + (\bar{\rho} \bar{u}_i \bar{u}_j)_{,j} = -\bar{p}_{,i} + (\tau_{ij} + \tau_{ij}^T)_{,j} \quad (\text{A.8})$$

Mean Energy

$$(\bar{\rho} \bar{e}_0 + \bar{\rho}' h_0')_{,t} + (\bar{\rho} \bar{h}_0 \bar{u}_j)_{,j} = (\bar{u}_i \bar{\tau}_{ij} + \bar{u}' \tau_{ij}' - q_j - q_j^T)_{,j} \quad (\text{A.9})$$

with the Equation of State

$$\bar{p} = \bar{\rho} R \bar{T} + R \bar{\rho}' T' \quad (\text{A.10})$$

where the compressible RANS turbulence terms have been defined to be

$$\begin{aligned} m_j^T &= -\overline{\rho' u_j'} \\ \tau_{ij}^T &= -\bar{\rho} \overline{u_i' u_j'} - \bar{u}_i \overline{\rho' u_j'} - \bar{u}_j \overline{\rho' u_i'} - \overline{\rho' u_i' u_j'} \\ q_i^T &= +\bar{\rho} \overline{h_0' u_i'} + \bar{h}_0 \overline{\rho' u_i'} + \bar{u}_i \overline{\rho' h_0'} + \overline{\rho' h_0' u_i'} \end{aligned} \quad (\text{A.11})$$

However, this process introduces an additional 6 unknowns. In these equations e_o and h_o are stagnation conditions (i.e., $e_o = e + \frac{1}{2} u_i u_i$). The terms which are due to Reynolds averaging are the turbulent apparent mass flux, m_i^T , compressible turbulent shear stress, τ_{ij}^T , and compressible turbulent heat flux, q_i^T . For thin layer flows, these reduce to:

$$m_y^T = -\overline{\rho' v'} \quad \tau_{xy}^T = -\bar{\rho} \overline{u' v'} - \bar{u} m_y^T \quad q_y^T = +\bar{\rho} \overline{h_0' v'} - \bar{h}_0 m_y^T \quad (\text{A.12})$$

and for incompressible flows:

$$m_i^T = 0 \quad \tau_{ij}^T = -\bar{\rho} \overline{u'_i u'_j} \quad q_i^T = +\bar{\rho} \overline{h'_0 u'_i} \quad (\text{A.13})$$

A.4 Favré Averaged Navier-Stokes Equations

When employing Favré averaging, any given primitive flow quantity, ϕ , is expressed as the sum of a mass-weighted-averaged mean value (Favré averaged), $\tilde{\phi}$, and a fluctuating component, ϕ'' . The Favré averaged quantity and the Favré turbulent fluctuation of the quantity are defined as^[66]:

$$\tilde{\phi} = \frac{\overline{\rho\phi}}{\bar{\rho}} \quad \text{and} \quad \phi'' = \phi - \tilde{\phi} \quad (\text{A.14})$$

It should be noted that although $\overline{\phi''} \neq 0$, it is also true that

$$\overline{\rho\phi} = \overline{\rho(\tilde{\phi} + \phi'')} = \overline{\rho\tilde{\phi}} + \overline{\rho\phi''} = \bar{\rho}\tilde{\phi} + \overline{\rho\phi''} = \bar{\rho}\frac{\overline{\rho\phi}}{\bar{\rho}} + \overline{\rho\phi''} = \overline{\rho\phi} + \overline{\rho\phi''}$$

so, it must be true that $\overline{\rho\phi''} = 0$. Also, the following relationships can be derived

$$\bar{\phi} - \tilde{\phi} = \phi'' - \phi' = \overline{\phi''} = -\frac{\overline{\rho'\phi''}}{\bar{\rho}} = -\frac{\overline{\rho'\phi'}}{\bar{\rho}}$$

The Favré averaged equations, as presented by Marvin^[68] (and corrected here), are

Continuity:

$$\frac{\partial \bar{\rho}}{\partial t} + \frac{\partial(\bar{\rho}\tilde{u}_i)}{\partial x_i} = 0 \quad (\text{A.15})$$

Momentum:

$$\frac{\partial(\bar{\rho}\tilde{u}_i)}{\partial t} + \frac{\partial(\bar{\rho}\tilde{u}_i\tilde{u}_j)}{\partial x_j} = -\frac{\partial \tilde{p}}{\partial x_i} + \frac{\partial(\bar{\tau}_{ij} - \overline{\rho u''_i u''_j})}{\partial x_j} \quad (\text{A.16})$$

Energy:

$$\frac{\partial \bar{\rho}\tilde{h}}{\partial t} + \frac{\partial(\bar{\rho}\tilde{h}\tilde{u}_j)}{\partial x_j} = \frac{\partial \tilde{p}}{\partial t} + \tilde{u}_j \frac{\partial \tilde{p}}{\partial x_j} + \overline{u''_j \frac{\partial p}{\partial x_j}} + \frac{\partial(-\bar{q}_j - \overline{\rho h'' u''_j})}{\partial x_j} + \overline{\tau_{ij} \frac{\partial u''_i}{\partial x_j}} \quad (\text{A.17})$$

These equations have the same form as the *incompressible* Reynolds averaged equations, except that the Reynolds stresses $\overline{\rho u_i'' u_j''}$ include the density fluctuations, which must be accounted for in some way. Compressibility is generally included by replacing the density with the mean density neglecting the terms which involve additional correlations arising from compressibility. Researchers using the Favré forms of the governing equations cite that avoiding some of the fluctuating density-generated terms simplifies closure of the system. However since much of the experimental data provides RANS-type information, modeling the effects of compressibility is problematic. The lack of an explicit fluctuating density component in the turbulent shear stresses is one of the specific shortcomings of this model.

The compressible FANS turbulence terms may be expressed as

$$m_i^T = 0 \quad \tau_{ij}^T = -\overline{\rho u_i'' u_j''} \quad q_i^T = \overline{\rho h_o'' u_i''} \quad (\text{A.18})$$

Note that these *compressible* Favré averaged terms are similar in appearance to their *incompressible* Reynolds averaged counterparts (Equation A.13). Bowersox and Schetz^[16] have shown that cross-wire anemometry is well suited for measurement of RANS turbulent terms. In particular, they have shown that the total shear stress can be directly measured for thin layer type flows. Furthermore, if the effects of the pressure fluctuations on the hot-wire response are small, then the multiple overheat cross-wire results can be decomposed into all of the terms in Equation A.11. This assumption has been verified by Bowersox and Schetz^[16] for a Mach 4.0 free mixing layer, and Kistler^[53] suggests that is valid for supersonic boundary layers up to Mach 4.7.

There are also forms of the Navier-Stokes equations in which both Reynolds- and Favré averaging are used.^[66] In these equations, the Reynolds average is often used for the density, pressure, transport coefficients, and specific heats, and Favré averaging is used for the other quantities.

A.5 Zero-Equation Turbulence Models (Baldwin-Lomax)

Both the RANS and FANS equations have additional fluctuation cross-correlation terms appear in the averaged form of the equations, causing them to have more unknowns than equations. Thus, turbulence modeling must be used to reduce the number of unknowns (or increase the number of equations) to close the system. This can be accomplished by expressing the cross-correlation terms as functions of mean flow properties, or by expressing them in terms of additional transport equations.

The following discussion is in no way intended to be a thorough review of turbulence modeling, but only a brief overview of the type of turbulence model used in the current research.

The simplest, and most widely used turbulence models are derivatives of the method of Cebeci and Smith [18, 19, 17]. The main drawback of this method is that the boundary layer thickness has to be known. In zero-equation (algebraic) models, the concept of a turbulent or eddy viscosity, μ_t , is used. This eddy viscosity is simply added to the molecular viscosity in the governing equations, i.e.,

$$\mu \rightarrow \mu + \mu_t$$

Also, a turbulent Prandtl number, Pr_t , is defined such that

$$\frac{\kappa}{C_p} \rightarrow \frac{\mu}{Pr} + \frac{\mu_t}{Pr_t}$$

in the energy equation. Baldwin and Lomax^[11] modified the model to eliminate the need for finding the edge of the boundary layer, δ .

$$\mu_t = \begin{cases} (\mu_t)_{\text{inner}} & y \leq y_c \\ (\mu_t)_{\text{outer}} & y_c < y \end{cases}$$

where y is the normal distance from the wall, and y_c is the smallest value of y at which the outer formulation is to be used.

The inner region is based on the Prandtl-van Driest formulation

$$(\mu_t)_{\text{inner}} = \rho \ell^2 |\omega|$$

where the mixing length and scaled coordinate are

$$\ell = ky \left[1 - e^{-y^+/A^+} \right] \quad \text{and} \quad y^+ = \frac{\rho_w u_\tau y}{\mu_w} = \frac{\sqrt{\rho_w \tau_w} y}{\mu_w}$$

where $u_\tau = \sqrt{\frac{\tau_w}{\rho_w}}$ is the friction velocity, and $|\omega|$ is the magnitude of the vorticity. The outer layer model is a modification of the Clauser formulation.

$$(\mu_t)_{\text{outer}} = K C_{\text{cp}} \rho F_{\text{wake}} F_{\text{kleb}}(y)$$

in which K is the Clauser constant, C_{cp} is a constant, and the wake function is given by

$$F_{\text{wake}} = \min \left\{ \begin{array}{c} y_{\text{max}} F_{\text{max}} \\ C_{\text{wk}} y_{\text{max}} u_{\text{diff}}^2 / F_{\text{max}} \end{array} \right\}$$

where F_{max} is the maximum value of the function

$$F(y) = y |\omega| \left[1 - e^{-y^+/A^+} \right]$$

and y_{max} is the value of y at which F_{max} occurs. The Klebanoff intermittency factor is given by

$$F_{\text{kleb}}(y) = \left[1 + 5.5 \left(\frac{C_{\text{kleb}} y}{y_{\text{max}}} \right)^6 \right]^{-1}$$

The constants specified to agree with Cebeci-Smith formulation for constant pressure boundary layers at transonic speeds, and are given as

$$\begin{array}{llll} A^+ = 26 & C_{\text{cp}} = 1.6 & C_{\text{kleb}} = 0.3 & C_{\text{wk}} = 0.25 \\ k = 0.4 & K = 0.0168 & Pr = 0.72 & Pr_t = 0.9 \end{array}$$

While simulating the flow about supersonic pointed bodies at large incidence, Degani and Schiff modified the method to properly account for the associated large regions of cross-flow separation.^[22] This allowed the method to more accurately predict these turbulent 3-D vortical flows using the thin layer parabolized Navier-Stokes (PNS) equations.

Appendix B. Hot-Film Methods for Turbulence

Care must be taken when comparisons between numerical and experimental results are made. However, it is clear that hot-film anemometry responds to time-averaged mass fluxes and total temperatures^[14]. The present research uses single-overheat thermal anemometry to measure the compressible Reynolds turbulence data in a Mach 2.8 ($Re/\ell=18 \times 10^6 m^{-1}$) flow involving a shock/boundary-layer interaction. Detailed three-dimensional surveys of pressure and mass fluxes have been obtained, enabling the calculation of turbulent quantities such as the turbulence intensities and Reynolds turbulent shear stresses.

The constant temperature hot-film anemometer^[84, 67] records the voltage required to maintain the film at a constant known temperature. The power required to maintain this temperature is equivalent to the heat transfer, q_f , between the hot-film and the surrounding flow. The Nusselt number can be related to the heat transfer from the film by

$$Nu = \frac{q_f}{\pi k \ell_f (T_f - T_e)} \quad (B.1)$$

Where T_e is the temperature the unheated film would approach under these specific flow conditions (equilibrium temperature).

The basic shape of a hot film probe used in this research is a cylinder and the form of the Nusselt number for compressible flow in dimensionless heat transfer is^[57]:

$$Nu = fcn(\ell_f/d, M, Pr, Re_e, \tau) \quad (B.2)$$

ℓ_f/d is the film aspect ratio; M is the Mach number; Pr is the Prandtl Number; Re_e is the effective cooling Reynolds number base on film diameter; and τ is the temperature loading factor. The *temperature loading factor* can be expressed as

$$\tau = \frac{T_f - T_e}{T_t}$$

where T_f is the film temperature and T_e is the equilibrium temperature, or the temperature that the unheated film would attain if placed in the flow. For Reynolds numbers greater

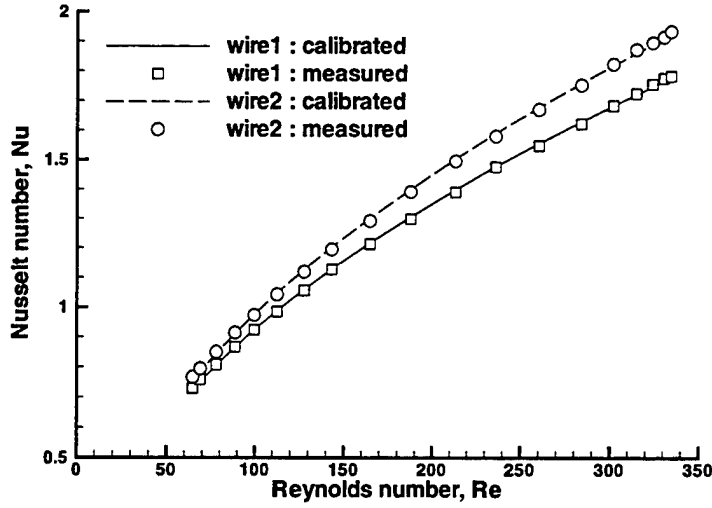


Figure B.1 Sample two-film calibration using *King's Law*.

than about 20, T_e is about 97% of T_t . When the Mach number normal to the film is greater than 1.2, or $M \sin \varphi \geq 1$, Pr is assumed constant, and the aspect ratio $\ell_f/d \gg 1$, the function for the Nusselt number simplifies to

$$Nu = fcn(Re_e, \tau) \quad (B.3)$$

It has been determined experimentally by Bowersox and Schetz^[16] that *King's Law*, the functional relationship between Nusselt number and Reynolds number for incompressible flow, is also an acceptable relationship for compressible flows.

$$Nu = a_k \sqrt{Re_e} + b_k \quad (B.4)$$

where the constants a_k and b_k must be experimentally determined for each value of T_f . Sample data from a two-film cross-wire calibration along with the corresponding *King's Law* curve fits are presented in Figure B.1. By definition, the Nusselt number is also proportional to the film power

$$Nu = \frac{q_f}{\pi k_t \ell_f (T_f - T_t)} \quad (B.5)$$

where

$$q_f = i_f^2 R_f \quad \text{and} \quad i_f = \frac{E_f}{R_f + R_s + R_L}$$

Here R_f is the film resistance, R_s is the resistance of the resistor in series with the film, and R_L is the probe lead resistance. Assuming that $T_e = T_t$ (which results in minimal error if done in both the calibration and the data reduction), the Nusselt number can be written as

$$\text{Nu} = \frac{E_f^2 R_f}{(R_f + R_s + R_L)^2} \frac{1}{\pi k_t \ell_f (T_f - T_e)} \quad (\text{B.6})$$

The turbulent power laws for viscosity and thermal conductivity are used to determine Nusselt and Reynolds numbers.

$$\begin{aligned} k_t &= k_0 \left(\frac{T_t}{T_0} \right)^{n_k} & n_k &= 0.89 \\ \mu_t &= \mu_0 \left(\frac{T_t}{T_0} \right)^{n_\mu} & n_\mu &= 0.77 \end{aligned} \quad (\text{B.7})$$

Combining (B.4), (B.6), and (B.7), gives the *hot film response equation*

$$\frac{E_f^2}{C_0} = \left(\frac{T_t}{T_0} \right)^{n_k} \left[a_k \sqrt{\text{Re}_{0_e}} \left(\frac{T_t}{T_0} \right)^{-n_\mu/2} + b_k \right] (T_f - T_t) \quad (\text{B.8})$$

where Re_{0_e} is the effective Reynolds number with $\mu = \mu_0$, and

$$C_0 = \frac{(R_f + R_s + R_L)^2}{R_f} \pi \ell_f k_0 \quad (\text{B.9})$$

B.1 Turbulence Fluctuations

Replacing E_f , Re_{0_e} , and T_t by their mean and fluctuating components in the *hot film response equation* (B.10), using the Binomial Theorem, retaining only the first order terms, and noting that

$$\frac{\overline{E_f^2}}{C_0} = \left(\frac{\overline{T_t}}{T_0} \right)^{n_k} \left[a_k \sqrt{\overline{\text{Re}_{0_e}}} + b_k \right] (\overline{T_f} - \overline{T_t}) \quad (\text{B.10})$$

then solving for E'_f/\overline{E}_f , the *hot film fluctuation equation* is derived in the form

$$\frac{E'_f}{\overline{E}_f} = f \left(\frac{\text{Re}_{0_e}'}{\overline{\text{Re}}_{0_e}} \right) + g \left(\frac{T'_t}{\overline{T}_t} \right) \quad (\text{B.11})$$

where the *hot film sensitivities* are given by

$$f = \frac{1}{4} \left[1 + \frac{b_k}{a_k \sqrt{\overline{\text{Re}}_e}} \right]^{-1} \quad \text{and} \quad g = \frac{-\overline{T}_t}{2(T_f - \overline{T}_t)} + \frac{n_k}{2} - f n_\mu \quad (\text{B.12})$$

For the single-overheat technique^[14], the sensitivity to total temperature fluctuation is minimized by operating the hot-film at large overheat ratios ($\frac{R_t}{R_{ref}} \approx 2$); hence g is small. For flows where the total temperature fluctuations, T'_t , is also small, the second term in Equation B.11 can be neglected. For Mach 3 boundary layers, the total temperature fluctuation has been found to be small ($\frac{T'_t}{\overline{T}_t} \approx 2-3\%$), thus neglecting that term is reasonable. Specifically, the AFIT Mach 3 wind tunnel has been found to maintain total temperature fluctuations below about 2.0%.^[44, 45, 70, 75] To evaluate f , $\overline{\text{Re}}_e$ is found from Equation B.10, where \overline{T}_t is assumed equal to the plenum total temperature, $T_{t\infty}$.

B.1.0.1 Decomposition into Cartesian Coordinates. To derive the formulas for analysis, the effective Reynolds number given by the previous section must be related to the x - y coordinate system. Since φ did not vary substantially from the calibration values, the cosine law was assumed valid, i.e.,

$$\begin{Bmatrix} \text{Re}_n \\ \text{Re}_t \end{Bmatrix} = \begin{bmatrix} \cos \varphi & \sin \varphi \\ -\sin \varphi & \cos \varphi \end{bmatrix} \begin{Bmatrix} \text{Re}_x \\ \text{Re}_y \end{Bmatrix} \quad (\text{B.13})$$

Thus the effective cooling Reynolds number becomes

$$\text{Re}_e^2 = A_1 \text{Re}_x^2 + 2A_2 \text{Re}_x \text{Re}_y + A_3 \text{Re}_y^2 \quad (\text{B.14})$$

where A_i are given by

$$\begin{aligned} A_1 &= \cos^2 \varphi \\ A_2 &= \cos \varphi \sin \varphi \\ A_3 &= \sin^2 \varphi \end{aligned} \quad (\text{B.15})$$

and φ is the incidence angle of the hot film to the flow.

Replacing Re_{0e} , Re_{0x} and Re_{0y} by their mean and fluctuating components and applying the binomial theorem, with $R_0 \ll 1$, one can show that

$$\overline{\text{Re}_{0ej}} \equiv \overline{\text{Re}_{0x}} \sqrt{B_{3j}} \quad (\text{B.16})$$

and write the *fluctuation equation* as

$$\left(\frac{\text{Re}_{0e}'}{\overline{\text{Re}_{0e}}} \right)_j \equiv B_{1j} \left(\frac{\text{Re}_{0x}'}{\overline{\text{Re}_{0x}}} \right) + B_{2j} \left(\frac{\text{Re}_{0y}'}{\overline{\text{Re}_{0x}}} \right) \quad (\text{B.17})$$

where the index j sums over the two films on the cross-film probe, and

$$\begin{aligned} R_0 &\equiv \frac{\overline{\text{Re}_{0y}}}{\overline{\text{Re}_{0x}}} = \overline{\rho v} / \overline{\rho u} \\ B_1 &\equiv \frac{A_1}{B_3} \\ B_2 &\equiv \frac{A_2}{B_3} \\ B_3 &\equiv A_1 + 2A_2 R_0 \end{aligned} \quad (\text{B.18})$$

Solving this set of equations and decomposing into x and y components

$$\begin{aligned} \overline{\text{Re}_{0x}}^2 &= \frac{\overline{\text{Re}_{0e1}}^2 / A_{21} - \overline{\text{Re}_{0e2}}^2 / A_{22}}{A_{11} / A_{21} - A_{12} / A_{22}} \\ \overline{\text{Re}_{0y}} &= \frac{1}{2\overline{\text{Re}_{0x}}} \frac{\overline{\text{Re}_{0e1}}^2 / A_{11} - \overline{\text{Re}_{0e2}}^2 / A_{12}}{A_{21} / A_{11} - A_{22} / A_{12}} \end{aligned} \quad (\text{B.19})$$

The turbulence variables can be decomposed into x and y components via (B.17) as

$$\overline{\left(\frac{Re_{0x}'}{Re_{0x}}\right)^2} = \frac{1}{D_2^2} \left[\frac{1}{B_{21}^2} \overline{\left(\frac{Re_{0e}'}{Re_{0e}}\right)_1^2} - \frac{2}{B_{21}B_{22}} \overline{\left(\frac{Re_{0e}'}{Re_{0e}}\right)_1 \left(\frac{Re_{0e}'}{Re_{0e}}\right)_2} + \frac{1}{B_{22}^2} \overline{\left(\frac{Re_{0e}'}{Re_{0e}}\right)_2^2} \right] \quad (B.20)$$

$$\overline{\left(\frac{Re_{0y}'}{Re_{0y}}\right)^2} = \frac{1}{D_1^2} \left[\frac{1}{B_{11}^2} \overline{\left(\frac{Re_{0e}'}{Re_{0e}}\right)_1^2} - \frac{2}{B_{11}B_{12}} \overline{\left(\frac{Re_{0e}'}{Re_{0e}}\right)_1 \left(\frac{Re_{0e}'}{Re_{0e}}\right)_2} + \frac{1}{B_{12}^2} \overline{\left(\frac{Re_{0e}'}{Re_{0e}}\right)_2^2} \right] \quad (B.21)$$

$$\overline{\left(\frac{Re_{0x}'}{Re_{0x}} \frac{Re_{0y}'}{Re_{0y}}\right)} = \frac{1}{2B_{11}B_{21}} \left[\overline{\left(\frac{Re_{0e}'}{Re_{0e}}\right)_1^2} - B_{11}^2 \overline{\left(\frac{Re_{0x}'}{Re_{0x}}\right)^2} + B_{21}^2 \overline{\left(\frac{Re_{0y}'}{Re_{0y}}\right)^2} \right] \quad (B.22)$$

where $D_1 = (B_{21}/B_{11} - B_{22}/B_{12})$ and $D_2 = (B_{11}/B_{21} - B_{12}/B_{22})$. The covariance of the two films can be expressed as

$$\overline{\left(\frac{E_f'}{E_f}\right)_1 \left(\frac{E_f'}{E_f}\right)_2} = f_1 f_2 \overline{\left(\frac{Re_{0e}'}{Re_{0e}}\right)_1 \left(\frac{Re_{0e}'}{Re_{0e}}\right)_2} \quad (B.23)$$

For the x - z plane, the above equations are used with w replacing v , and z replacing y . In this case, the cross-film is rotated 90 degrees (i.e. an x - z cross-film is used).

B.2 Turbulence Transformation - Reynolds Shear Stress

Bowersox and Schetz^[16] have shown that the Reynolds shear stress can be expressed in terms of the conservative cross-film variables as

$$\tau_{ij}^T = -\frac{\overline{(\rho u_i)' (\rho u_j)'}}{\bar{\rho}} + \bar{\rho} \bar{u}_i \bar{u}_j \overline{\left(\frac{\rho'}{\bar{\rho}}\right)^2}$$

where the second term on the right hand side has been shown to be much less than the first term for thin layer type flows. For the present flowfield, the flow angle was usually less than 5-10°, hence neglecting the second term would have probably been acceptable. In fact, the second term was calculated using the methods of Bowersox^[14] and was determined to be at least an order of magnitude smaller than the first term for all of the data presented.

Appendix C. Experimental Uncertainty Analysis

Error and uncertainty are inherent to experimental research. This section attempts to identify the possible sources of measurement error in the experiments, and then quantify the effects of these errors on the presented data. Based on the analysis presented by Bowersox^[13] the Euclidean (L_2) norm is utilized to assess the cumulative effects of error sources. The L_1 norm (a summation of the absolute error values) has been found to be too conservative an estimate when compared to a perturbation analysis of the data reduction equations. The L_2 norm of a set data, x_i , is defined by^[102]

$$\|x_i\|_2 = \|x_1, x_2, \dots, x_n\|_2 \equiv \left[\sum_{i=1}^n x_i^2 \right]^{\frac{1}{2}} \quad (\text{C.1})$$

Thus, the total dimensional error is defined to be^[42]

$$\mathcal{E}_R \equiv \|\mathcal{E}_{x_i}\|_2 = \left[\sum_{i=1}^n \left(\frac{\partial R}{\partial x_i} \mathcal{E}_{x_i} \right)^2 \right]^{\frac{1}{2}} \quad (\text{C.2})$$

where the index i runs over the various measurement errors, \mathcal{E}_{x_i} , associated with determination of the result, R . The dimensional errors can be normalized by reference values to obtain nondimensional errors (i.e. $\varepsilon_R = \mathcal{E}_R/R$). The effects of measurement errors were propagated through the data reduction process, where the equations were linearized to provide approximate error bounds on the processed data for the experiments.

C.1 Measurement Errors

Every measurement has an associated error. It is assumed all measurement errors are random, with a Gaussian distribution. The assumption of random errors precludes the existence of biased errors or blunders.

C.1.1 Conventional Probes. Pressure was measured by transducers which measure gauge pressure. An error of $\pm 0.0034 \text{ atm}$ was assumed in measurement of ambient pressure, determined by the smallest increment on the barometer.

The pressure transducers used to measure pitot, cone-static and plenum pressure are advertised to have accuracies of 0.5%, 0.5% and 0.4%, respectively.^[30] Calibration and digital conversion of the pressure data for storage and processing also adds error. All pressure readings were conditioned the same style of indicator (Endevco 4428A) with a maximum gain error of $\pm 0.5\%$ and gain stability of $\pm 0.2\%$.^[31] The probe pressure units were re-zeroed daily, and never deviated more than 0.01psi or 0.1psi for the probe and plenum pressures, respectively. Finally, Volluz^[115] reports that turbulence induces about $\pm 0.0068\text{atm}$ error for both pitot and cone static probe types.

Using multiple overheat (MOH) hot-film anemometry, the AFIT Mach 3 wind tunnel has been found to have boundary layer total temperature root mean square (RMS) fluctuations of 2.0%.^[174, 69] The RMS fluctuations are included as errors in this analysis as they provide a definitive bound of measurement uncertainty from large data samples. The plenum total temperature was observed to vary no more than $\pm 2.36\text{K}$ during tunnel runs. The plenum thermocouple and display unit were accurate to within $\pm 1\text{K}$.

The degree of flexing experienced by each type of probe during tunnel operation was determined by aligning two grids onto the Plexiglas plates to measure x and y position. The flex angle and position were then determined as a function of initial measured position, and accurate to within 1° (1.1mm). The measurement of x and y position was accurate to $\pm 0.5\text{mm}$. Without Plexiglas windows on the top and bottom of the tunnel, it was more difficult to determine the z position of each probe. The error in z position was assumed to be twice the measurement error in x or y (1.0mm). An additional error from digitization occurred in the measurement of y position - as y position was recorded using a linear displacement voltage transducer, LDVT. Since the LDVT was sampled with a 12.0V range, the above error in digitization voltage was multiplied by the calibration slope. This manipulation resulted in an error in y position from digitization of $\pm 0.015\text{mm}$. Errors in position were also incurred due to the flexing of the probes during tunnel operation.

C.1.2 Hot-Film Probes. The possibility of measurement error is greatest in the angular rotation of the probe. Since the probes are calibrated at an upstream location then moved to the downstream measurement locations, great efforts were taken to ensure

that the probe remained aligned with the tunnel axis. Probe alignment was "spot checked" where possible by examining the measured flow angularity in the freestream.

Hot-wire measurements have shown 1.0% root mean square fluctuation in voltage for freestream flow. Additionally, a digitization error of $\pm 0.003V$ was accounted for in the 12.0V sampling range. The errors in pressure, temperature, position and voltage have been summarized in Table C.1.

Table C.1 Measurement error bounds.

Measured Property, x	Error	
	Mach 2.8	Mach 4.9
x	1.2mm	1.2mm
y	0.5mm	0.5mm
z	1.0mm	1.0mm
T_{t1}	2.3%	2.2%
P_{t1}	0.8%	0.7%
P_{t2}	0.9%	0.8%
P_{cs}	3.5%	1.3%
E_f	1.0%	---

C.2 Error Propagation

The errors listed in Table C.1 have an influence on all subsequent data reduction. To determine the influence on calculations, the equations used are linearized about freestream conditions.^[44] Tables C.2 and C.3 list the freestream conditions and typical freestream hot-film calibration parameters used in the analysis, as well as to normalize the uncertainty estimates.

C.2.1 Properties Determined with Pressure Probes. The majority of mean flow calculations are based on the local Mach number, where the Mach number is calculated from a curve fit to experimental data (Equations 3.1 and 3.2). As an example of error propagation, the analysis is applied to Equation 3.1 which is of the form

$$\frac{1}{M} = C_0 + C_1\xi + C_2\xi^2 + C_3\xi^3 + C_4\xi^4 \Rightarrow M = M^2[C_0 + C_1\xi + C_2\xi^2 + C_3\xi^3 + C_4\xi^4]$$

Table C.2 Freestream conditions.

Condition	M=2.8 Value	M=4.9 Value
T_{t1}	294K	354K
P_{t1}	2.085atm	32.0atm
P_{t2}	0.7175atm	1.86atm
P_{cs}	0.1017	0.3388atm
ξ	0.1417	0.1725
M	2.80	4.90
γ	1.4	1.4
R_{air}	$287.1 \frac{m^2}{s^2 K}$	$287.1 \frac{m^2}{s^2 K}$
T	114.5K	61.5K
a_∞	$214.48 \frac{m}{s}$	$157.19 \frac{m}{s}$
P_1	0.065atm	0.070atm
ρ_1	$0.2432 \frac{kg}{m^3}$	$0.3977 \frac{kg}{m^3}$
u	$600.5 \frac{m}{s}$	$766 \frac{m}{s}$
$\rho_1 u$	$140.6 \frac{kg}{m^2 s}$	$304.7 \frac{kg}{m^2 s}$
Re_∞	$1.8 \times 10^6 / m$	$75 \times 10^6 / m$

Table C.3 Typical freestream hot-film parameters (M=2.8).

Condition	Value
E_f	5.0V
T_f	700.0K
T_e	294.0K
R_f	10.0 Ω
R_s	50.0 Ω
R_L	0.0 Ω
a_k	0.11
b_k	-0.10
d	$5.1 \cdot 10^{-5} m$
L	0.001m
Re_e	300
Nu(wire)	1.8

Application of Equation C.2 results in the normalized error at Mach 2.8 of

$$\varepsilon_M = \frac{\varepsilon_M}{M} = \|M(C_1\xi + 2C_2\xi^2 + 3C_3\xi^3 + 4C_4\xi^4) \cdot \varepsilon_\xi\|_2 = 0.725\varepsilon_\xi \quad (C.3)$$

Similarly, Equation 3.2 at Mach 4.9 gives

$$\varepsilon_M = \|M(C_1\xi + C_2\xi) \cdot \varepsilon_\xi\|_2 = 0.855\varepsilon_\xi \quad (C.4)$$

The pressure ratio, ξ is the ratio of pressures measured with a 10° or 20° cone-static probe and a pitot probe.

$$\xi = \frac{P_{cs}}{P_{t1}} \Big|_{cs} \cdot \frac{P_{t1}}{P_{t2}} \Big|_{t2} \quad (C.5)$$

Two different plenum pressures ($P_{t1}|_{t2}$ and $P_{t1}|_{cs}$) are used to minimize errors caused by differences between the two separate tunnel runs (one for each probe). Since ξ was a combination of pressure measurements, the errors combine with the Euclidean norm

$$\varepsilon_\xi = \|2\varepsilon_{P_{t1}}, \varepsilon_{P_{t2}}, \varepsilon_{P_{cs}}\|_2 \quad (C.6)$$

The Mach number and plenum temperature were used to derive the local tunnel temperature, T_1 , assuming isentropic flow. Although isentropic flow was violated by shocks, no method for measuring local temperature was available. The equation of state and ideal gas laws were then used to calculate density and speed. Table C.4 summarizes the propagation errors of the pressure probe measurements.

C.2.2 Properties Determined with Hot-film Measurements. Single overheat (SOH) hot-film anemometry was used to measure mass-flux mean flow and RMS fluctuations. SOH analysis assumes negligible total temperature fluctuations and has proved to be valid for this experimental facility.^[74, 26] Additionally, cross-wire measurements provided flow direction information. A detailed explanation of the hot-film data reduction techniques which were used is presented in Appendix B. Due to the complicated nature of the hot-film data reduction, a logarithmic/derivative technique^[44] was applied to the hot-film data reduction equations to estimate the propagation of errors throughout the hot-film analysis.

Table C.4 Pressure probe related error bounds.

Calculated Property	Derivation		Error	
	M=2.8	M=4.9	M=2.8	M=4.9
ξ	$\ 2\varepsilon_{P_{t1}}, \varepsilon_{P_{t2}}, \varepsilon_{P_{cs}}\ _2$	$\ 2\varepsilon_{P_{t1}}, \varepsilon_{P_{t2}}, \varepsilon_{P_{cs}}\ _2$	3.9%	2.0%
M	$0.725\varepsilon_\xi$	$0.855\varepsilon_\xi$	2.8%	1.7%
T_1	$\ \varepsilon_{T_{t1}}, 1.221\varepsilon_M\ _2$	$\ \varepsilon_{T_{t1}}, 1.655\varepsilon_M\ _2$	4.1%	3.6%
a	$0.5\varepsilon_{T_1}$	$0.5\varepsilon_{T_1}$	2.1%	1.8%
P_1	$\ \varepsilon_{P_{t2}}, 1.907\varepsilon_M\ _2$	$\ \varepsilon_{P_{t2}}, 1.970\varepsilon_M\ _2$	5.5%	3.5%
ρ_1	$\ \varepsilon_{P_1}, \varepsilon_{T_1}\ _2$	$\ \varepsilon_{P_1}, \varepsilon_{T_1}\ _2$	6.9%	5.0%
u	$\ \varepsilon_M, \varepsilon_\alpha\ _2$	$\ \varepsilon_M, \varepsilon_\alpha\ _2$	3.5%	2.5%

The Nusselt number (of the hot-film), Nu , was determined from the power consumption required to maintain a constant wire temperature (Equation B.6). The error in Nu was a function of the measured voltage error and total temperature error. The effective Reynolds number, Re_e , was determined by a curve fit of Nu (*King's Law*, Equation 3.3). Additionally, the fluctuation in Re_e was a function of measured voltage error. These errors were combined under the L_2 norm. The error in mass-flux is equivalent to the error in Reynolds number, and it assumes that the transverse mass-fluxes suffer the same error as the axial component. Table C.5 summarizes the propagation errors of the hot-film probe measurements.

C.2.3 Separation of Primitive Fluctuations. The separation equations for the primitive fluctuations were linearized about the reference conditions of Table C.2. The results of variable separation error analysis are summarized in Table C.6.

C.3 Comparison of u - v and u - w Hot-film Probes

The agreement between the axial mean and fluctuating quantities obtained by the two probes was considered excellent (Figure C.1). The small differences were attributed primarily to the high flow angles ($\phi \approx \pm 10^\circ$) experienced by the probes which have finite (1mm) wire separations.

Table C.5 Hot-film related error bounds (M=2.8).

Calculated Property	Derivation	Error
Nu	$\ 2.0\varepsilon_{E_f}, \varepsilon_{T_{t1}}\ _2$	3.0%
Re _e	$\ 2.0\varepsilon_{Nu}, \varepsilon_{E_f}\ _2$	6.1%
f	$0.5\varepsilon_{Re_e}$	3.1%
g	$\ \varepsilon_{T_{t1}}, \varepsilon_f\ _2$	3.8%
Re _e ²	$2.0\varepsilon_{Re_e}$	12.2%
Re _x ²	$\ \varepsilon_{Re_{e1}^2}, \varepsilon_{Re_{e1}Re_{e2}}, \varepsilon_{Re_{e2}^2}\ _2$	21.2%
Re _x Re _y	$\varepsilon_{Re_x^2}$	21.2%
Re _x Re _z	$\varepsilon_{Re_x^2}$	21.2%
Re _x	$0.5\varepsilon_{Re_x^2}$	10.6%
Re _y	ε_{Re_x}	10.6%
Re _z	ε_{Re_x}	10.6%
ρu	ε_{Re_x}	10.6%
ρv	ε_{Re_y}	10.6%
ρw	ε_{Re_z}	10.6%

Table C.6 Turbulent fluctuation error bounds (M=2.8).

Calculated Property	Derivation	Error
(ρu)'	ε_{Re_x}	10.6%
(ρv)'	ε_{Re_y}	10.6%
(ρw)'	ε_{Re_z}	10.6%
(ρu)'(ρv)'	$\varepsilon_{Re_xRe_y}$	21.2%
(ρu)'(ρw)'	$\varepsilon_{Re_xRe_z}$	21.2%
ρ'	$\ 0.458\varepsilon_M, 0.771\varepsilon_{(\rho u)'}\ _2$	8.3%
u'	$\ \varepsilon_{\rho'}, \varepsilon_{(\rho u)'}\ _2$	13.4%
v'	$\varepsilon_{u'}$	13.4%
w'	$\varepsilon_{u'}$	13.4%

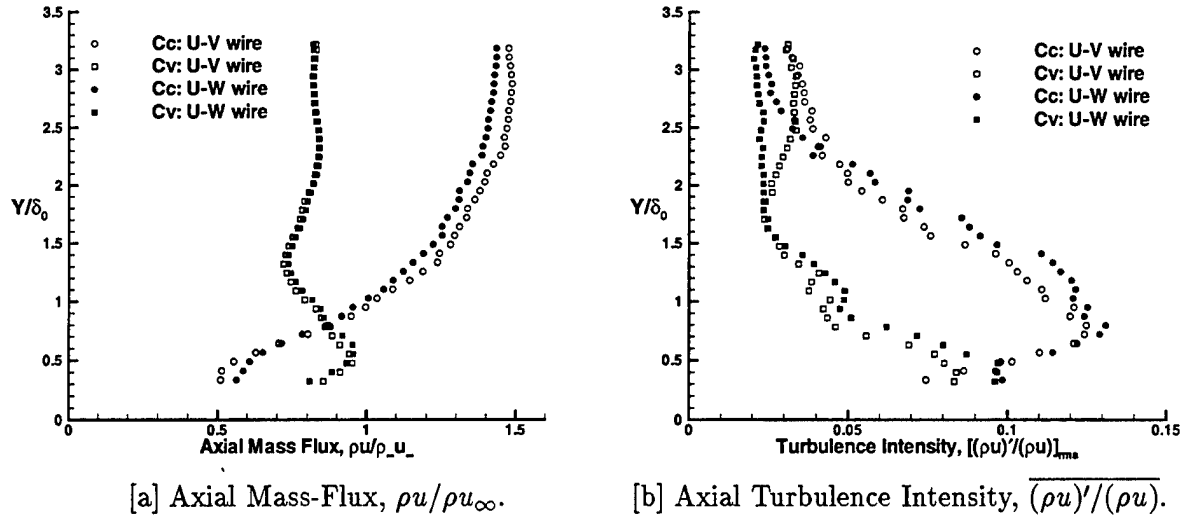
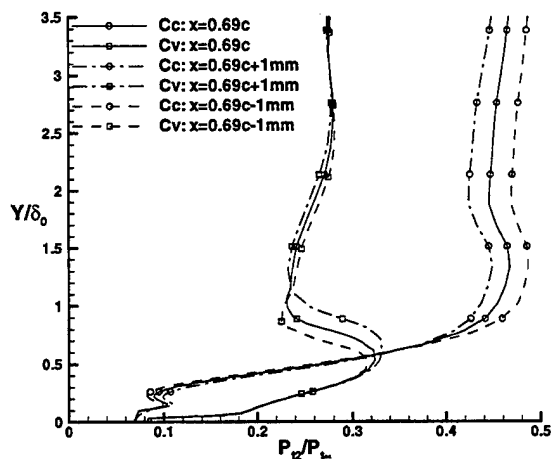


Figure C.1 Comparison of hot-wire probe orientation at $x=0.69c$ ($M=2.8$).

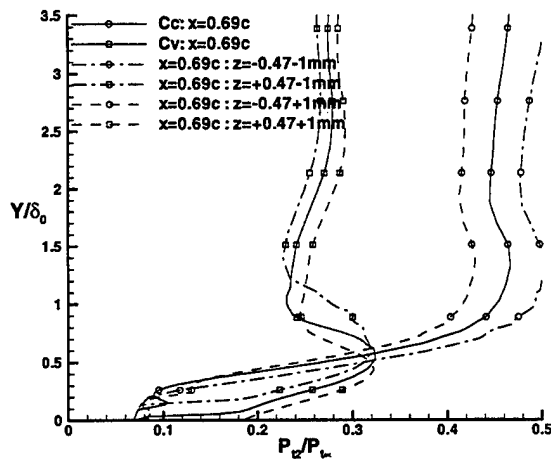
C.4 Assessment of Probe Location Error Using Numerical Solutions

The effects of probe location error were also assessed by ‘probing’ the computational results. By assuming a location error, then examining the CFD results at the extremes of that error band, an estimate of the sensitivity of measured flowfield variables to probe location error may be ascertained. Figure C.2 shows the effect that a $\pm 1\text{mm}$ probe location error in the x and z directions (in the numerical solution) has on the measured pitot pressure. Due to the high transverse pressure gradients, the measured data are more sensitive to variations in z (with measurement errors of up to 8.5%) than it is to x (up to 5.5% on the concave side). In reality, it is likely that the probe experiences less flexing as it is moved away from the model wall. If this is true, Δx becomes less positive as Y/δ increases, and a profile more closely resembling the experimentally observed data (without the acceleration peak over $Y/\delta \in [0.8, 1.8]$) could result on the concave side of the fin. The measured data on the convex side would be relatively unaffected as it is comparatively invariant with Δx .

Many of the differences between measured and predicted flow angularity may also be attributed to probe location errors. Figures C.3 through C.6 show the effects of a $\pm 1\text{mm}$ probe location error in the x and z directions on the calculated flow angularities. For example, at a location only 1mm closer to the fin than estimated on the convex side, the nu-



[a] Axial $\Delta x = \pm 1\text{mm}$.

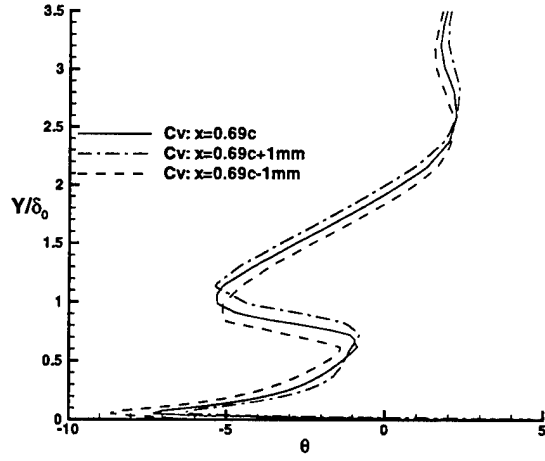


[b] Transverse $\Delta z = \pm 1\text{mm}$.

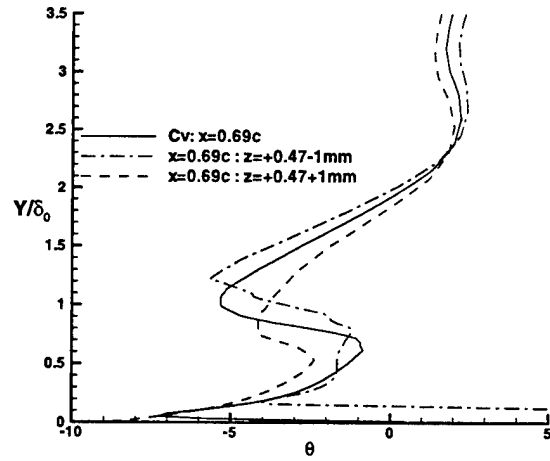
Figure C.2 Effect of a variation in probe position on computed pitot pressure ($M=2.8$).

merical simulation almost exactly reproduces the experimentally observed flattening of the horizontal angularity, θ , near the body ($0.3 < Y/\delta_0 < 0.8$) (cf Figures 5.8[c] and C.3[b]). At this same location, the experimentally observed inflection seen in the azimuthal flow angle, ϕ , is also very closely reproduced in the numerical solution (cf Figures 5.8[d] and C.4[b]).

On the concave side of the fin, moving the probe location 1mm further away from the fin (in the numerical solution) yields the drastic reduction in the horizontal flow angularity, θ , near the body ($Y/\delta_0 < 0.7$) similar to that observed in the experiment (cf Figures 5.9[c] and C.5[b]). The sensitivity of θ to probe location error in the z direction in this region ($z/c \approx -0.47$) can also be seen in Figure 5.11[a]. Near the body, the flow can be directed either toward or away from the body with a small variation in z .

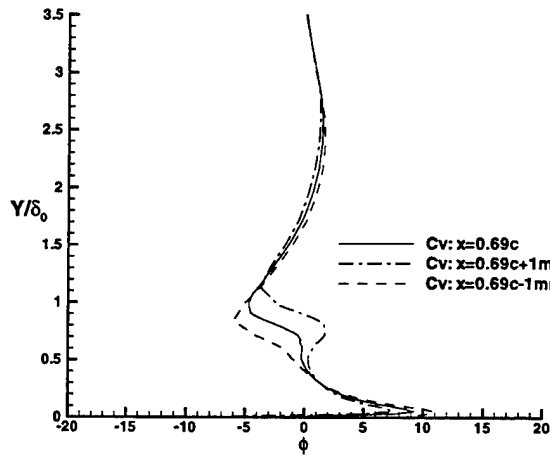


[a] Axial $\Delta x = \pm 1\text{mm}$.

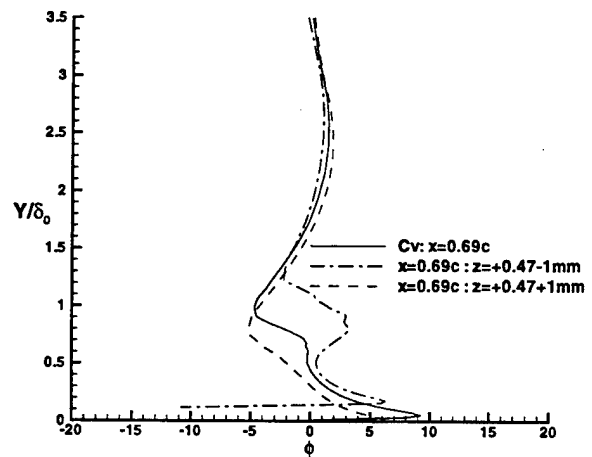


[b] Transverse $\Delta z = \pm 1\text{mm}$.

Figure C.3 Effect of a variation in probe position on θ ; convex side ($M=2.8$).

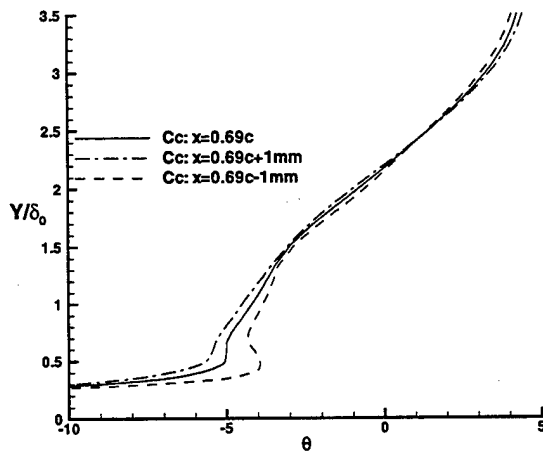


[a] Axial $\Delta x = \pm 1\text{mm}$.

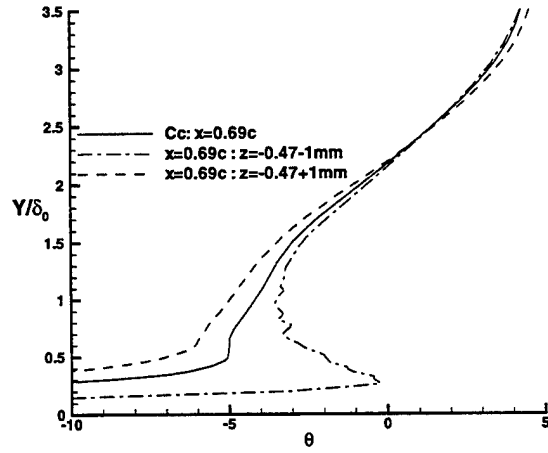


[b] Transverse $\Delta z = \pm 1\text{mm}$.

Figure C.4 Effect of a variation in probe position on ϕ ; convex side ($M=2.8$).

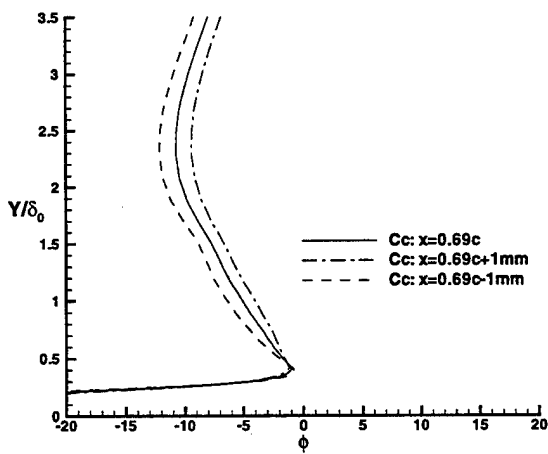


[a] Axial $\Delta x = \pm 1\text{mm}$.

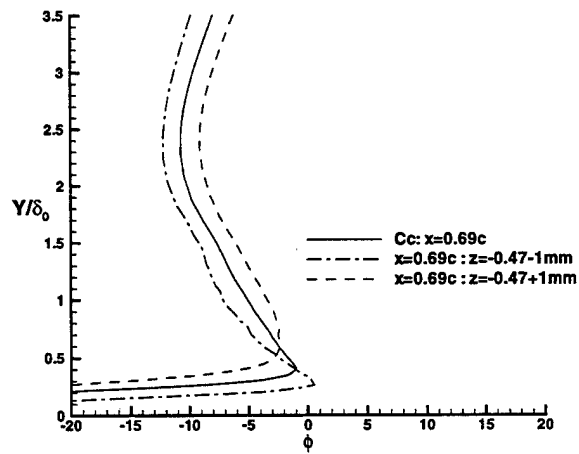


[b] Transverse $\Delta z = \pm 1\text{mm}$.

Figure C.5 Effect of a variation in probe position on θ ; concave side ($M=2.8$).



[a] Axial $\Delta x = \pm 1\text{mm}$.



[b] Transverse $\Delta z = \pm 1\text{mm}$.

Figure C.6 Effect of a variation in probe position on ϕ ; concave side ($M=2.8$).

Appendix D. Mach 5 Wind Tunnel

D.1 Overview

The AFIT Mach 5 wind tunnel is a blow-down design (as illustrated in Figure D.1) which operates over a range of Reynolds numbers. Since the static temperature for Mach 5 flow at standard day total temperature is below the liquefaction temperature of oxygen, the air is heated by a refractive pebble-bed heating system. The nominal chamber total pressure and temperature are 20–32atm and 350–375K respectively, yielding a freestream Reynolds number $Re/\ell \approx 32\text{--}75 \times 10^6 \text{m}^{-1}$. The nominal tunnel conditions experienced in the tunnel for the present research are shown in Table D.1. Although the tunnel is capable of sustaining longer run times, it is typically run for only 10–15 seconds. The design, construction, and instrumentation of this facility comprised a significant portion of this research effort.

D.2 Air Supply

High pressure air is stored in a 175atm tank (Figure D.2) having a capacity of 1.25 cubic meters, and is controlled with a high volume dome regulated control valve (Figure D.3). The tank is recharged with a four-stage compressor and dryer system (Figure D.4). This system provides enough air to run the tunnel at a plenum pressure of 20atm for over 2 minutes, and requires about 5 hours to re-charge, although actual run-times are never expected to exceed 30 seconds in order to allow several runs during a day.

Table D.1 Typical Mach 5 tunnel freestream conditions (used for viscous CFD).

Condition	Value
M	4.87
P_t	$3.23 \times 10^6 \text{Pa} = 32.0 \text{atm}$
P	$7.017 \text{kPa} = 0.070 \text{atm}$
T_t	354K
T	61.5K
u	$766 \frac{\text{m}}{\text{s}}$
ρ	$0.3977 \frac{\text{kg}}{\text{m}^3}$

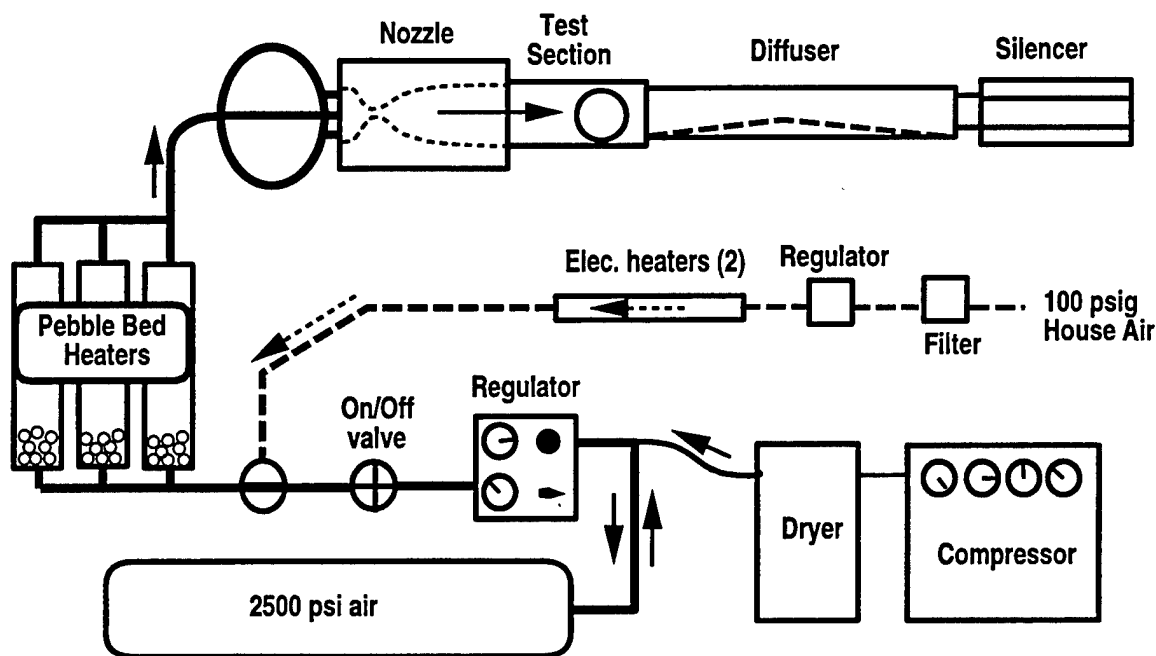


Figure D.1 Mach 5 wind tunnel schematic.

In the present configuration, both the run time and down time are determined by the heating system. The system passes the high-pressure air through a bank of refractory pebble-bed heaters (Figure D.5) before it enters the tunnel. To accomplish the heater design, computer programs (in both FORTRAN and Mathcad) were developed which implement the heater design method of Pope and Goin.^[86] Each of the pebble beds are designed to heat the air to 375K before entering the tunnel, which keeps the static temperature in the tunnel well above the liquefaction temperature. This temperature can be maintained or exceeded for several seconds, and is monitored by a thermocouple in the settling chamber. The air can easily be heated to higher or lower temperatures by heating the pebble beds to other initial temperatures. The heater system is designed to be very flexible, allowing the use of single or multiple heaters during a run. This is accomplished by channeling the air from the heaters through a manifold before entering the tunnel, which allows them to be run independently or in parallel. In practice, two heaters are usually run in parallel, providing enough heat for three runs, each sustaining acceptable temperatures for 8–12 seconds of 10–15 second runs.

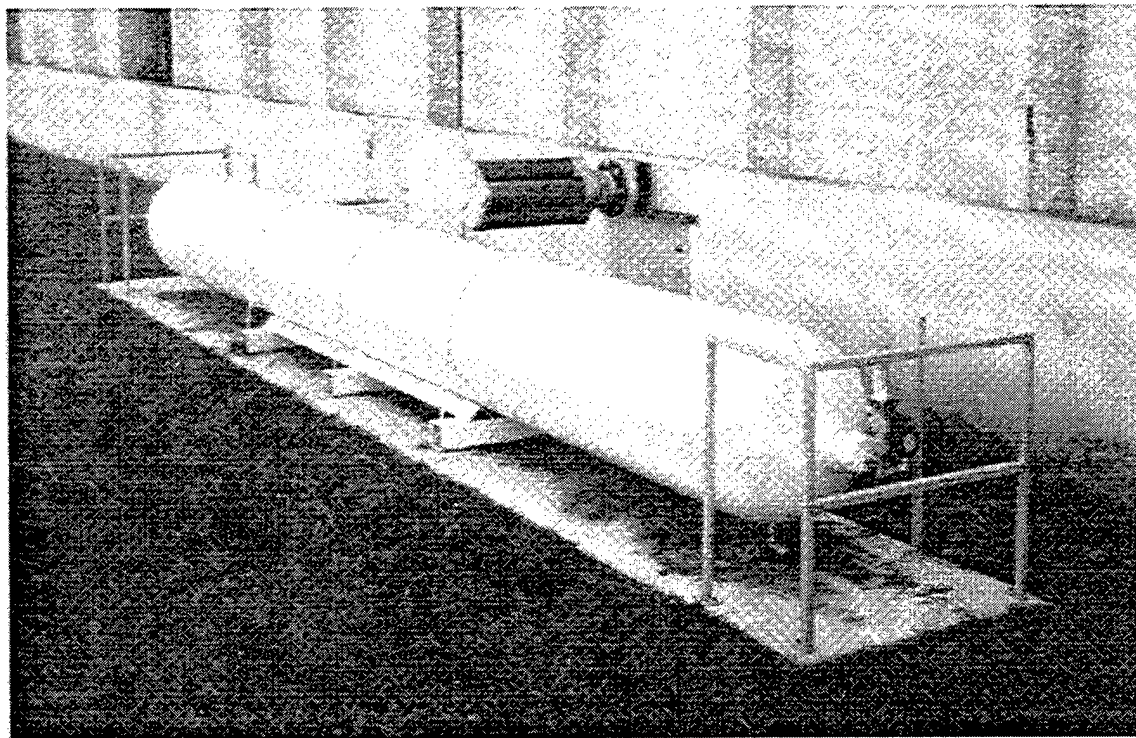
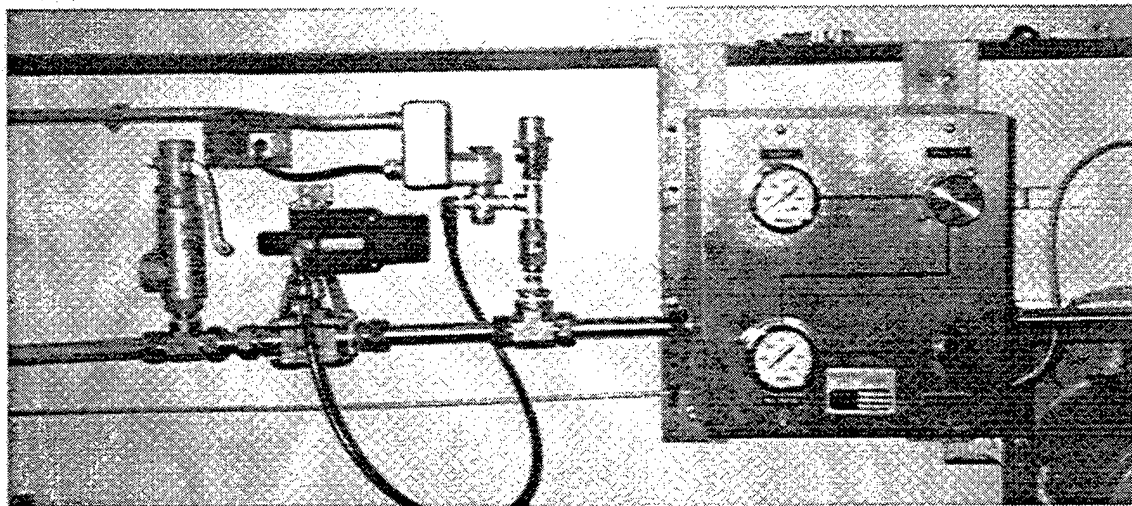
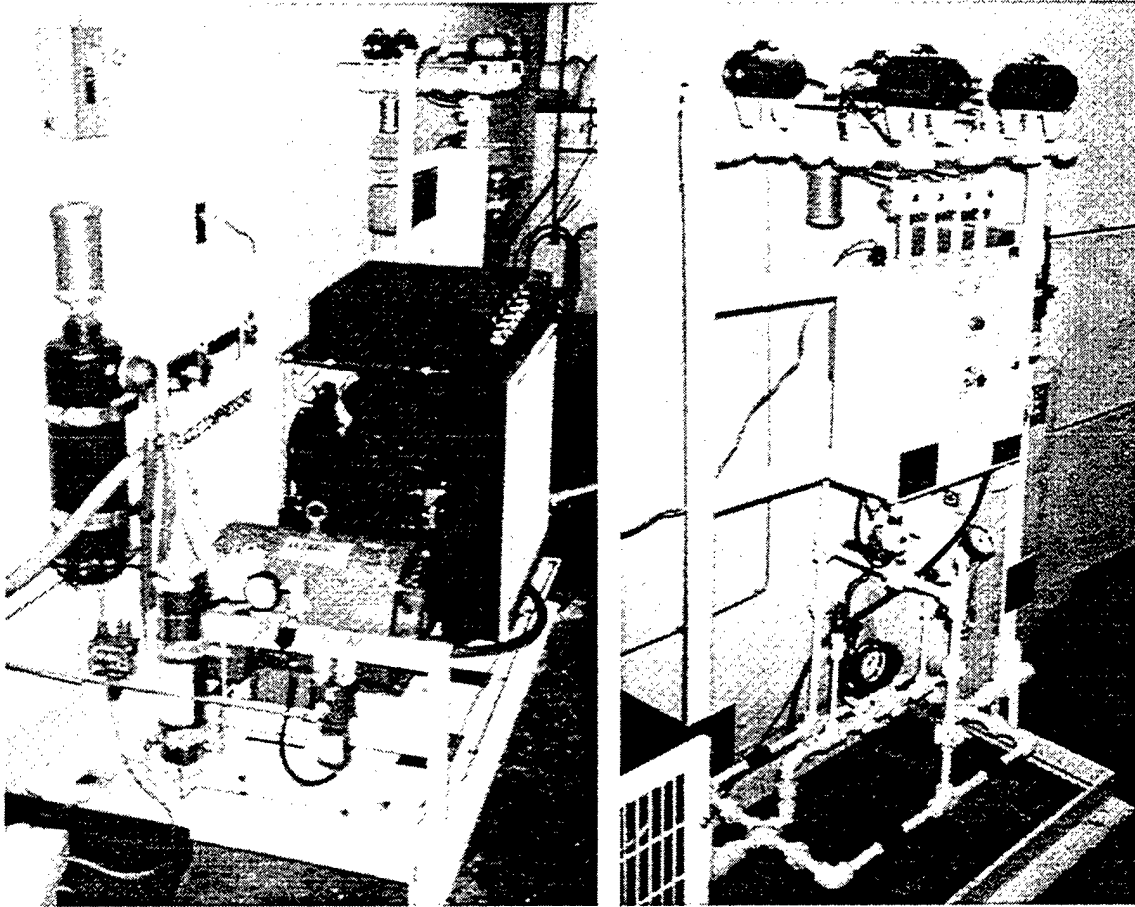


Figure D.2 High pressure air tank.



Style:	High Volume / Dome Regulated 204atm
Regulator:	Grove Powreactor Dome Regulator #200/300
Manufacturer:	Eagle Compressors Inc., Pleasant Garden, NC
Model:	A.C.P. Custom Air Control Panel #G07C0177

Figure D.3 Air control panel.



Style:	air cooled four stage compressor
Power:	30kW
Separator:	mechanical
Dryer:	regenerative
Delivery:	1m ³ /min @ 41atm (free air delivery)
Manufacturer:	Eagle Compressors Inc., Pleasant Garden, NC
Model:	HORIZONTAL 4S50 MKII #HW40HH3

Figure D.4 Compressor and dryer.

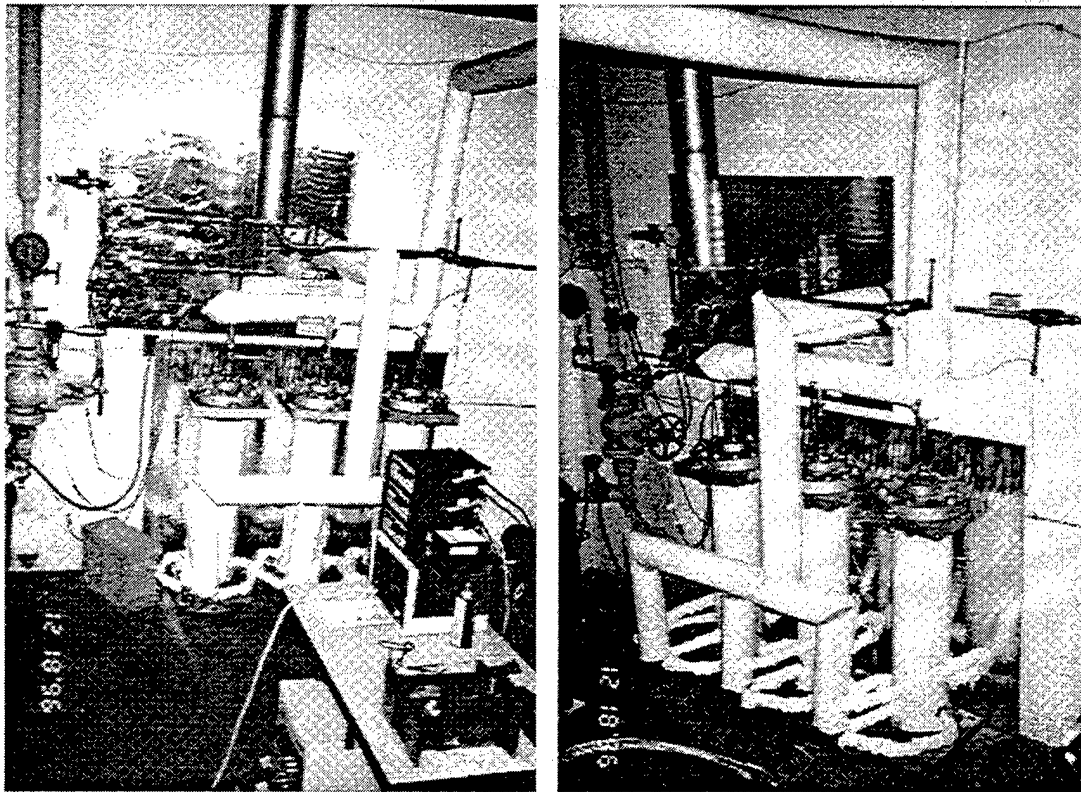


Figure D.5 Mach 5 wind tunnel pebble bed heating system.

The heaters are re-heated by convection with two heavy-duty electric air heaters (Reheat Co. Inc. Model HDA-2-12-2). These heaters each produce a minimum 1.5kW when powered by standard 240 Volt outlets. With both electric heaters in operation, it takes approximately 1 hour to re-heat each pebble-bed heater from an end-of-run temperature back to operating temperature.

D.3 Nozzle & Test Section

The nozzle profile was designed using the method of characteristics with modifications for viscous effects. The test section of the wind tunnel has cross-sectional dimensions of 7.62cm \times 7.62cm and a length of 26.67cm. The test section and nozzle (Figures D.6 and D.7) are milled from 347 stainless steel. The test section side walls are fitted with optical grade glass windows to allow for photographic visualization of the flow (Figure D.8). The tunnel ceiling (Figure D.9) is designed to accept the WAF model, and the floor (Figure D.10) is fitted with slots for probe insertion.

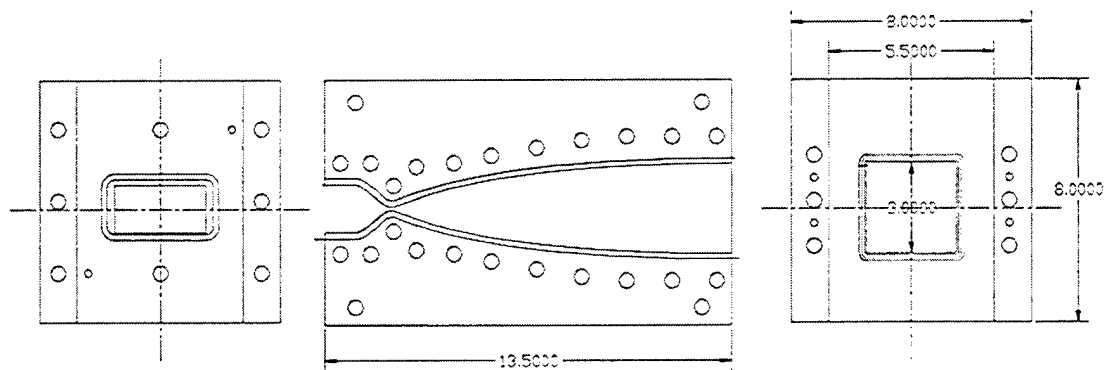
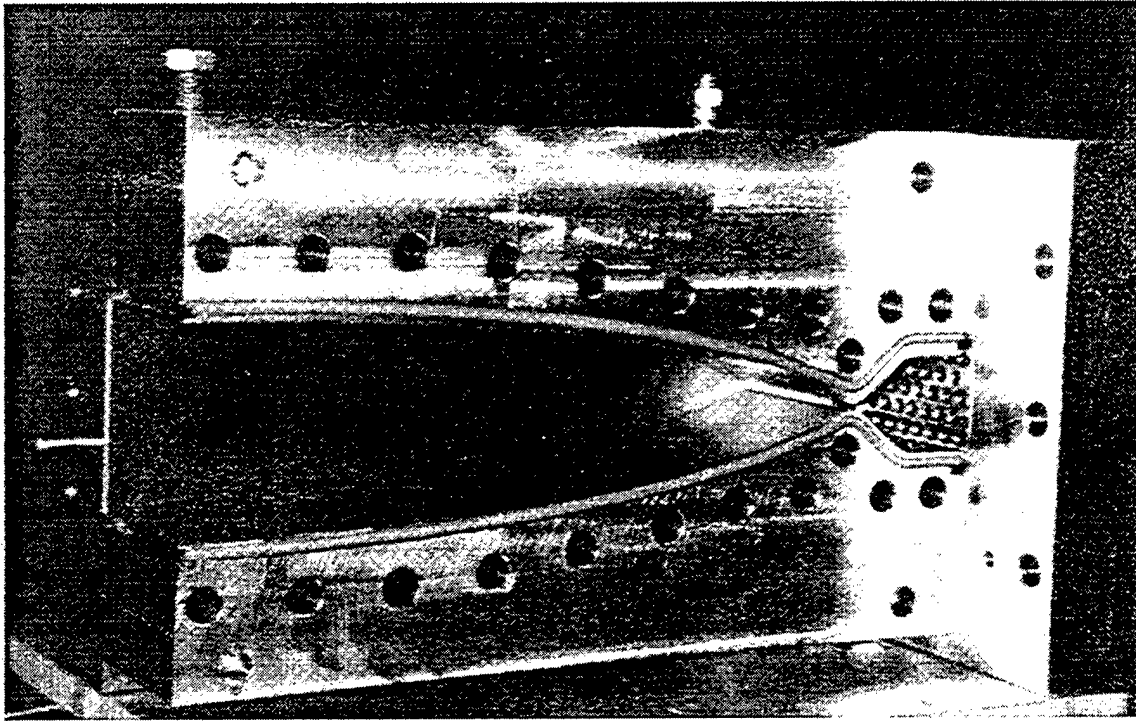


Figure D.6 Wind tunnel nozzle (dimensions in inches).

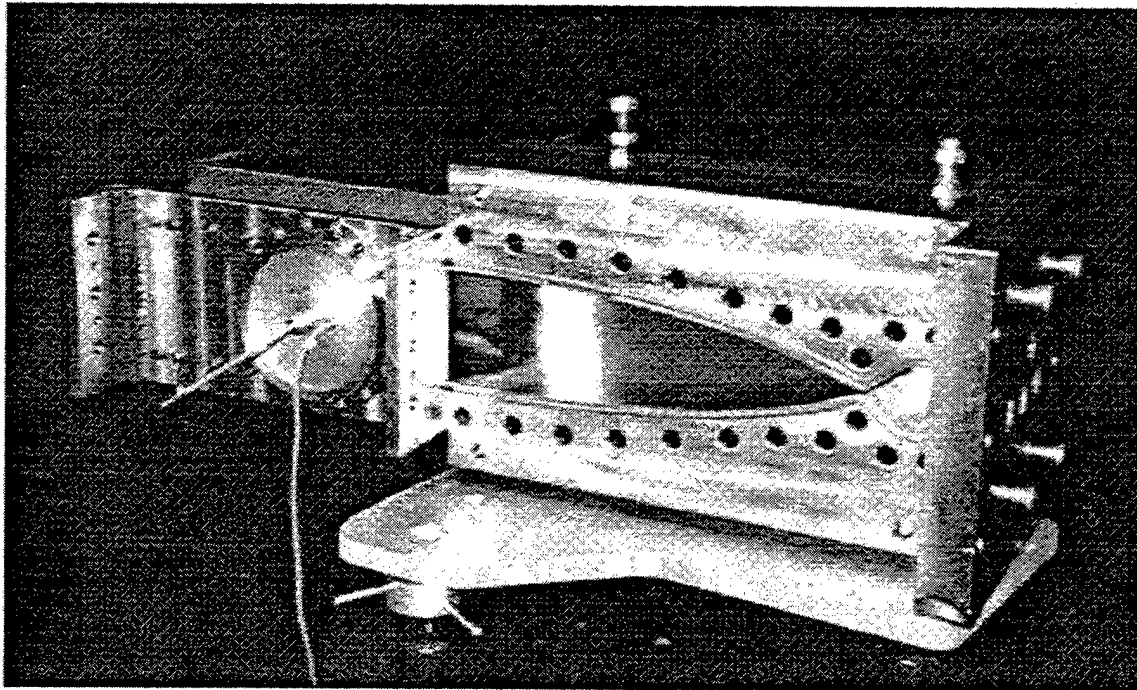


Figure D.7 Wind tunnel nozzle and test section. Shown with nozzle wall removed for visibility and window replaced by aluminum plug for initial tunnel calibration.

D.4 Diffuser & Silencer

An adjustable throat-area diffuser was employed, allowing it to be tuned for optimal performance after the tunnel was assembled. A sound muffler (seen in Figure D.2) which is attached directly to the diffuser exit directs the air back outside the building.

D.5 Plenum Chamber Instrumentation

Instrumentation for the tunnel conditions include an upstream pitot tube and thermocouple well ahead of the throat to measure $P_{t\infty}$ and $T_{t\infty}$. A 34atm Endevco pressure transducer was used to sense plenum pressure, which is displayed and digitized by an Endevco (model 4428A) signal conditioner. Plenum temperature is sensed with an Omega K-type (model KAIN-18-U-12) lance thermocouple, then displayed on an Omega model DP41-TC-A temperature display. This temperature data was used in the data reduction as well as to ensure that the air had been adequately heated. Pressure and temperature is sent to the data acquisition unit (Section 3.6).

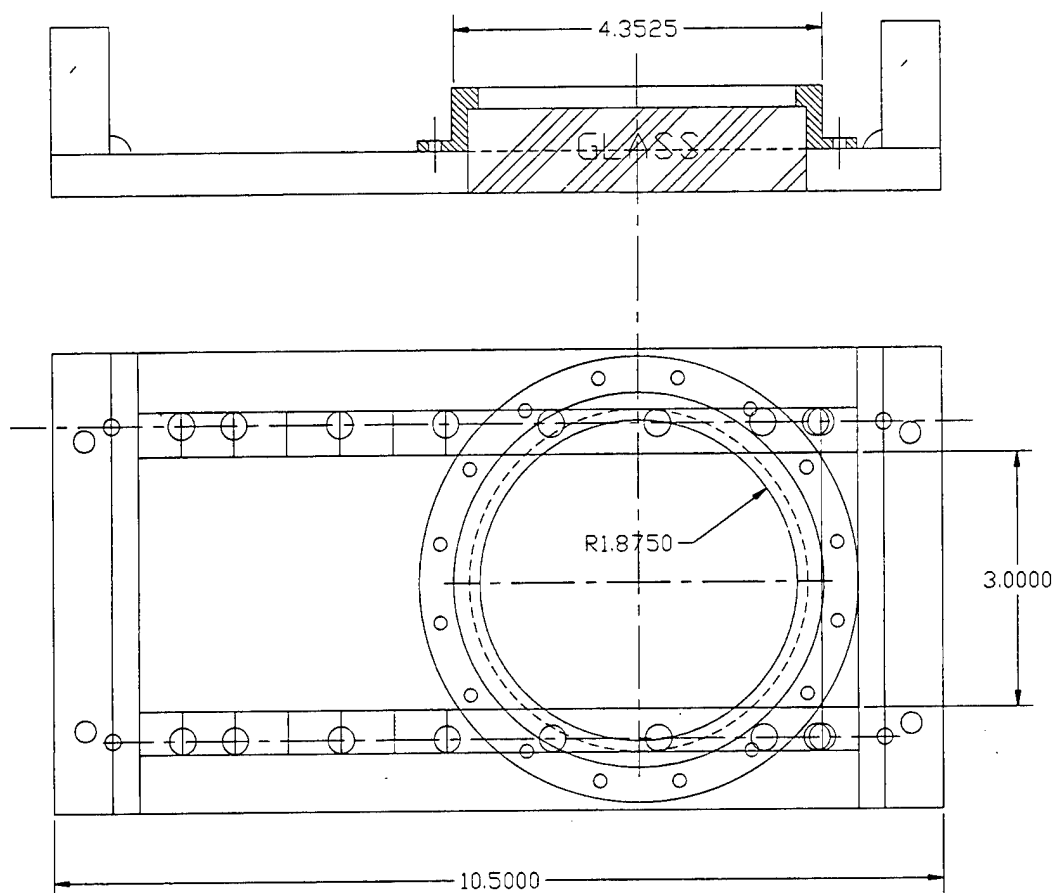


Figure D.8 Wind tunnel test section wall with windows (dimensions in inches).

D.6 TSI 3-DOF Traverse System

A TSI 3-DOF traverse system was used for the Mach 5 experiments. Although this traverse was equipped with its own manual control center, safety concerns dictated that the traverse be controlled from a remote location during tunnel operation. The control software also provides the ability to move specific distances at prescribed speeds.

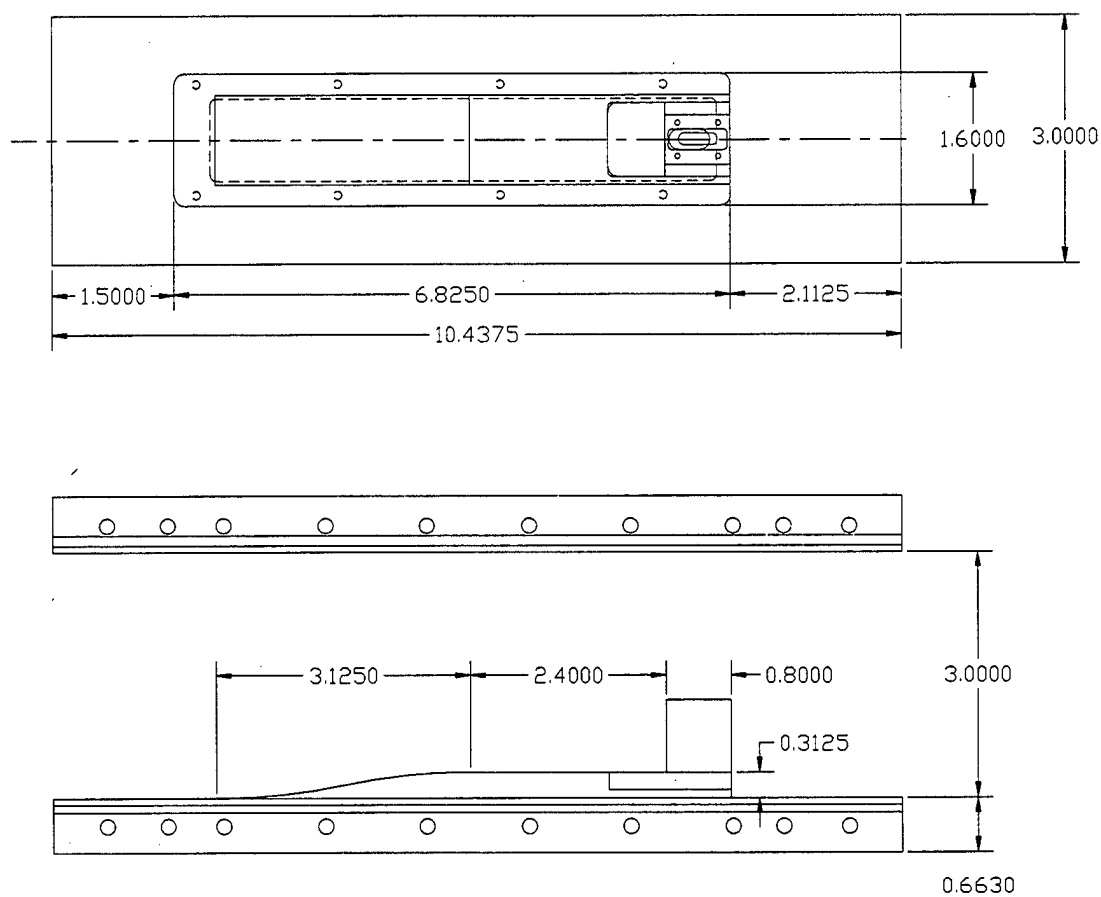


Figure D.9 Wind tunnel ceiling with model insert (dimensions in inches).

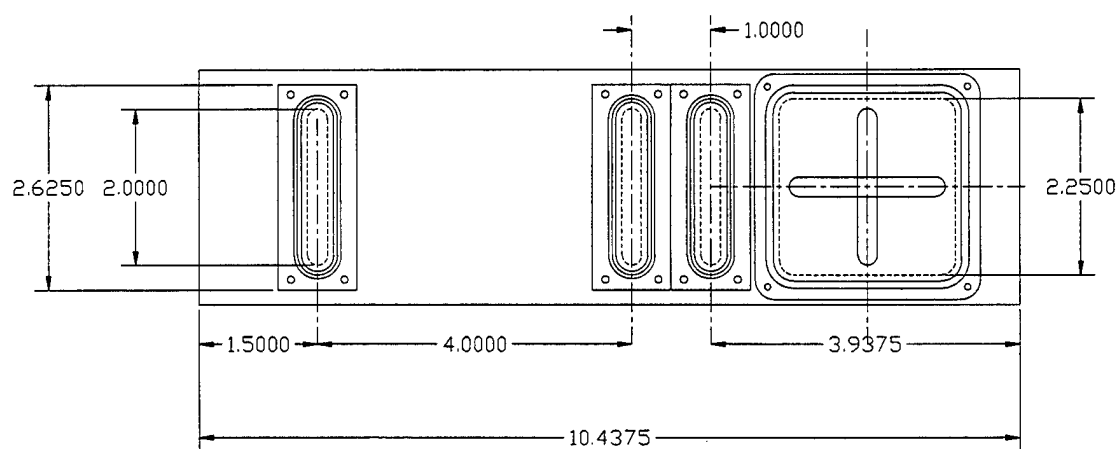


Figure D.10 Wind tunnel floor with probe access (dimensions in inches).

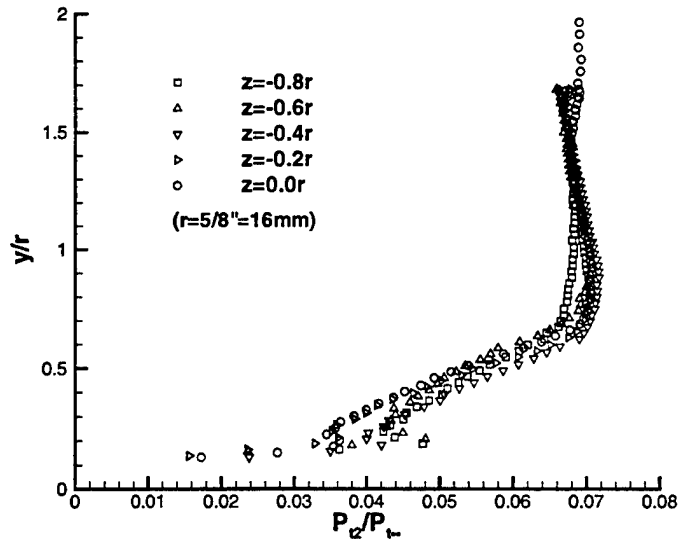


Figure D.11 Measured pitot pressure at upstream location.

D.7 Tunnel Calibration

When operated near the conditions given in Table D.1, the tunnel flow is very two-dimensional over a significant portion of the tunnel width. This is demonstrated in Figure D.11 which shows pitot pressures measured at an upstream ($x = -9.64r = -7.53c$) location over a range of span-wise locations.

D.8 Numerical Validation

The AFIT Mach 5 wind tunnel was simulated numerically to provide some reassurance of the tunnel design, as well as to gain some early experience with the methods used for the wrap-around fin simulations. The simulations were conducted using the General Aerodynamic Simulation Program (GASP) Version 2.0^[72]. The computational requirements of these simulations were also used to estimate the computational requirements of the WAF simulations presented in this document. Several 2-D and 3-D solutions were obtained, the details of which were reported in the Prospectus for this research.^[107]

Appendix E. GASP Input Deck for $M=2.8$ Viscous Simulation

The GASP input deck (version 3.0) for the viscous simulation at Mach 2.8 discussed in Chapter 4 is presented below. As discussed in Chapter 4, a 2-Dimensional inflow boundary condition (shown in Figure E.1) is specified on the upstream edge of the first zone. Parallel flow and constant pressure through the boundary layer was assumed. This two-dimensional PNS region allowed the boundary layer to develop into a fully turbulent profile (also shown in Figure E.1) upstream of the blended body region.

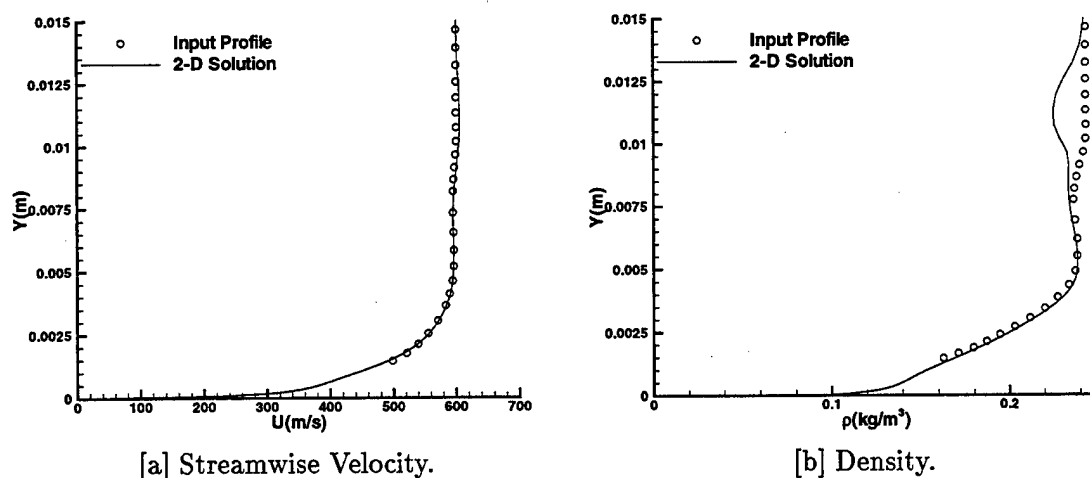


Figure E.1 Space marched zone inflow boundary condition for and exit.

GASP Input Deck: Mach 3 WAF Simulation with Experimental Upstream BC

```

-----
                        FILE INFO
-----
chemModPath      gridDir      solutionDir  bcDir
'../../database/db1.bin'  '.'  '.'  '.'
gridFileMode solnFileMode bcFileMode
      1           1           1
-----

                        GENERAL INFO
-----
iunits      rhoNDim      vNDim      tNDim      lNDim      pGauge
  1      2.039000e-01  6.070000e+02  1.096000e+02  1.000000e+00  0.000000e+00
irest  initByZone  memoryMode  residmode  cpumode
  1      0           1           2           1
nZone  nZonalBoun  nPartStyle  nPhysMod  nBlock  iBlkStt  iBlkEnd
  12      21           1           3           8       8       8
-----

                        ZONE INFO

```

ZONE #1: 2D -- Rectangular Part of Test Section (half)

Initial Conditions

initPhysMod

1

Boundary Conditions

nSurfTypes	i0	id	j0	jd	k0	kd
6	-2	-3	10	-3	-19	-3

twall	pback
294.00	1.431

Mesh Sequencing

nSeqLevel

3

seqNum	initSolFile	intrpQ	ilev	jlev	klev
1	0	0	1	1	1
2	0	0	1	1	1
3	0	0	1	1	1

ZONE #2: Blend from Flat Plate to Cyl Body (half)

Initial Conditions

initPhysMod

1

Boundary Conditions

nSurfTypes	i0	id	j0	jd	k0	kd
6	-20	-3	10	-3	-19	-3

twall	pback
294.00	1.431

Mesh Sequencing

nSeqLevel

3

seqNum	initSolFile	intrpQ	ilev	jlev	klev
1	0	0	1	1	1
2	0	0	1	1	1
3	0	0	1	1	1

ZONE #3: Cylindrical Body

Initial Conditions

initPhysMod

1

Boundary Conditions

nSurfTypes	i0	id	j0	jd	k0	kd
6	-20	-3	10	-3	-3	-3

twall	pback
294.00	1.431

Mesh Sequencing

nSeqLevel

3

seqNum	initSolFile	intrpQ	ilev	jlev	klev
1	0	0	1	1	1
2	0	0	1	1	1
3	0	0	1	1	1

ZONE #4: Blend to fin

Initial Conditions

initPhysMod

1

Boundary Conditions

nSurfTypes i0 id j0 jd k0 kd
6 -20 -3 10 -3 -3 -3

twall pback
294.00 1.431

Mesh Sequencing

nSeqLevel

3

seqNum	initSolFile	intrpQ	ilev	jlev	klev
1	0	0	1	1	1
2	0	0	1	1	1
3	0	0	1	1	1

ZONE #5: Quadrant I -- ahead of fin

Initial Conditions

initPhysMod

3

Boundary Conditions

nSurfTypes i0 id j0 jd k0 kd
6 -20 -20 -20 -3 -20 -3

twall pback
294.00 1.431

Mesh Sequencing

nSeqLevel

3

seqNum	initSolFile	intrpQ	ilev	jlev	klev
1	1	0	1	1	1
2	1	0	2	2	2
3	1	0	4	4	4

ZONE #6: Quadrant II -- ahead of fin

Initial Conditions

initPhysMod

3

Boundary Conditions

nSurfTypes i0 id j0 jd k0 kd
6 -20 -20 -20 -3 -3 -20

twall pback
294.00 1.431

Mesh Sequencing

nSeqLevel

3

seqNum	initSolFile	intrpQ	ilev	jlev	klev
1	1	0	1	1	1
2	1	0	2	2	2
3	1	0	4	4	4

ZONE #7: Fin region - Quadrant I

Initial Conditions

initPhysMod

3

Boundary Conditions

nSurfTypes i0 id j0 jd k0 kd

6 -20 -3 -20 -3 -20 -3

twall pback

294.00 1.431

Mesh Sequencing

nSeqLevel

3

seqNum	initSolFile	intrpQ	ilev	jlev	klev
--------	-------------	--------	------	------	------

1	1	0	1	1	1
---	---	---	---	---	---

2	1	0	2	2	2
---	---	---	---	---	---

3	1	0	4	4	4
---	---	---	---	---	---

ZONE #8: Fin region - Quadrant II

Initial Conditions

initPhysMod

3

Boundary Conditions

nSurfTypes i0 id j0 jd k0 kd

6 -20 -3 -20 -3 -3 -20

twall pback

294.00 1.431

Mesh Sequencing

nSeqLevel

3

seqNum	initSolFile	intrpQ	ilev	jlev	klev
--------	-------------	--------	------	------	------

1	1	0	1	1	1
---	---	---	---	---	---

2	1	0	2	2	2
---	---	---	---	---	---

3	1	0	4	4	4
---	---	---	---	---	---

ZONE #9: Fin region - Quadrant III

Initial Conditions

initPhysMod

3

Boundary Conditions

nSurfTypes i0 id j0 jd k0 kd

6 -20 -3 10 -20 -3 0

twall pback

294.00 1.431

Mesh Sequencing

nSeqLevel

3

seqNum	initSolFile	intrpQ	ilev	jlev	klev
--------	-------------	--------	------	------	------

1	1	0	1	1	1
---	---	---	---	---	---

2	1	0	2	2	2
---	---	---	---	---	---

3	1	0	4	4	4
---	---	---	---	---	---

ZONE #10: Fin region - Quadrant IV

Initial Conditions

initPhysMod

3

Boundary Conditions

nSurfTypes i0 id j0 jd k0 kd

6 -20 -3 10 -20 0 -3

twall pback

294.00 1.431

Mesh Sequencing

nSeqLevel

3

seqNum	initSolFile	intrpQ	ilev	jlev	klev
--------	-------------	--------	------	------	------

1	1	0	1	1	1
---	---	---	---	---	---

2	1	0	2	2	2
---	---	---	---	---	---

3	1	0	4	4	4
---	---	---	---	---	---

ZONE #11: fin tip to top wall

Initial Conditions

initPhysMod

3

Boundary Conditions

nSurfTypes i0 id j0 jd k0 kd

6 -20 -3 10 -3 -20 -20

twall pback

294.00 1.431

Mesh Sequencing

nSeqLevel

3

seqNum	initSolFile	intrpQ	ilev	jlev	klev
--------	-------------	--------	------	------	------

1	1	0	1	1	1
---	---	---	---	---	---

2	1	0	2	2	2
---	---	---	---	---	---

3	1	0	4	4	4
---	---	---	---	---	---

ZONE #12: fin tip to side wall

Initial Conditions

initPhysMod

3

Boundary Conditions

nSurfTypes i0 id j0 jd k0 kd

6 -20 -3 -3 10 -20 -20

twall pback

294.00 1.431

Mesh Sequencing

nSeqLevel

3

seqNum	initSolFile	intrpQ	ilev	jlev	klev
--------	-------------	--------	------	------	------

1	1	0	1	1	1
---	---	---	---	---	---

2	1	0	2	2	2
---	---	---	---	---	---

3	1	0	4	4	4
---	---	---	---	---	---

ZONAL BOUN INFO

ZONAL BOUNDARY #1: -- straight test sect to body blend

izbpass	zbType	zbFluxCrct					
2	1	0					
nz	zbface	zbd1r1	zbstt1	zbend1	zbd1r2	zbstt2	zbend2
1	2	2	1	136	3	1	1
neqn	zmap(1:neqn)						
5	1 2 3 4 5						
nz	zbface	zbd1r1	zbstt1	zbend1	zbd1r2	zbstt2	zbend2
2	1	2	1	136	3	1	96
neqn	zmap(1:neqn)						
5	1 2 3 4 5						

ZONAL BOUNDARY #2: -- body blend to cyl body -- Quad I & IV

izbpass	zbType	zbFluxCrct					
2	0	0					
nz	zbface	zbd1r1	zbstt1	zbend1	zbd1r2	zbstt2	zbend2
2	2	2	1	136	3	1	96
neqn	zmap(1:neqn)						
5	1 2 3 4 5						
nz	zbface	zbd1r1	zbstt1	zbend1	zbd1r2	zbstt2	zbend2
3	1	2	1	136	3	97	192
neqn	zmap(1:neqn)						
5	1 2 3 4 5						

ZONAL BOUNDARY #3: -- body blend to cyl body -- Quad II & III

izbpass	zbType	zbFluxCrct					
2	0	0					
nz	zbface	zbd1r1	zbstt1	zbend1	zbd1r2	zbstt2	zbend2
2	2	2	1	136	3	1	96
neqn	zmap(1:neqn)						
5	1 2 3 4 5						
nz	zbface	zbd1r1	zbstt1	zbend1	zbd1r2	zbstt2	zbend2
3	1	2	1	136	3	96	1
neqn	zmap(1:neqn)						
5	1 2 3 -4 5 (NOTE: zbmab2 -4 requires GASP mod.)						

ZONAL BOUNDARY #4: -- cyl body to body-to-fin transition zone

izbpass	zbType	zbFluxCrct					
2	0	0					
nz	zbface	zbd1r1	zbstt1	zbend1	zbd1r2	zbstt2	zbend2
3	2	2	1	136	3	1	192
neqn	zmap(1:neqn)						
5	1 2 3 4 5						
nz	zbface	zbd1r1	zbstt1	zbend1	zbd1r2	zbstt2	zbend2
4	1	2	1	136	3	1	192
neqn	zmap(1:neqn)						
5	1 2 3 4 5						

ZONAL BOUNDARY #5: -- Quadrant I of Zone 4 to Zone 5

izbpass	zbType	zbFluxCrct					
2	1	0					
nz	zbface	zbd1r1	zbstt1	zbend1	zbd1r2	zbstt2	zbend2
4	2	2	97	136	3	97	192
neqn	zbmap(1:neqn)						
5	1 2 3 4 5						
nz	zbface	zbd1r1	zbstt1	zbend1	zbd1r2	zbstt2	zbend2
5	1	2	1	40	3	1	96
neqn	zbmap(1:neqn)						
5	1 2 3 4 5						

ZONAL BOUNDARY #6: -- Quadrant II of Zone 4 to Zone 6

izbpass	zbType	zbFluxCrct					
2	1	0					
nz	zbface	zbd1r1	zbstt1	zbend1	zbd1r2	zbstt2	zbend2
4	2	2	97	136	3	1	96
neqn	zbmap(1:neqn)						
5	1 2 3 4 5						
nz	zbface	zbd1r1	zbstt1	zbend1	zbd1r2	zbstt2	zbend2
6	1	2	1	40	3	1	96
neqn	zbmap(1:neqn)						
5	1 2 3 4 5						

ZONAL BOUNDARY #7: -- Quadrant III of Zone 4 to Zone 9

izbpass	zbType	zbFluxCrct					
2	1	0					
nz	zbface	zbd1r1	zbstt1	zbend1	zbd1r2	zbstt2	zbend2
4	2	2	1	96	3	1	96
neqn	zbmap(1:neqn)						
5	1 2 3 4 5						
nz	zbface	zbd1r1	zbstt1	zbend1	zbd1r2	zbstt2	zbend2
9	1	2	1	96	3	1	96
neqn	zbmap(1:neqn)						
5	1 2 3 4 5						

ZONAL BOUNDARY #8: -- Quadrant IV of Zone 4 to Zone 10

izbpass	zbType	zbFluxCrct					
2	1	0					
nz	zbface	zbd1r1	zbstt1	zbend1	zbd1r2	zbstt2	zbend2
4	2	2	1	96	3	97	192
neqn	zbmap(1:neqn)						
5	1 2 3 4 5						
nz	zbface	zbd1r1	zbstt1	zbend1	zbd1r2	zbstt2	zbend2
10	1	2	1	96	3	1	96
neqn	zbmap(1:neqn)						
5	1 2 3 4 5						

ZONAL BOUNDARY #9: -- Zone 5 to Zone 6

izbpass	zbType	zbFluxCrct
0	0	0

nz	zbfac	zbd1r	zbstt1	zbend1	zbd1r2	zbstt2	zbend2
5	5	1	1	72	2	1	40
neqn		zmap(1:neqn)					
5		1	2	3	4	5	
nz	zbfac	zbd1r	zbstt1	zbend1	zbd1r2	zbstt2	zbend2
6	6	1	1	72	2	1	40
neqn		zmap(1:neqn)					
5		1	2	3	4	5	

ZONAL BOUNDARY #10: -- Zone 6 to top of front of Zone 9

izbpass	zbType	zbFluxCrct					
0	0	0					
nz	zbfac	zbd1r	zbstt1	zbend1	zbd1r2	zbstt2	zbend2
6	3	1	1	72	3	1	96
neqn		zmap(1:neqn)					
5		1	2	3	4	5	
nz	zbfac	zbd1r	zbstt1	zbend1	zbd1r2	zbstt2	zbend2
9	4	1	1	72	3	1	96
neqn		zmap(1:neqn)					
5		1	2	3	4	5	

ZONAL BOUNDARY #11: -- Zone 9 to Zone 10 (extends forward from l.e.)

izbpass	zbType	zbFluxCrct					
0	0	0					
nz	zbfac	zbd1r	zbstt1	zbend1	zbd1r2	zbstt2	zbend2
10	5	1	1	72	2	1	96
neqn		zmap(1:neqn)					
5		1	2	3	4	5	
nz	zbfac	zbd1r	zbstt1	zbend1	zbd1r2	zbstt2	zbend2
9	6	1	1	72	2	1	96
neqn		zmap(1:neqn)					
5		1	2	3	4	5	

ZONAL BOUNDARY #12: -- Zone 5 to top of front of Zone 10

izbpass	zbType	zbFluxCrct					
0	0	0					
nz	zbfac	zbd1r	zbstt1	zbend1	zbd1r2	zbstt2	zbend2
5	3	1	1	72	3	1	96
neqn		zmap(1:neqn)					
5		1	2	3	4	5	
nz	zbfac	zbd1r	zbstt1	zbend1	zbd1r2	zbstt2	zbend2
10	4	1	1	72	3	1	96
neqn		zmap(1:neqn)					
5		1	2	3	4	5	

ZONAL BOUNDARY #13: -- Zone 5 to Zone 7

izbpass	zbType	zbFluxCrct					
0	0	0					
nz	zbfac	zbd1r	zbstt1	zbend1	zbd1r2	zbstt2	zbend2
5	2	2	1	40	3	1	96
neqn		zmap(1:neqn)					

5		1	2	3	4	5		
nz	zbfac	zbd1r	zbstt1	zbend1	zbd2r	zbstt2	zbend2	
7	1	2	1	40	3	1	96	
neqn	zmap(1:neqn)							
5		1	2	3	4	5		

ZONAL BOUNDARY #14: -- Zone 6 to Zone 8

izbpass	zbType	zbFluxCrct						
0	0	0						
nz	zbfac	zbd1r	zbstt1	zbend1	zbd2r	zbstt2	zbend2	
6	2	2	1	40	3	1	96	
neqn	zmap(1:neqn)							
5		1	2	3	4	5		
nz	zbfac	zbd1r	zbstt1	zbend1	zbd2r	zbstt2	zbend2	
8	1	2	1	40	3	1	96	
neqn	zmap(1:neqn)							
5		1	2	3	4	5		

ZONAL BOUNDARY #15: -- Zone 7 to back of Zone 10

izbpass	zbType	zbFluxCrct						
0	0	0						
nz	zbfac	zbd1r	zbstt1	zbend1	zbd2r	zbstt2	zbend2	
7	3	1	1	84	3	1	96	
neqn	zmap(1:neqn)							
5		1	2	3	4	5		
nz	zbfac	zbd1r	zbstt1	zbend1	zbd2r	zbstt2	zbend2	
10	4	1	73	156	3	1	96	
neqn	zmap(1:neqn)							
5		1	2	3	4	5		

ZONAL BOUNDARY #16: -- (Q1) to Fin-to-Top Zone -- LE

izbpass	zbType	zbFluxCrct						
0	0	0						
nz	zbfac	zbd1r	zbstt1	zbend1	zbd2r	zbstt2	zbend2	
7	5	1	1	20	2	1	40	
neqn	zmap(1:neqn)							
5		1	2	3	4	5		
nz	zbfac	zbd1r	zbstt1	zbend1	zbd2r	zbstt2	zbend2	
11	1	3	1	20	2	1	40	
neqn	zmap(1:neqn)							
5		1	2	3	4	5		

ZONAL BOUNDARY #17: -- (Q1) to Fin-to-Top Zone -- Side

izbpass	zbType	zbFluxCrct						
0	0	0						
nz	zbfac	zbd1r	zbstt1	zbend1	zbd2r	zbstt2	zbend2	
7	5	1	21	84	2	1	40	
neqn	zmap(1:neqn)							
5		1	2	3	4	5		
nz	zbfac	zbd1r	zbstt1	zbend1	zbd2r	zbstt2	zbend2	
11	6	1	1	64	2	1	40	

```

neqn          zbmap(1:neqn)
  5            1  2  3  4  5
-----
ZONAL BOUNDARY #18: -- (Q2) to Fin-to-Top Zone
izbpass      zbType      zbFluxCrct
  0            0            0
nz  zbfac     zbdire     zbstd     zbend     zbdire     zbstd     zbend
  8   6         1         1         64         2         1         40
neqn          zbmap(1:neqn)
  5            1  2  3  4  5
nz  zbfac     zbdire     zbstd     zbend     zbdire     zbstd     zbend
11   5         1         1         64         2         1         40
neqn          zbmap(1:neqn)
  5            1  2  3  4  5
-----
ZONAL BOUNDARY #19: -- (Q3) to Fin-to-Side Zone -- LE
izbpass      zbType      zbFluxCrct
  0            0            0
nz  zbfac     zbdire     zbstd     zbend     zbdire     zbstd     zbend
  9   4         1         73         92         3         1         96
neqn          zbmap(1:neqn)
  5            1  2  3  4  5
nz  zbfac     zbdire     zbstd     zbend     zbdire     zbstd     zbend
12   1         3         1         20         2         1         96
neqn          zbmap(1:neqn)
  5            1  2  3  4  5
-----
ZONAL BOUNDARY #20: -- (Q3) to Fin-to-Side Zone -- Side
izbpass      zbType      zbFluxCrct
  0            0            0
nz  zbfac     zbdire     zbstd     zbend     zbdire     zbstd     zbend
  9   4         1         93         156         3         1         96
neqn          zbmap(1:neqn)
  5            1  2  3  4  5
nz  zbfac     zbdire     zbstd     zbend     zbdire     zbstd     zbend
12   6         1         1         64         2         1         96
neqn          zbmap(1:neqn)
  5            1  2  3  4  5
-----
ZONAL BOUNDARY #21: -- (Q2) to Fin-to-Side Zone
izbpass      zbType      zbFluxCrct
  0            0            0
nz  zbfac     zbdire     zbstd     zbend     zbdire     zbstd     zbend
  8   3         1         1         64         3         1         96
neqn          zbmap(1:neqn)
  5            1  2  3  4  5
nz  zbfac     zbdire     zbstd     zbend     zbdire     zbstd     zbend
12   5         1         1         64         2         1         96
neqn          zbmap(1:neqn)
  5            1  2  3  4  5
-----

```

PARTITION STYLES

PARTITION STYLE #1:

nDir

1

dir numPart

1 1

PHYSICAL MODELING INFO

PHYSICAL MODEL #1: PNS x-marching, Viscous - B-L

CHEMISTRY & THERMODYNAMICS

nspec	nnev	prefDiss	vibRelax	itherm	chemmod	ieq
1	0	0	0	4	'Perfect Gas'	1

INVISCID FLUXES

imarch

1

invflxi invflxj invflxk

4 3 3

rkapi rkapij rkapik sdm2 sdm4

-1.0000 0.3333 0.3333 0.0000 0.0000

limi limj link rk_ven

2 2 2 1.000

VISCOUS FLUXES

isViscous

2

visflxi visflxj visflxk

0 -1 -1

modlmu modlk imodld ivac

2 2 1 2

prl prt scl sct

0.72 0.90 1.00 0.50

ikeps kemin wallfunc igb

0 0 0 0

INITIAL CONDITIONS

icond

2

Vel/Mach	cx	cy	cz	temp/press	turbi	tkelref
2.9	1	0	0	109.6	0.01	0.001

rho_spec

0.2039

REFERENCE STATE FOR B.C.'s

```

-----
icond
  2
Vel/Mach      cx      cy      cz      temp/press  turbi  tkelref
    2.9        1      0      0      109.6      0.01   0.001
rho_spec
0.2039

```

```

*****
PHYSICAL MODEL #2: RANS, Viscous - Laminar, 3rd order
-----

```

CHEMISTRY & THERMODYNAMICS

```

-----
nspec  nnev  prefDiss  vibRelax  itherm  chemmod  ieq
  1      0      0      0      4      'Perfect Gas'  1
-----

```

INVISCID FLUXES

```

-----
imarch
  0
invflxi  invflxj  invflxk
  2      2      2
rkapi    rkapij   rkapk    sdm2     sdm4
0.3333   0.3333   0.3333   0.0000   0.0000
limi     limj     limk     rk_ven
  2      2      2      1.000
-----

```

VISCOUS FLUXES

```

-----
isViscous
  1
visflxi  visflxj  visflxk
  -1      -1      -1
modlmu   modlk   imodld   ivac
  2      2      1      2
prl      prt     scl      sct
0.72     0.90    1.00    0.50
ikeps    kemin   wallfunc  igb
  0      0      0      0
-----

```

INITIAL CONDITIONS

```

-----
icond
  2
Vel/Mach      cx      cy      cz      temp/press  turbi  tkelref
    2.9        1      0      0      109.6      0.01   0.001
rho_spec
0.2039
-----

```

REFERENCE STATE FOR B.C.'s

```

-----
icond

```



```

2
Vel/Mach      cx      cy      cz      temp/press  turbi  tkelref
2.9          1       0       0       109.6      0.01   0.001

```

```

rho_spec
0.2039

```

```

*****

```

```

PHYSICAL MODEL #3: RANS, Viscous - B-L, 3rd order

```

CHEMISTRY & THERMODYNAMICS

```

nspec  nnev  prefDiss  vibRelax  itherm      chemmod      ieq
1       0       0         0         4      'Perfect Gas'  1

```

INVISCID FLUXES

```

imarch
0
invflxi  invflxj  invflxk
2         2         2
rkapi    rkapi    rkapi    sdm2    sdm4
0.3333   0.3333   0.3333   0.0000  0.0000
limi     limj     limk     rk_ven
2        2        2        1.000

```

VISCOUS FLUXES

```

isViscous
2
visflxi  visflxj  visflxk
-1        -1        -1
modlmnu  modlk    imodld  ivac
2         2         1         2
prl       prt      scl      sct
0.72     0.90     1.00     0.50
ikeps     kemin    wallfunc  igb
0         0         0         0

```

INITIAL CONDITIONS

```

icond
2
Vel/Mach      cx      cy      cz      temp/press  turbi  tkelref
2.9          1       0       0       109.6      0.01   0.001
rho_spec
0.2039

```

REFERENCE STATE FOR B.C.'s

```

icond
2
Vel/Mach      cx      cy      cz      temp/press  turbi  tkelref

```

2.9 1 0 0 109.6 0.01 0.001
rho_spec
0.2039

BLOCK INFO

BLOCK #1: march through zone 1 -- (starting at experimental zb) (1-60)

imcont	nswp	ncycle	nwres	mstage	rtolr	rtola		
1	1	250	50	1	1.00e-03	1.00e-10		
mgstyle	nitfine	nitcrct	nitsmth	smthfac	dtfac			
0	1	1	0	3.00e-01	1.00e+00			
SWEEP #1: march through zone 3								
nz	iseq	npm	partStyle	iswkdir	iplstt	iplend		
1	3	1	1	1	1	60		
impl	itmstep	keslv	ichemslv	nplane	inner	mxin	tolin	
2	1	1	1	1	0	5	0.01	
dtmin	dtmax	irelu	nremax	tolreu				
-1.00e+00	-1.00e+00	1	10	1.00e-01				

BLOCK #2: march through zone 2 (1-100)

imcont	nswp	ncycle	nwres	mstage	rtolr	rtola		
1	1	250	50	1	1.00e-03	1.00e-10		
mgstyle	nitfine	nitcrct	nitsmth	smthfac	dtfac			
0	1	1	0	3.00e-01	1.00e+00			
SWEEP #1: march through zone 4								
nz	iseq	npm	partStyle	iswkdir	iplstt	iplend		
2	3	1	1	1	1	100		
impl	itmstep	keslv	ichemslv	nplane	inner	mxin	tolin	
2	1	1	1	1	0	5	0.01	
dtmin	dtmax	irelu	nremax	tolreu				
-1.00e+00	-1.00e+00	1	10	1.00e-01				

BLOCK #3: march through zone 3 (1-80)

imcont	nswp	ncycle	nwres	mstage	rtolr	rtola		
1	1	250	50	1	1.00e-03	1.00e-10		
mgstyle	nitfine	nitcrct	nitsmth	smthfac	dtfac			
0	1	1	0	3.00e-01	1.00e+00			
SWEEP #1: march through zone 5								
nz	iseq	npm	partStyle	iswkdir	iplstt	iplend		
3	3	1	1	1	1	80		
impl	itmstep	keslv	ichemslv	nplane	inner	mxin	tolin	
2	1	1	1	1	0	5	0.01	
dtmin	dtmax	irelu	nremax	tolreu				
-1.00e+00	-1.00e+00	1	10	1.00e-01				

BLOCK #4: march through zone 4

imcont	nswp	ncycle	nwres	mstage	rtolr	rtola		
1	1	250	50	1	1.00e-03	1.00e-10		
mgstyle	nitfine	nitcrct	nitsmth	smthfac	dtfac			
0	1	1	0	3.00e-01	1.00e+00			
SWEEP #1: march through zone 6								

nz	iseq	npm	partStyle	iswkdir	iplstt	iplend		
4	3	1	1	1	1	24		
impl	itmstep	keslv	ichemslv	nplane	inner	mxin	tolin	
2	1	1	1	1	0	5	0.01	
dtmin	dtmax	irelu	nremax	tolreu				
-5.00e-01	-5.00e-01	1	10	1.00e-01				

BLOCK #5: global by fin - Laminar - sequence 3

imcont	nswp	ncycle	nwres	mstage	rtolr	rtola		
0	8	2000	100	1	1.00e-04	1.00e-10		
mgstyle	nitfine	nitcrct	nitsmth	smthfac	dtfac			
0	1	1	0	3.00e-01	1.00e+00			

SWEEP #1:

nz	iseq	npm	partStyle	iswkdir	iplstt	iplend		
10	3	2	1	2	1	96		
impl	itmstep	keslv	ichemslv	nplane	inner	mxin	tolin	
4	1	1	1	1	1	5	0.01	
dtmin	dtmax	irelu	nremax	tolreu				
-1.00e-00	-1.00e-00	0	10	1.00e-01				

SWEEP #2:

nz	iseq	npm	partStyle	iswkdir	iplstt	iplend		
9	3	2	1	2	1	96		
impl	itmstep	keslv	ichemslv	nplane	inner	mxin	tolin	
4	1	1	1	1	1	5	0.01	
dtmin	dtmax	irelu	nremax	tolreu				
-1.00e-00	-1.00e-00	0	10	1.00e-01				

SWEEP #3:

nz	iseq	npm	partStyle	iswkdir	iplstt	iplend		
5	3	2	1	2	1	40		
impl	itmstep	keslv	ichemslv	nplane	inner	mxin	tolin	
4	1	1	1	1	1	5	0.01	
dtmin	dtmax	irelu	nremax	tolreu				
-1.00e-00	-1.00e-00	0	10	1.00e-01				

SWEEP #4:

nz	iseq	npm	partStyle	iswkdir	iplstt	iplend		
6	3	2	1	2	1	40		
impl	itmstep	keslv	ichemslv	nplane	inner	mxin	tolin	
4	1	1	1	1	1	5	0.01	
dtmin	dtmax	irelu	nremax	tolreu				
-1.00e-00	-1.00e-00	0	10	1.00e-01				

SWEEP #5:

nz	iseq	npm	partStyle	iswkdir	iplstt	iplend		
7	3	2	1	2	1	40		
impl	itmstep	keslv	ichemslv	nplane	inner	mxin	tolin	
4	1	1	1	1	1	5	0.01	
dtmin	dtmax	irelu	nremax	tolreu				
-1.00e-00	-1.00e-00	0	10	1.00e-01				

SWEEP #6:

nz	iseq	npm	partStyle	iswkdir	iplstt	iplend		
8	3	2	1	2	1	40		
impl	itmstep	keslv	ichemslv	nplane	inner	mxin	tolin	

4	1	1	1	1	1	5	0.01
dtmin	dtmax	irelu	nremax	tolreu			
-1.00e-00	-1.00e-00	0	10	1.00e-01			
SWEEP #7:							
nz	iseq	npm	partStyle	iswpdir	iplstt	iplend	
11	3	2	1	3	1	20	
impl	itmstep	keslv	ichemslv	nplane	inner	mxin	tolin
4	1	1	1	1	1	5	0.01
dtmin	dtmax	irelu	nremax	tolreu			
-1.00e-00	-1.00e-00	0	10	1.00e-01			
SWEEP #8:							
nz	iseq	npm	partStyle	iswpdir	iplstt	iplend	
12	3	2	1	3	1	20	
impl	itmstep	keslv	ichemslv	nplane	inner	mxin	tolin
4	1	1	1	1	1	5	0.01
dtmin	dtmax	irelu	nremax	tolreu			
-1.00e-00	-1.00e-00	0	10	1.00e-01			

BLOCK #6: global by fin - Laminar - sequence 2

imcont	nswp	ncycle	nwres	mstage	rtolr	rtola	
0	8	3000	100	1	1.00e-04	1.00e-10	
mgstyle	nitfine	nitcrct	nitsmth	smthfac	dtfac		
0	1	1	0	3.00e-01	1.00e+00		
SWEEP #1:							
nz	iseq	npm	partStyle	iswpdir	iplstt	iplend	
10	2	2	1	2	1	96	
impl	itmstep	keslv	ichemslv	nplane	inner	mxin	tolin
4	1	1	1	1	1	5	0.01
dtmin	dtmax	irelu	nremax	tolreu			
-1.00e-00	-1.00e-00	0	10	1.00e-01			
SWEEP #2:							
nz	iseq	npm	partStyle	iswpdir	iplstt	iplend	
9	2	2	1	2	1	96	
impl	itmstep	keslv	ichemslv	nplane	inner	mxin	tolin
4	1	1	1	1	1	5	0.01
dtmin	dtmax	irelu	nremax	tolreu			
-1.00e-00	-1.00e-00	0	10	1.00e-01			
SWEEP #3:							
nz	iseq	npm	partStyle	iswpdir	iplstt	iplend	
5	2	2	1	2	1	40	
impl	itmstep	keslv	ichemslv	nplane	inner	mxin	tolin
4	1	1	1	1	1	5	0.01
dtmin	dtmax	irelu	nremax	tolreu			
-1.00e-00	-1.00e-00	0	10	1.00e-01			
SWEEP #4:							
nz	iseq	npm	partStyle	iswpdir	iplstt	iplend	
6	2	2	1	2	1	40	
impl	itmstep	keslv	ichemslv	nplane	inner	mxin	tolin
4	1	1	1	1	1	5	0.01
dtmin	dtmax	irelu	nremax	tolreu			
-1.00e-00	-1.00e-00	0	10	1.00e-01			

```

SWEEP #5:
nz   iseq   npm   partStyle iswkdir   iplstt   iplend
 7    2     2     1         2         1     40
impl itmstep keslv ichemslv nplane   inner   mxin   tolin
 4     1     1     1         1         1     5     0.01
dtmin      dtmax      irelu   nremax      tolreu
-1.00e-00 -1.00e-00    0       10       1.00e-01
SWEEP #6:
nz   iseq   npm   partStyle iswkdir   iplstt   iplend
 8    2     2     1         2         1     40
impl itmstep keslv ichemslv nplane   inner   mxin   tolin
 4     1     1     1         1         1     5     0.01
dtmin      dtmax      irelu   nremax      tolreu
-1.00e-00 -1.00e-00    0       10       1.00e-01
SWEEP #7:
nz   iseq   npm   partStyle iswkdir   iplstt   iplend
11    2     2     1         3         1     20
impl itmstep keslv ichemslv nplane   inner   mxin   tolin
 4     1     1     1         1         1     5     0.01
dtmin      dtmax      irelu   nremax      tolreu
-1.00e-00 -1.00e-00    0       10       1.00e-01
SWEEP #8:
nz   iseq   npm   partStyle iswkdir   iplstt   iplend
12    2     2     1         3         1     20
impl itmstep keslv ichemslv nplane   inner   mxin   tolin
 4     1     1     1         1         1     5     0.01
dtmin      dtmax      irelu   nremax      tolreu
-1.00e-00 -1.00e-00    0       10       1.00e-01

```

BLOCK #7: global by fin - Laminar - sequence 1

```

imcont  nswp  ncycle  nwres  mstage  rtolr  rtola
 0       8    4000    100    1       1.00e-03 1.00e-10
mgstyle nitfine nitrcrt nitsmth smthfac dtfac
 0       1     1     0       3.00e-01 1.00e+00
SWEEP #1:
nz   iseq   npm   partStyle iswkdir   iplstt   iplend
10    1     2     1         2         1     96
impl itmstep keslv ichemslv nplane   inner   mxin   tolin
 4     1     1     1         1         1     5     0.01
dtmin      dtmax      irelu   nremax      tolreu
-1.00e-00 -1.00e-00    0       10       1.00e-01
SWEEP #2:
nz   iseq   npm   partStyle iswkdir   iplstt   iplend
 9    1     2     1         2         1     96
impl itmstep keslv ichemslv nplane   inner   mxin   tolin
 4     1     1     1         1         1     5     0.01
dtmin      dtmax      irelu   nremax      tolreu
-1.00e-00 -1.00e-00    0       10       1.00e-01
SWEEP #3:
nz   iseq   npm   partStyle iswkdir   iplstt   iplend
 5    1     2     1         2         1     40

```

```

impl  itmstep  keslv  ichemslv  nplane  inner  mxin  tolin
  4      1      1      1      1      1      5      0.01
dtmin      dtmax      irelu  nremax      tolreu
-1.00e-00  -1.00e-00      0      10      1.00e-01
SWEEP #4:
nz  iseq  npm  partStyle  iswkdir  iplstt  iplend
  6      1      2      1      2      1      40
impl  itmstep  keslv  ichemslv  nplane  inner  mxin  tolin
  4      1      1      1      1      1      5      0.01
dtmin      dtmax      irelu  nremax      tolreu
-1.00e-00  -1.00e-00      0      10      1.00e-01
SWEEP #5:
nz  iseq  npm  partStyle  iswkdir  iplstt  iplend
  7      1      2      1      2      1      40
impl  itmstep  keslv  ichemslv  nplane  inner  mxin  tolin
  4      1      1      1      1      1      5      0.01
dtmin      dtmax      irelu  nremax      tolreu
-1.00e-00  -1.00e-00      0      10      1.00e-01
SWEEP #6:
nz  iseq  npm  partStyle  iswkdir  iplstt  iplend
  8      1      2      1      2      1      40
impl  itmstep  keslv  ichemslv  nplane  inner  mxin  tolin
  4      1      1      1      1      1      5      0.01
dtmin      dtmax      irelu  nremax      tolreu
-1.00e-00  -1.00e-00      0      10      1.00e-01
SWEEP #7:
nz  iseq  npm  partStyle  iswkdir  iplstt  iplend
 11      1      2      1      3      1      20
impl  itmstep  keslv  ichemslv  nplane  inner  mxin  tolin
  4      1      1      1      1      1      5      0.01
dtmin      dtmax      irelu  nremax      tolreu
-1.00e-00  -1.00e-00      0      10      1.00e-01
SWEEP #8:
nz  iseq  npm  partStyle  iswkdir  iplstt  iplend
 12      1      2      1      3      1      20
impl  itmstep  keslv  ichemslv  nplane  inner  mxin  tolin
  4      1      1      1      1      1      5      0.01
dtmin      dtmax      irelu  nremax      tolreu
-1.00e-00  -1.00e-00      0      10      1.00e-01

```

BLOCK #7: global by fin - Turbulent B-L - sequence 1

```

imcont  nswp  ncycle  nwres  mstage  rtolr  rtola
  0      8      5000      100      1      1.00e-03  1.00e-10
mgstyle  nitfine  nitcrct  nitsmth  smthfac  dtfac
  0      1      1      0      3.00e-01  1.00e+00
SWEEP #1:
nz  iseq  npm  partStyle  iswkdir  iplstt  iplend
 10      1      3      1      2      1      96
impl  itmstep  keslv  ichemslv  nplane  inner  mxin  tolin
  4      1      1      1      1      1      5      0.01
dtmin      dtmax      irelu  nremax      tolreu

```

```

-1.00e-00 -1.00e-00 0 10 1.00e-01
SWEEP #2:
nz iseq npm partStyle iswpdir iplstt iplend
9 1 3 1 2 1 96
impl itmstep keslv ichemslv nplane inner mxin tolin
4 1 1 1 1 1 5 0.01
dtmin dtmax irelu nremax tolreu
-1.00e-00 -1.00e-00 0 10 1.00e-01
SWEEP #3:
nz iseq npm partStyle iswpdir iplstt iplend
5 1 2 1 2 1 40
impl itmstep keslv ichemslv nplane inner mxin tolin
4 1 1 1 1 1 5 0.01
dtmin dtmax irelu nremax tolreu
-1.00e-00 -1.00e-00 0 10 1.00e-01
SWEEP #4:
nz iseq npm partStyle iswpdir iplstt iplend
6 1 2 1 2 1 40
impl itmstep keslv ichemslv nplane inner mxin tolin
4 1 1 1 1 1 5 0.01
dtmin dtmax irelu nremax tolreu
-1.00e-00 -1.00e-00 0 10 1.00e-01
SWEEP #5:
nz iseq npm partStyle iswpdir iplstt iplend
7 1 2 1 2 1 40
impl itmstep keslv ichemslv nplane inner mxin tolin
4 1 1 1 1 1 5 0.01
dtmin dtmax irelu nremax tolreu
-1.00e-00 -1.00e-00 0 10 1.00e-01
SWEEP #6:
nz iseq npm partStyle iswpdir iplstt iplend
8 1 2 1 2 1 40
impl itmstep keslv ichemslv nplane inner mxin tolin
4 1 1 1 1 1 5 0.01
dtmin dtmax irelu nremax tolreu
-1.00e-00 -1.00e-00 0 10 1.00e-01
SWEEP #7:
nz iseq npm partStyle iswpdir iplstt iplend
11 1 3 1 3 1 20
impl itmstep keslv ichemslv nplane inner mxin tolin
4 1 1 1 1 1 5 0.01
dtmin dtmax irelu nremax tolreu
-1.00e-00 -1.00e-00 0 10 1.00e-01
SWEEP #8:
nz iseq npm partStyle iswpdir iplstt iplend
12 1 3 1 3 1 20
impl itmstep keslv ichemslv nplane inner mxin tolin
4 1 1 1 1 1 5 0.01
dtmin dtmax irelu nremax tolreu
-1.00e-00 -1.00e-00 0 10 1.00e-01

```